Design of ultra-robust supramolecular assemblies and their application to water treatment

by

Ty Christoff-Tempesta

B.S. Materials Science and Engineering
University of Florida, 2017

SUBMITTED TO THE DEPARTMENT OF MATERIALS SCIENCE AND ENGINEERING IN PARTIAL FULFILLMENT OF THE REQUIREMENTS FOR THE DEGREE OF

DOCTOR OF PHILOSOPHY IN POLYMERS AND SOFT MATTER

at the

MASSACHUSETTS INSTITUTE OF TECHNOLOGY

May 2022

Signature of Author:

Department of Materials Science and Engineering
April 11, 2022

Certified by:

Julia H. Ortony
Associate Professor of Materials Science and Engineering
Thesis Supervisor

Accepted by:

Frances M. Ross
Professor of Materials Science and Engineering
Chair, Departmental Committee on Graduate Studies

Design of ultra-robust supramolecular assemblies and their application to water remediation

by

Ty Christoff-Tempesta

Submitted to the Department of Materials Science and Engineering on April 11, 2022 in partial fulfillment of the requirements for the Degree of Doctor of Philosophy in Polymers and Soft Matter.

Abstract

Molecular self-assembly offers a powerful bottom-up approach to producing small molecule nanostructures with high surface areas, tunable surface chemistries, and pristine internal order. Conventionally, the dynamic nature of these systems has constrained their use to specific cases in primarily biomedical applications. Here, I present the design of molecular self-assemblies constructed from small molecule aramid amphiphiles to overcome these limitations. Aramid amphiphiles incorporate a Kevlar-inspired domain that imparts strong, cohesive intermolecular interactions between molecules. This design results in the self-assembly of aramid amphiphiles into nanostructures with suppressed dynamic mobility and mechanical properties rivaling silk. By harnessing this stability, I expand the application space of small molecule assemblies to extending molecular assemblies to the solid-state, stabilizing unusual metastable nanostructures, and producing stable antifouling surface coatings. Finally, I leverage surface areas near 200 m^2/g to design aramid amphiphile-based nanomaterials that treat liters of lead-contaminated water with single milligrams of material. Incorporating durable interactions into supramolecular assemblies offers a route to surmount the limitations of conventional assemblies, enabling customizable nanomaterials for demanding applications.

Thesis Supervisor: Julia H. Ortony
Title: Associate Professor of Materials Science and Engineering

Never be so kind, you forget to be clever.
Never be so clever, you forget to be kind.

- marjorie, Taylor Swift

Acknowledgements

To my doctoral advisor, Prof. Julia Ortony, I am endlessly appreciative for your mentorship, guidance, and unwavering support throughout my graduate career. Thank you for welcoming me into the world of small molecule science, broadening my scientific imagination, and supporting my growth as a scholar and world citizen. I will also finally concede that some graphs look better when made in Origin instead of Excel. My thesis committee has also been an integral part of this journey: Prof. Michael Cima and Prof. Timothy Swager, thank you for your thoughtful inquiries and ideas throughout my Ph.D. I grew deeply as a scientist as a result of your contributions and involvement. To my labmates – Robin, Yukio, Dae-Yoon, Cynthia, Andrew, Yu-Jin, and Sam – thank you for not only being excellent collaborators but for creating an excellent lab culture. I consider myself enormously lucky to have worked with and alongside you. In particular, thank you Yukio for carrying us through delirious days at Argonne and bringing endless cheer to our group. To my undergrad mentee Linnaea, your contributions to science are already outstanding, and I am beyond excited to see where your future carries you.

It is perhaps unusual to thank a singer, songwriter, producer, director, and (so far) 11-time Grammy-winner in a dissertation, but I think anyone who has spent even five minutes around me during my PhD knows that Taylor Swift's music and activism were a cornerstone of my graduate experience. In the unlikely scenario that you ever come across this thesis, thank you Taylor for > 70,000 minutes of happy, free, confused, and lonely at the same time (source: Spotify Wrapped), and for standing up for the rights of marginalized communities.

Brittani, Tiara, Neil, Unaiza, Aaron, and Hannah – my close friends from before graduate school – thank you for reminding me that there is a real world outside of MIT, for all of the game nights and meetups, for grounding me, and for being an endless source of joy, laughter, and support.

Early in my PhD, I competed with an incredible group of people who represent the best of the Institute in a case competition; I have since come to appreciate this competition as a formative experience to my outlook on the interplay between science and society.

Cherry, Ellena, Jordan, Cristina, and Audrey, thank you for showing me how science may be used to benefit the broader world, for upping my emoji game, for not shaming my inability to get on a surfboard, and for the most memorable experiences.

To the LAATTE crew – Eric, Tiffany, Andrew, and Lindsey – thank you for welcoming me into your family over the last year and half, for warm waffles in frigid conditions, for taco Fridays, and for exceptionally warm friendship.

Pierre and Safia, thank you for keeping me sane during the pandemic, for an endless supply of lava cakes and crepes, and for encouraging terrible pandemic decisions like trying P90X to stay active. I'll be sure to keep you apprised of my future addresses so you know where to ship extra desserts.

Elad, Eesha, Kat, Shayna, and the rest of the PPSM crew, thank you for getting me out of the lab for unforgettable social gatherings, whether spiderwebs caught in ceilings, backyard barbecues, afternoon teas with ridiculous hats, or days on the mountain. Your friendships have been a boundless source of encouragement and happiness.

To the Hydrogen Research Crew – Lily, Sara, and Margaret – I cannot believe how lucky I was to sit next to you in first-year Thermodynamics. From slogging through classes to countless board game nights, competitions, and being on MIT's monitors, thank you for five years of commiserating and laughter. Your close friendship has meant the world to me.

To the Spoopy Crew – Evi, Kate, Jackie, and Cécile – I don't know if I have the words for how much your friendship has meant to me. You taught me the importance of self-care and venting, supported my addition to Flour hot cocoas, and brought countless nights of laughter that formed the foundation of my graduate school experience. You have made pursuing a PhD the most imaginably rewarding experience that it could have been.

To my family, I am unendingly grateful. Throughout my entire life, you all have been a constant bedrock of support and encouragement, and I am deeply thankful that whether I was celebrating new successes or dealing with the most difficult parts of graduate school, I have always been able to pick up the phone and know that you were there to have my back.

Alex: if I could do graduate school over again, I would change very little because being here brought me to you. I am unendingly thankful to have you by my side, for your endless support, encouragement, and love. Jeg elsker deg.

I would not be here without the teachers who believed in me as a scientist and scholar well before I knew this could even be a path for me. In particular, I would like to thank Mrs. Lynne Burrier and Prof. Kevin W. Davies, two teachers and mentors who welcomed me entirely into their spaces as a high schooler. My interest in STEM traces directly back to your classrooms and labs, and I am eternally grateful for that. This thesis is dedicated to you.

Professional Acknowledgements

I gratefully acknowledge the fellowship support of the National Science Foundation Graduate Research Fellowship Program under grant no. 1122374, the Martin Family Society of Fellows for Sustainability, and the Hugh Hampton Young Fellowship.

This material is based upon work supported by the National Science Foundation under grant no. CHE-1945500. This work was supported in part by the Professor Amar G. Bose Research Grant Program, the Abdul Latif Jameel Water and Food Systems Lab, the Lemelson-Vest Foundation, and the MIT Center for Environmental Health Sciences under NIH Center grant P30-ES002109.

This work made use of the MRSEC Shared Experimental Facilities at MIT supported by the National Science Foundation under award number DMR-14-19807 and the MIT Department of Chemistry Instrumentation Facility. X-ray scattering measurements were performed at beamline 12-ID-B of the Advanced Photon Source, a US Department of Energy Office of Science User Facility operated for the US Department of Energy Office of Science by Argonne National Laboratory under contract no. DE-AC02-06CH11357. This work was performed in part at the Harvard University Center for Nanoscale Systems cryo-TEM facility, a member of the National Nanotechnology Coordinated Infrastructure Network, which is supported by the National Science Foundation under award no. 1541959. Specimens were prepared and imaged at the Automated Cryogenic Electron Microscopy Facility in MIT.nano on a Talos Arctica microscope, which was a gift from the Arnold and Mabel Beckman Foundation.

Contents

Chapter 1

Introduction

Supramolecular assemblies, defined in this dissertation as nanostructures formed by the spontaneous organization of organic small molecule amphiphiles in water, play a critical role in enabling life.[1, 2] The cell membrane is perhaps the most quintessential example of a supramolecular assembly (Figure 1.1), and offers insight into the structure-property relationships which underlie their ubiquitous presence in nature. For example, controlled surface chemistries of cell membranes enable desirable, specific interactions with their environments.[3] Nanometer-scale bilayer thicknesses give rise to extraordinarily high surface area-to-volume ratios which enable more chemistry on less material.[4] The use of noncovalent interactions to form nanostructures enables spontaneous self-healing to repair defects.[5] Finally, a combination of specific intermolecular interaction strengths and multicomponent co-assembly enable control over membrane dynamics.[6, 7]

Inspired by these characteristics, researchers over the past several decades have created a wealth of synthetic analogues to harness these properties. Peptide-based, calixarene, pillarene, cucurbituril, and prodrug assemblies are among the multitudes of spatially arranged nanostructures with molecular length scales produced through bottom-up self-assembly.[8-16] To highlight one example, peptide amphiphiles covalently bind hydrophilic peptide headgroups to hydrophobic (typically aliphatic) tail groups. These molecular structures have been tuned to, e.g., induce β-sheet formation, regulate solubility, and express bioactive sequences.[16] Supramolecular assemblies of peptide amphiphiles commonly form cylindrical nanofibers, and the high-aspect-ratios of these materials combined with their capacity for expressing high densities of bioactive moieties hold promise for biomedical applications including drug delivery, tissue engineering, and regenerative medicine.[17-19]

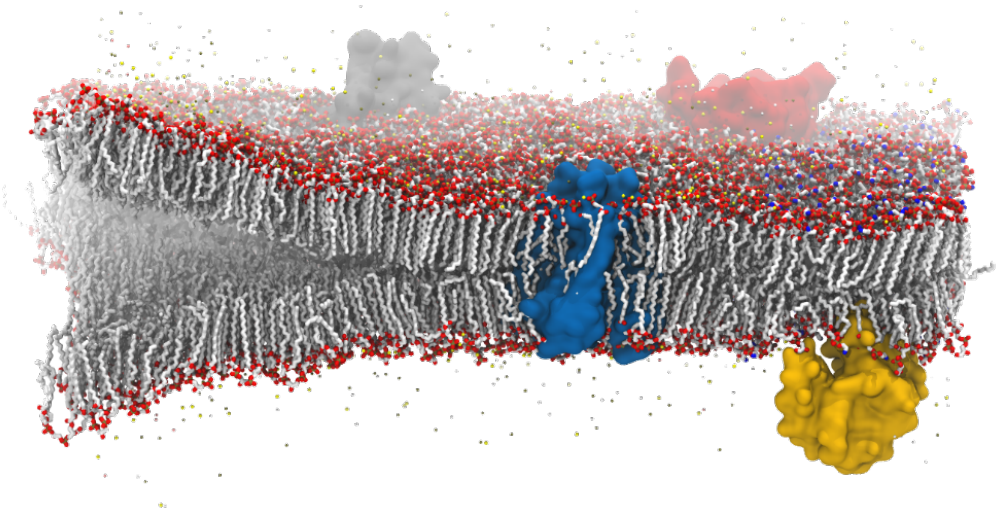

Figure 1.1. The cell membrane is a quintessential example of a naturally-occurring supramolecular assembly. This membrane is constructed of small molecule amphiphiles called phospholipids (illustrated as red spheres with white, squiggly tails) which spontaneously form the characteristic high surface area lipid bilayer in aqueous environments. Cell membrane surfaces are optimized for specific environmental interactions and internal dynamics are controlled through co-assembly with proteins and small molecules. Image credit: Thomas Lemmin, Laboratory for Molecular Modeling, École Polytechnique Fédérale de Lausanne.

In spite of the desirable characteristics of supramolecular assemblies for engineering applications, the dynamic nature of these systems has historically limited their use to solvated environments where dynamic motion is permissible or desired. Notably, supramolecular assemblies suffer from a breadth of dynamic instabilities, ranging from the exchange of molecules between assemblies to the rapid translation and rotation of molecules within assemblies.[20-22] However, there are a broad range of applications where the inherent properties of supramolecular assemblies may be desirable, including liquid-phase applications where stability is critical, applications where a weakly hydrophilic or hydrophobic surface is desirable, and solid-state applications.

In this dissertation, I explore the design of small molecules dubbed “aramid amphiphiles” which form nanostructures with strongly interacting internal domains. Aramid amphiphiles incorporate a triaramid repeat unit inspired by the molecular structure of *Kevlar* to form robust, microns-long nanoribbons with suppressed molecular exchange and mechanical properties rivaling silk. In Chapter 2, I explore the design principles which create aramid amphiphile assemblies, the properties of these assemblies, and the ability

to translate aramid amphiphile nanostructures to solid-state materials. In Chapter 3, I harness stability imparted by the aramid amphiphile design to sustain the unusual nanotube metastable state of a photoswitchable supramolecular assembly. In Chapter 4, I take advantage of the nanostructures' high-aspect-ratios and tunable surface chemistries to form surface coatings which are resistant to biofouling. In Chapter 5, I extend the use of supramolecular assemblies to treating water contaminated with heavy metals by decorating the nanomaterial surfaces with pharmaceutical compounds for heavy metal treatment. Finally, in Chapter 6, I measure and optimize amphiphile head group dynamics and hydration to enhance the performance of heavy metal remediating nanostructures. This body of work aims to reveal molecular design principles that produce unconventionally robust supramolecular nanostructures and accordingly apply these assemblies to urgent challenges.

Supramolecular assemblies: a brief primer

The self-assembly of organic small molecules into supramolecular nanostructures is driven by orthogonal interactions between differing parts of the molecule (typically hydrophilic and hydrophobic regions, dubbed head and tail groups, respectively) and their surrounding aqueous environment. The field has developed significantly over the past half century, spanning the development of fundamental theories which underlie self-assembly behavior[23] to the design of a breadth of functional nanomaterials.[24-26] Pushing beyond the prototypical molecular designs found in nature – primarily singly- or doubly-charged head groups with single or branched aliphatic tails – a library of novel synthetic analogous have incorporated cohesive or stimuli-responsive chemical moieties to impart additional functionality. For example, incorporating chemical groups responsible for hydrogen bonding,[27] π stacking,[28] photo-responsiveness,[29] and pH-responsiveness[30] into amphiphile design have been topics of significant investigation. Recently, more complex phenomena found in nature such *in situ* surface functionalization[31, 32] and co-assembly of multiple components[33, 34] have also been integrated into supramolecular nanostructures, The application space of supramolecular assemblies currently spans primarily biomedical applications (e.g. tissue engineering[35] and drug delivery[36]), optoelectronic applications

(e.g. photovoltaics[37] and biosensing[38]), and energy applications (e.g. photocatalysis[39] and supercapacitance[40]).

Overcoming dynamic instabilities: the aramid amphiphile design

The noncovalent interactions underpinning supramolecular assemblies enable dynamic motion critical to biological processes,[41] which can again be understood through an analysis of the cell membrane. The fluid mosaic model describing cell membrane dynamics highlights that constituent lipids and proteins comprising the bilayer are in constant rotational and translational motion.[42-45] Fluidity is so critical in these assemblies that if protein rotation is prevented by any means, proteins lose their functionality.[43, 44] Cell membranes also contain components like cholesterol to regulate bilayer fluidity by stabilizing the membrane at elevated temperatures and preventing phospholipid clustering at depressed temperatures. In turn, operation and cohesion of cell membranes is maintained over a range of environmental conditions.[6, 7, 46]

The dynamic nature intrinsic to conventional supramolecular assemblies results in a host of measurable dynamic processes which impact the performance of synthetic analogues, including high molecular exchange rates between assemblies, molecular migration of amphiphiles within an assembly, and dynamic instabilities.[21, 41, 47-50] Though these dynamic processes may be beneficial for the application of supramolecular materials in biological environments, increasing nanostructure stability might provide a path for their use in non-biological applications. Specifically, imparting high stability to supramolecular amphiphile assemblies can inhibit or control assembly dynamics, which may minimize the loss of amphiphiles from assemblies in aqueous environments, facilitate modifications to nanostructures post-assembly, and enable application beyond solvated environments.

In this dissertation, I report on the development of the “aramid amphiphile,” a small molecule designed to suppress dynamic effects in supramolecular assemblies.[51] Aramid amphiphiles have at least three distinct domains: in addition to the (1) nonpolar tails and (2) polar head groups found in the design of conventional amphiphiles, aramid amphiphiles also contain (3) a triaramid “structural domain” inspired by the molecular

structure of Kevlar. This structural domain is designed to create a network of hydrogen bonding interactions within amphiphilic assemblies to positionally "lock" each molecule to its neighbors. Incorporating a high density of strong intermolecular interactions within assemblies represents a notable divergence from conventional amphiphile design principles.[52, 53]

Molecular packing in strongly interacting systems

In 1976, Israelachvili et. al. comprehensively described the thermodynamics of packing for small molecule surfactants, ultimately giving rise to the concept of the *packing parameter* as a predictive tool for determining the self-organized nanostructure of amphiphiles.[23, 54] The packing parameter, p, is a dimensionless metric which incorporates three quantities to speculate organization: a, the thermodynamically derived surface area per molecule of an assembly's hydrophobic core, which is strongly influenced by surfactant head group interactions and characteristics; l, the length of the surfactant's tail group; and V, the volume of the surfactant's tail group. These quantities are related in Equation **1.1**.

$$p = V / (l \cdot a) \qquad (\mathbf{1.1})$$

Based on this relationship, the packing parameter is able to suggest the spontaneous assembly of small molecules into micelles ($p \approx 1/3$), cylinders ($p \approx 1/2$) , continuous cubic phases ($1/2 < p < 1$), and lamellar phases ($p \approx 1$), and the inverts of these geometries.[23] Since its description, the packing parameter has successfully explained the assembly of a diverse range of amphiphilic materials spanning lipoplexes for gene delivery to bacterial membranes to block copolymer systems.[55-57]

Significant attention has been given to the role of an amphiphile's head group in predicting the geometry of an assembled system. Notably, the packing parameter has adapted over time to describe a as an 'effective head group area,' noting that the interaction strength of a surfactant's head group can be modulated by factors including pH, salt identity and concentration, and temperature.[58-61] However, the thermodynamics underlying packing parameter still rely on 'simple' tail groups to describe self-organization. The packing parameter is primarily descriptive when tail groups are single or branched

aliphatic tails that induce weak van der Waals interactions between the tails of neighboring molecules.

In this dissertation, I investigate the assembly of surfactants with deliberately robust intermolecular interactions in the tail group region through the addition of the aforementioned structural domain. In addition to suppressing dynamic instabilities, the inclusion of a structural domain allows us to probe the organization of molecules which are not well-predicted by the packing parameter. In fact, in most cases, we find that aramid amphiphiles form microns-long and nanometers-wide lamellar ribbons, demonstrating a strong preference for in-register hydrogen bonding along the ribbon axis and a nanoribbon width controlled by head group charge and sterics. This geometry is largely unpredicted by packing parameter considerations, which would tend towards a circular or planar bilayer cross-section.

The assembly of aramid amphiphiles is also strongly dictated by a fine balance between the hydrophobic effect and crystallization and solubility effects. The design parameters for molecules reported in this dissertation were obtained after synthesis and attempted assembly of dozens of molecules with varying head and tail group lengths, sterics, and interaction strengths, and head group charges. Notably, we find aramid amphiphiles must have three aramid repeat units and a *tert*-butyl or similar short, branched, aliphatic tail for assembly to occur. With more aramid repeat units in the structural domain or a straight aliphatic tail of any length (C2-C16 lengths were tested), the molecules preferentially crystallized in water over forming self-assembled structures. Conversely, with fewer than three aramid repeat units, a preference for molecule solubilization or agglomeration into disordered aggregates was observed. Whereas the packing parameter alone may indicate these changes would result in the formation of different assembly morphologies (by effectively changing tail group length and/or volume), these results suggest that different thermodynamic conditions underlie the assembly of small molecule amphiphiles with strongly interacting tail group regions than conventional surfactant systems.

A broad need for effective, point-of-use water treatment technologies

A promising application space for the robust supramolecular assemblies reported in this dissertation is the removal of heavy metal contaminants from drinking water sources, which I motivate here. In 2014, the city of Flint, Michigan changed the primary source of the city's potable water from a Detroit-based supply to the Flint River as a cost-saving measure.[62] However, the acidity of the new water supply differed from that of the old source, leading to widespread corrosion of the city's lead piping. Significant quantities of lead consequently leached into Flint's drinking water supply.[62, 63] For context, the World Health Organization sets an actionable level of lead in water at 10 parts per billion (ppb).[64] The "Ground Zero" household taps analyzed in Flint tested as high as 13,200 ppb lead.[65]

While the case of Flint, Michigan is widely known today, it is not unique. A 2016 study compiling data from health departments across 21 states representing 61% of the United States population found nearly 3,000 locations with lead poisoning levels at least double that of Flint at the height of its crisis.[66] Furthermore, the most recently available data (ca. 2019) from the Institute for Health Metrics and Evaluation at the University of Washington concludes that one in three children worldwide – over 800 million children – have blood lead levels higher than an actionable level.[67] While drinking water alone is not the sole source of lead transport to humans, these realities underscore an urgent need to develop technologies which are highly effective at removing heavy metal contaminants like lead from drinking water supplies.

The tunable surface chemistries and high surface areas hallmark of supramolecular assemblies make them a promising candidate for this application. However, this space has been largely unexplored due to the dynamic instabilities historically intrinsic to this class of materials. In this dissertation, I explore applying aramid amphiphiles to create nanostructures which are coated with chemical moieties capable of capturing heavy metal contaminants. Head group designs for these amphiphiles use chelators, a class of compounds renowned for their capability to complex heavy metals, which are also sufficiently hydrophilic to induce self-assembly. By probing and optimizing head group dynamics and hydration, we can obtain nanostructures capable of treating thousands of liters of lead-contaminated water with single grams of material.

Chapter 2

Self-assembly of aramid amphiphiles into ultra-stable nanoribbons and aligned nanoribbon threads

This chapter was adapted from the publication "Self-assembly of aramid amphiphiles into ultra-stable nanoribbons and aligned nanoribbon threads," originally published in Nature Nanotechnology.[51]

Abstract: Small-molecule self-assembly is an established route for producing high-surface-area nanostructures with readily customizable chemistries and precise molecular organization. However, these structures are fragile, exhibiting molecular exchange, migration and rearrangement—among other dynamic instabilities—and are prone to dissociation upon drying. Here we show a small-molecule platform, the aramid amphiphile, that overcomes these dynamic instabilities by incorporating a Kevlar-inspired domain into the molecular structure. Strong, anisotropic interactions between aramid amphiphiles suppress molecular exchange and elicit spontaneous self-assembly in water to form nanoribbons with lengths of up to 20 micrometers. Individual nanoribbons have a Young's modulus of 1.7 GPa and tensile strength of 1.9 GPa. We exploit this stability to extend small-molecule self-assembly to hierarchically ordered macroscopic materials outside of solvated environments. Through an aqueous shear alignment process, we organize aramid amphiphile nanoribbons into arbitrarily long, flexible threads that support 200 times their weight when dried. Tensile tests of the dry threads provide a benchmark for Young's moduli (between approx. 400 and 600 MPa) and extensibilities (between approx. 0.6 and 1.1%) that depend on the counterion chemistry. This bottom-up approach to macroscopic materials could benefit solid-state applications historically inaccessible by self-assembled nanomaterials.

Introduction

Spontaneous self-assembly of small amphiphilic molecules in water provides a powerful route to nanoscale structures with molecular-scale dimensions and pristine internal organization.[25, 68] High-aspect-ratio nanostructures afforded by molecular self-assembly may be entangled or aligned, while maintaining high surface areas and tunable surface chemistries.[69, 70] However, these supramolecular structures are generally fragile due to their weak intermolecular interactions[48, 71] and pervasive dynamic instabilities – i.e. molecular exchange, migration, insertions, rearrangements, and transpositions.[20-22] Further, internal transient water contributes to the vulnerability of amphiphilic nanostructures by facilitating enzymatic or hydrolytic degradation.[72, 73] Because of these limitations, small molecule assemblies are generally developed for biomaterials applications, where fast dynamics and biodegradability are harnessed as key design features.[74-76] These properties preclude their use in air, where they lack the structural stability imposed via the hydrophobic effect that is required to hold them together. Therefore, an amphiphile self-assembly platform that minimizes dynamics is an important target and could provide an approach to solid-state applications for which precise molecular organization, nanoscale structure, tunable surface chemistries, and water-processability are desirable.[77] Such solid-state applications could range from ion transporting to thermally conductive soft materials.[78, 79]

A reliable strategy for enhancing mechanical properties of molecular materials is to incorporate hydrogen bonding domains into the molecular design.[80] For example, the collective hydrogen bonding between aromatic amides (aramids) in Kevlar (poly(*p*-phenylene terephthalamide), PPTA) lead to its renowned strength and impact resistance.[81] Similar aramid chemical motifs have been incorporated into the design of biomimetic peptide-based amphiphiles;[82, 83] however, in these cases, the impact of the aramid domains on mechanical properties remains unknown. In contrast to small amphiphilic molecules, polymeric aramid nanofibers composed of PPTA have shown strong mechanical behavior,[84] even upon drying, but neither control over nanofiber surface chemistry nor precise internal molecular organization is achievable. In a handful

of cases, molecules containing aramid moieties have aggregated in a variety of solvents into short rod-like or hockey-puck micelles, with the longest dimension on the order of tens or hundreds of nanometers.[85-87] Despite these contributions, rational design of amphiphiles to form mechanically robust high-aspect-ratio nanostructures and the processing of these nanostructures into aligned solid-state 1-dimensional materials remains an important goal.

Here, we show a molecular design motif that incorporates aramids as a structural domain within small molecule amphiphiles. This design produces aramid amphiphiles (AAs), molecules that self-assemble in water to form nanoribbons. AA nanoribbons are designed to be intrinsically hydrolysis-resistant, containing amides that are buried in the hydrophobic interior of the nanostructure, away from water.[72] AAs incorporate three attributes to suppress exchange dynamics and to enhance mechanical properties: (1) a high hydrogen bond density, with six hydrogen bonds per molecule; (2) in-register organization within each hydrogen bond network and the ability to form interplane π-π stacking;[88] and (3) minimal steric packing strain and torsion to minimize hydrogen bond distances,[89] achieved by incorporating unobtrusive amphiphile head and tail groups into the molecular design. As a result, these nanoribbons are candidates for alignment and removal from water while maintaining their structure to obtain macroscopic, air-stable threads.

Results and Discussion

We synthesized AAs with three different head group chemistries to tune the surface charge of the nanoribbons (Figure 2.1a): compound **1**, an anionic pentetic acid amphiphile, compound **2**, a zwitterionic ammonium sulfonate amphiphile, and compound **3**, a cationic triazaheptane amphiphile. The structural domains of compounds **1** – **3** contain three aramid repeat units, and the hydrophobic tails consist of branched, six-carbon neopentyl groups. These features are designed to elicit spontaneous self-assembly in water into nanostructures with strong intermolecular interactions (Figure 2.1b).

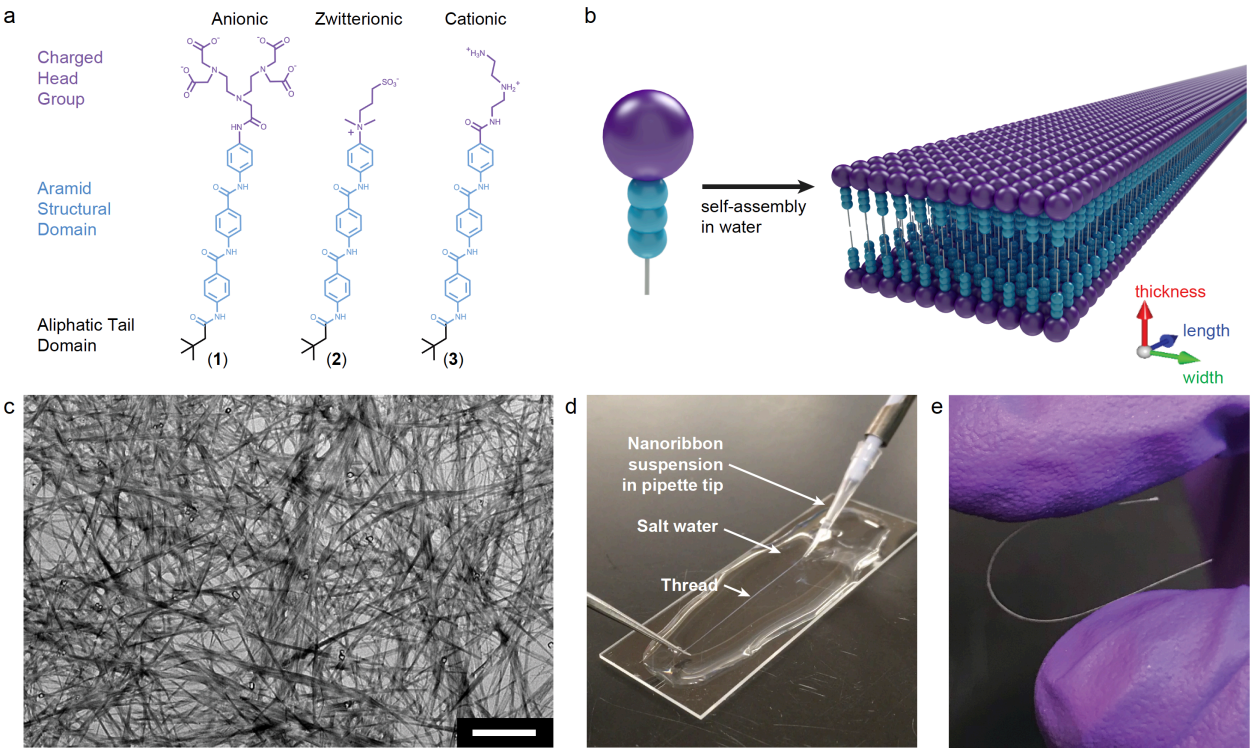

Figure 2.1 l Kevlar-inspired aramid amphiphiles self-assemble into ultra-stable nanoribbons capable of hierarchical ordering to form dry macroscopic threads. **a**, Aramid amphiphiles are composed of a charged head group and an aliphatic tail to induce amphiphilic self-assembly, and an aramid structural domain to yield collective intermolecular hydrogen bonding. Aramid amphiphiles **1**, **2**, and **3** have anionic, zwitterionic, and cationic head groups, respectively. **b**, Aramid amphiphiles are designed to spontaneously self-assemble in water into nanoribbons with suppressed exchange dynamics. **c**, Dried nanoribbons of **2** are observed in a representative transmission electron micrograph (TEM) (scale bar, 1 μm). **d**, A nanoribbon suspension (compound **3**) is pulled out of a pipet tip by tweezers into a sodium sulfate solution to form a 1-dimensional gel. **e,** The gel is removed from water and dried to form a thread composed of aligned nanoribbons that can be bent and handled easily.

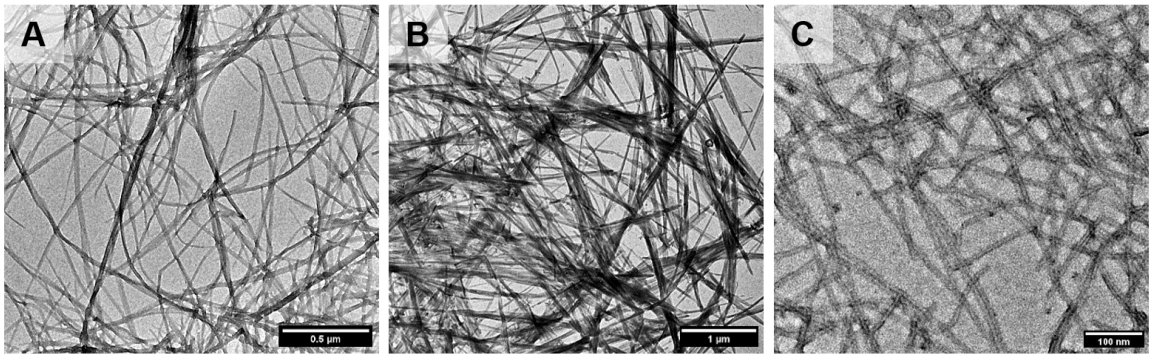

Figure 2.2 l Compounds **a**, **1**; **b**, **2**; and **c**, **3** in water self-assemble into microns-long nanoribbons, as visible in transmission electron microscopy images of their microstructures.

We observe the assembly of **1**, **2**, and **3** in water into high-aspect-ratio nanoribbons by conventional transmission electron microscopy (TEM) (Figure 2.1c, Figure 2.2). The nanostructures' stability and high-aspect-ratios allow for shear alignment during gelation. This process leads to arbitrarily long threads (Figure 2.1d) that remain intact when removed from water (Figure 2.1e).

Small angle X-ray scattering (SAXS) profiles of compounds **1-3** in water fit most closely to a lamellar bilayer model (Figure 2.3a).[90, 91] This fit gives a nanoribbon thickness of 3.9 nm for **1**, **2**, and **3**, which is corroborated by atomic force microscopy (AFM) height profiles (Figure 2.4). The observed slope of -2 in the low-*q* regime of the SAXS profiles further suggests one-dimensional nanostructures in solution.[92] Cryogenic TEM (cryo-TEM) was used to image the nanoribbons in water at higher resolution for determining nanoribbon widths. Based on cryo-TEM, the widths of nanoribbons of **1**, **2**, and **3** are 5.5 nm, 5.1 nm, and 5.8 nm, respectively (Figure 2.3b, Figure 2.5). We find that the nanoribbon geometry is insensitive to temperature and concentration, where nanoribbons of **3** are observed up to 80 °C and from 0.1 to 20 mg/mL, but sensitive to pH (Figure 2.6, Figure 2.7). Interestingly, we observe that self-assembled AA nanoribbons elongate upon bath sonication (with powers of approximately 10 mW/mL), reaching extraordinary lengths of up to 20 μm,[93, 94] corresponding to width-to-length aspect-ratios of 4,000:1. Sonication has been previously shown to facilitate reorganization of hydrogen bonding in self-assembling systems[95]. The observed high-aspect-ratios of AA nanoribbons confirm that highly anisotropic intermolecular interactions occur between the nanoribbon long and wide axes (Figures 2.4 and 2.5).

The nanoribbon geometry allows us to draw conclusions about the molecular packing. We observe through AFM height profiles a nanoribbon thickness approximately equal to two molecular lengths. Knowing that the hydrophilic head group must be exposed to water and the hydrophobic region (including the structural domain) must be shielded, we deduce that interdigitation between the molecules in the assembly must be limited to their short aliphatic tails. Concomitantly, we conclude that the molecules most likely adopt lamellar packing, which is corroborated by fits of SAXS profiles to a lamellar model (Figure 2.3a). This molecular arrangement deviates from the 2-dimensional networks observed

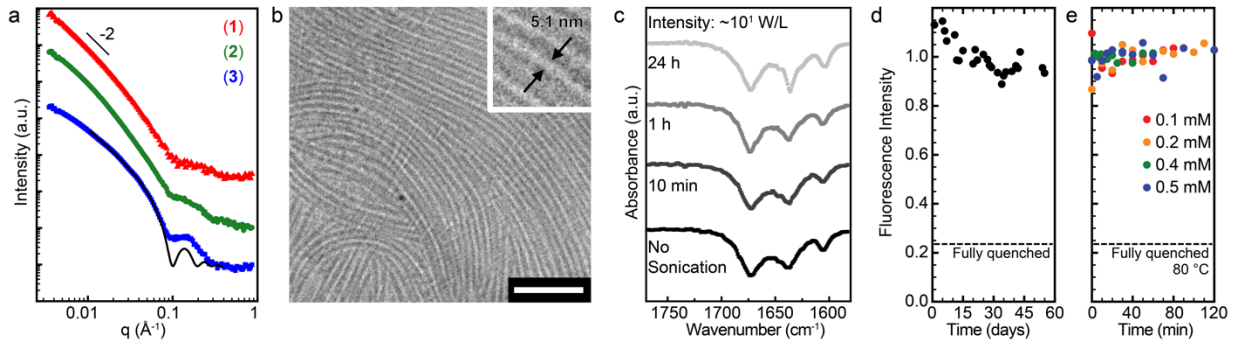

Figure 2.3 l Aramid amphiphile nanoribbons exhibit minimal molecular exchange. **a**, Small angle X-ray scattering of **1**, **2**, and **3** nanoribbons in water shows a slope of -2 in the low-*q* regime, indicating high-aspect-ratio structures, and is best fit to a lamellar model (black line) giving a 3.9 nm nanoribbon thickness, consistent with nanoribbon geometries. **b**, Representative cryogenic TEM of nanoribbons of **2** in water reveals nanoribbon widths of approx. 5 nm (scale bar, 100 nm). **c**, ATR-FTIR of compound **3** nanoribbons shows the emergence of a sharp peak at 1638 cm^{-1} upon bath sonication, consistent with strengthening of the hydrogen bond network. **d**, Normalized fluorescence intensities of a 1:1 mixture of donor- and quencher-labeled nanoribbon suspensions are measured over 55 days. A nearly constant fluorescence intensity indicates minimal dark quenching and corresponds to minimal molecular exchange between nanoribbons over this time period. As a control, complete co-assembly of donor and quencher amphiphiles result in a 76% decrease in fluorescence intensity, illustrated by the horizontal dotted line. **e**, Normalized fluorescence intensities of mixtures of donor- and quencher-labeled nanoribbon suspensions at 80 °C show that FRET dark quenching is not observed upon heating. This experiment was carried out with AA concentrations ranging from 0.1 to 0.5 mM, and no changes in exchange were observed.

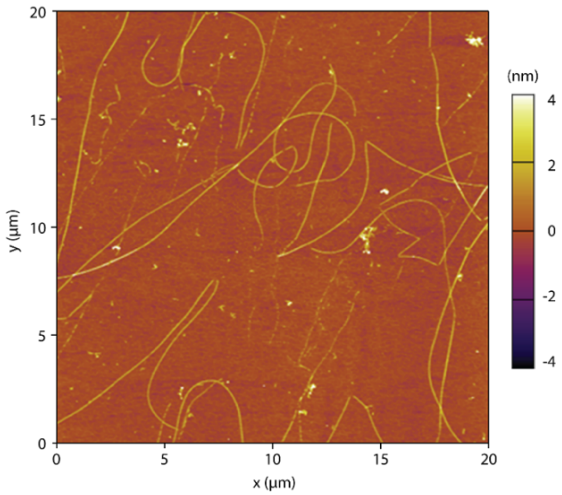

Figure 2.4 l A representative AFM profile of compound **3** nanoribbons deposited on mica illustrates nanoribbon lengths up to 20 µm as determined by ImageJ analysis. AFM nanoribbon cross-section analysis reveals heights of 3.7 ± 0.5 nm (average over height measurements of 61 nanoribbons).

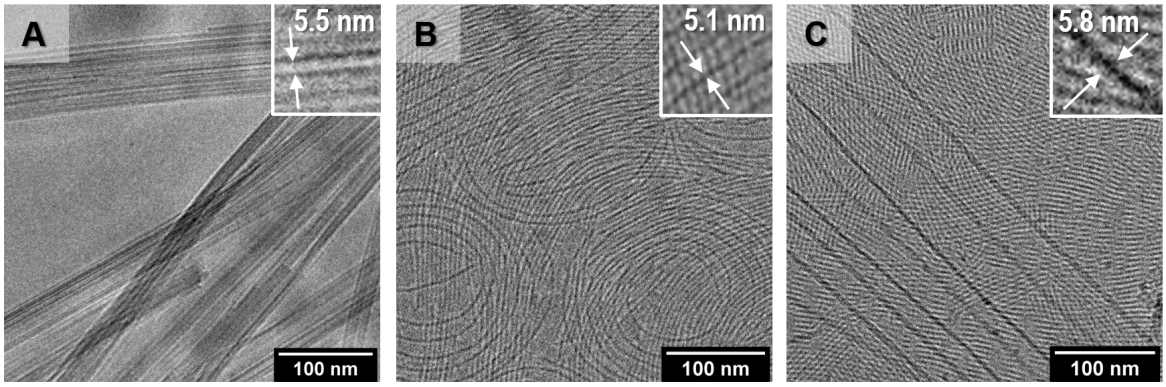

Figure 2.5l Cryogenic transmission electron microscopy images of assemblies of compounds **a**, **1**; **b**, **2**; and **c**, **3**.

in solid-state crystals of oligomeric *p*-benzamide crystals[96, 97] since the driving force for amphiphilic self-assembly imposes orientational constraints that differ from those implicated in crystallization.[98]

We performed attenuated total reflectance Fourier-transform infrared spectroscopy (ATR-FTIR) on solutions of compound **3** as a function of bath sonication time to observe the evolution of hydrogen bonding with nanoribbon formation in solution. Compound **3** nanoribbons are selected for this analysis because their solubility is high, and consequently produce the strongest signal of compounds **1**-**3**. However, molecular packing is likely dominated by the aramid structural domain, which is equivalent in all three AA compounds. Therefore, we expect the molecular packing of compound **3** to be representative of all AA nanoribbons, **1-3**, particularly because they all exhibit similar nanoribbon geometries. Shown in Figure 2.3c, a peak at 1638 cm^{-1}, corresponding to a carbonyl (C=O) amide I stretch and characteristic of β-sheet hydrogen bonding, becomes more pronounced as sonication time increases. The sharpening of this peak indicates that uniformity of intermolecular hydrogen bonding distances increases upon sonication, likely because sonication provides the necessary energy to overcome kinetic traps. As a control, addition of a denaturant, DMSO, to the nanoribbon suspension results in a suppression of the amide I peak, consistent with disruption of the hydrogen bonding network (Figure 2.8). The peaks at 1672 cm^{-1} and 1600 cm^{-1} are assigned to carbonyl stretching of the amide bond connecting the head group to the aramid structural domain

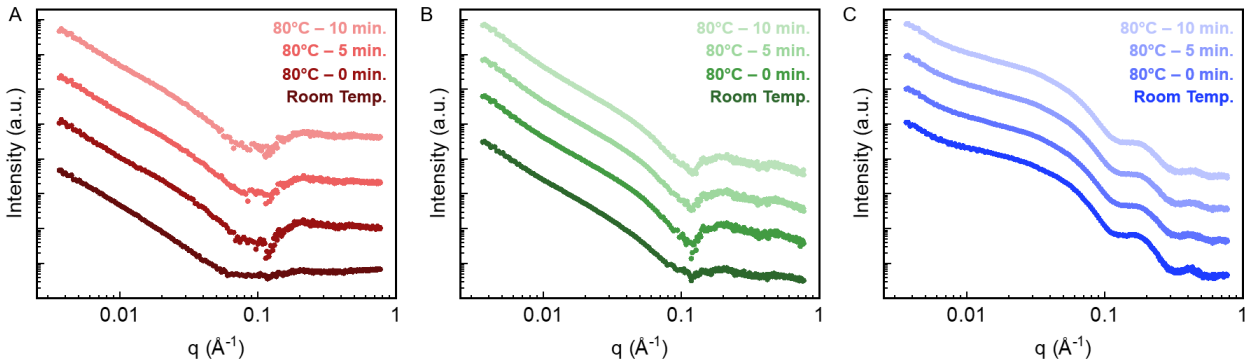

Figure 2.6 l Aqueous SAXS of **a**, compound **1**; **b**, compound **2**; and **c**, compound **3** shows no change in nanostructure morphology upon heating to and equilibrating at 80 °C. The significantly higher solubility of compound **3** results in SAXS profiles with enhanced signal-to-noise relative to compounds **1** and **2**.

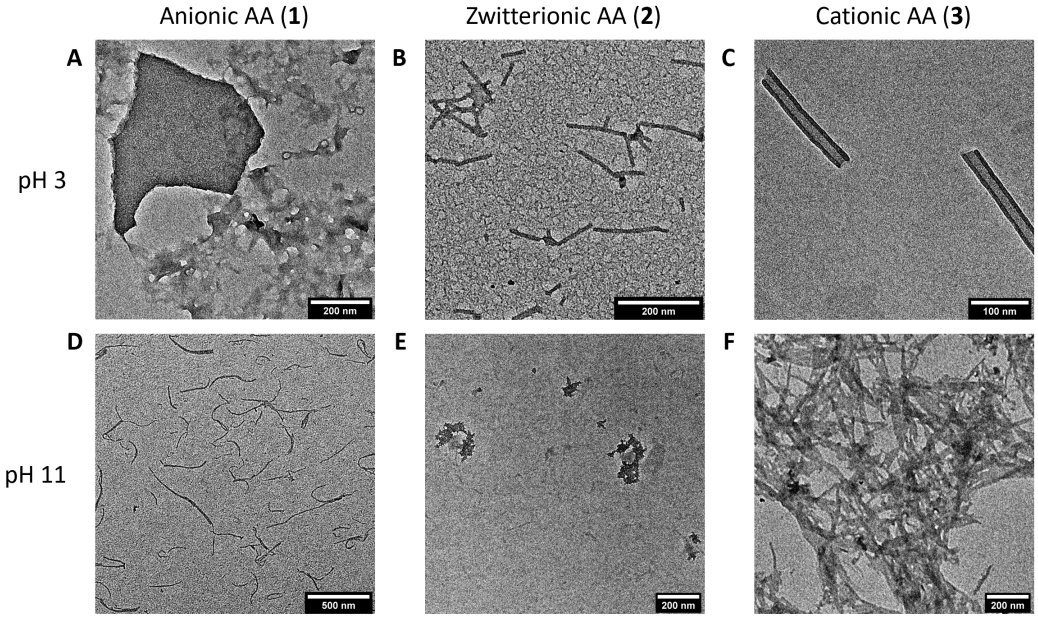

Figure 2.7 l The self-assembly morphology of aramid amphiphiles can be modulated by changing the pH, which affects effective head group size and charge. Representative micrographs of **a**, compound **1** at pH 3; **b**, compound **2** at pH 3; **c**, compound **3** at pH 3; **d**, compound **1** at pH 11; **e**, compound **2** at pH 11; and **f**, compound **3** at pH 11 are shown here. Compound **1** forms disordered aggregates at pH 3 and short noodle-like assemblies at pH 11; compound **2** forms needle-like assemblies at pH 3 and disordered aggregates at pH 11; and compound **3** forms cylindrical nanotubes at pH 3 and plate-like aggregates at pH 11. Aqueous suspensions of compounds **1**, **2**, and **3** at 0.1 mg/mL concentrations were adjusted to pH 3 and pH 11 using 0.5 M hydrochloric acid and sodium hydroxide, respectively, and bench sonicated for 10 minutes for these studies.

and carbon-carbon stretching in the aromatic units, respectively, and their positions and intensities are therefore less sensitive to molecular packing (Figure 2.9).[99, 100]

Collective hydrogen bonding within AA nanoribbons is expected to lead to strong internal cohesion and therefore slow molecular exchange dynamics.[48] We probed the rate at which individual AA molecules exchange between adjacent nanoribbons by Förster resonant energy transfer (FRET) dark quenching (see Methods for more details).[101] We mixed separate nanoribbon suspensions containing either fluorophore- or quencher-tagged amphiphiles and observed minimal molecular exchange between adjacent nanoribbons over 55 days (Figure 2.3d). Further, no changes in peak fluorescence intensity were observed when mixtures of fluorophore- and quencher-labeled nanoribbons were heated to 80 °C over a range of concentrations (Figure 2.3e). These results highlight the stability that aramid hydrogen bonding imparts on amphiphilic nanoribbon assemblies, representing a substantial departure from the typical exchange rates of 1-2 hours reported in phospholipid membranes and supramolecular peptide assemblies.[21, 22] The slow exchange dynamics of AA nanoribbons allow us to perform single-nanoribbon mechanical characterization experiments.

Direct mechanical characterization of solid-state nanofibers has previously been demonstrated to yield stress-strain profiles via AFM force measurements.[102, 103] However, this method requires that the widths of the fibers are large relative to the radius of curvature of the AFM tip. In the case of small nanostructures whose widths are less than 10 nm, as observed in AA nanoribbons, direct mechanical measurements pose significant experimental challenges. To circumvent the lower bound size limitation, indirect methods of nanofiber mechanical characterization have been developed.[104-106] These methods are based on AFM imaging of nanofilaments or nanofilament fragments followed by statistical analyses to determine Young's moduli or tensile strengths. Such studies have uncovered mechanical properties of a range of nanofilaments with diameters on the order of 10 nm including silver nanowires, carbon nanotubes, and amyloid fibrils.[104, 106, 107]

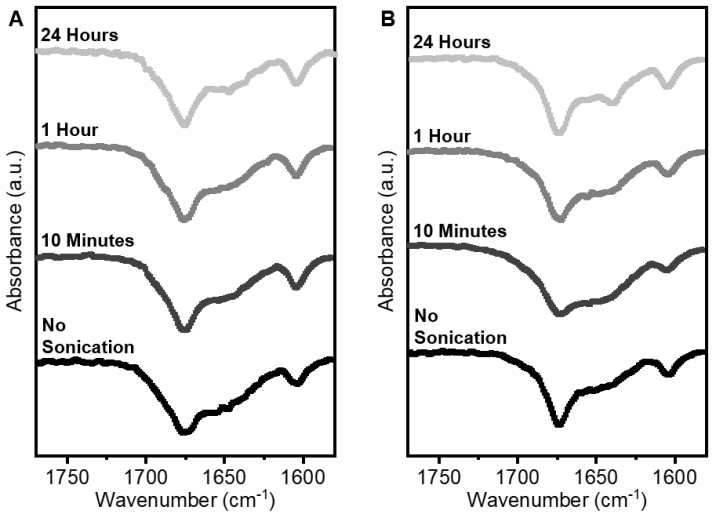

Figure 2.8 I ATR-IR spectra showing the effect of sonication time on intermolecular interactions between compound **3** in **a**, a 50:50 mixture of D_2O:DMSO-*d* and **b**, a 75:25 mixture of D_2O:DMSO-*d*. The amide I bond at 1638 cm^{-1} is enhanced with higher proportions of water and longer sonication times, resulting from the formation of a more uniform hydrogen bonding network in the self-assembled system.

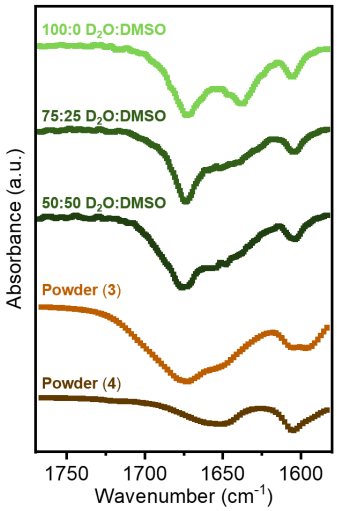

Figure 2.9 I FTIR spectra of compounds **3** and **4**, a control molecule with no head group, in dried powder form as controls and compound **3** dissolved in varying ratios of DMSO-*d* to D_2O. We assign the peak at 1672 cm^{-1} to the C = O stretch of the amide bond between the head group and structural domain and 1652 cm^{-1} to the C = O stretch of the amide bonding in aramid structural domain. The peak at 1672 cm^{-1} is present among all mixtures of DMSO-*d* and D_2O. Conversely, the amide I peak shifts to 1638 cm^{-1} in the full D_2O environment. This red shift indicates hydrogen bonding formation between at the corresponding amide bonding when compound **3** assembles in D_2O.[38] The peak at 1600 cm^{-1} is attributed to C – C stretching in the aromatic rings and is constant over all spectra.

We characterized the Young's modulus of AA nanoribbons using statistical topographical analysis of AFM images. The Young's modulus of compound **3** nanoribbons was measured due to its high solubility and for consistency among characterization techniques. Mechanical properties arise from the region with the strongest intermolecular interactions – the aramid structural domain – so we expect nanoribbons of **1** and **2** to exhibit similar Young's moduli and tensile strengths as compound **3**. The shape fluctuations of compound **3** nanoribbons (n = 29) in water equilibrated on a glass surface were used to determine their bending rigidity.[104, 105] Parametric splines to the contours of each nanoribbon were traced (Figure 2.10a) and fit to determine a persistence length, P = 3.9 ± 0.7 μm, from which the Young's modulus was calculated to be E = 1.7 ± 0.7 GPa (Figure 2.10b).

The ultimate tensile strength of AA nanoribbons was determined by AFM statistical analysis after horn sonication-induced scission, which produces nanostructure fragments in water below a threshold length, L_{lim}.[106, 108] For clarity, horn sonication delivers 100 to 1000 times greater sonication power intensity to the sample volume compared to bath sonication,[109],which was previously shown to reinforce the nanoribbon hydrogen bonding network by ATR-FTIR. From visualizing 400 horn sonicated fragments by TEM (Figure 3c), L_{lim} for the nanoribbons was evaluated from their fragment length distribution as 98 ± 26 nm, which corresponds to a tensile strength of $\sigma^* = 1.87 \pm 1.00$ GPa (Figure 2.10d). These mechanical properties place AA nanoribbons in a region of the Ashby plot viable for solid-state applications (Figure 2.10e).[110]

Materials constructed of small molecule amphiphile nanoribbons offer high surface areas, on the order of hundreds of m^2/g, dictated by the size of the constituent molecules. The tunable surface chemistries of such structures further allow for targeted interactions, and the capacity for co-assembly of different amphiphiles could allow such materials to perform multiple functions on the same surface.[111, 112] However, small molecule nanostructures are often limited to solvated environments due to their fast dynamics and reliance on the hydrophobic effect to hold their structures together. We explored the potential of aligning AA nanoribbons into solid-state thread-like materials, a possibility enabled by their suppressed exchange dynamics and robust mechanical properties.

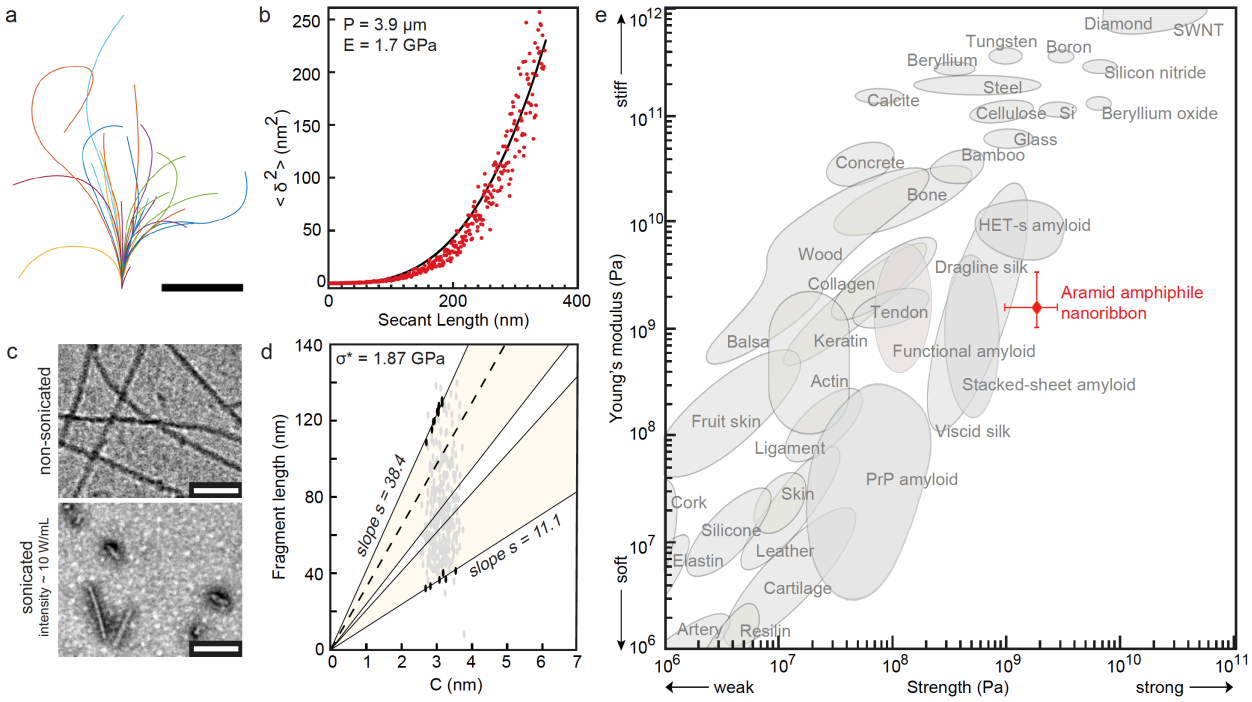

Figure 2.10. Aramid amphiphile nanoribbons have a Young's modulus of E = 1.7 GPa, and a tensile strength of σ* = 1.9 GPa. **a**, Contours acquired by tracing the AFM profiles of 29 AA nanoribbons are used for statistical topographical analysis (scale bar, 1 μm). **b**, Midpoint deviations δ from contour traces are used to calculate a persistence length, P = 3.9 ± 0.7 μm and Young's modulus, E = 1.7 ± 0.7 GPa, from least-squares fitting of a worm-like chain model for semi-flexible polymers to the data. **c**, Sonication-induced scission of nanoribbons, carried out with approximately 10 W/mL horn sonication, is illustrated by TEM (scale bars, 100 nm). **d**, The threshold length L_{lim} below which a fibril will not break under sonication is determined from plotting sonicated fragment lengths against cross-sectional size, C. The yellow areas illustrate the broadened boundaries of the terminal range defined by [$L_{lim}/2$, L_{lim}], and the dashed line represents the average L_{lim}.[48] The tensile strength of AA nanoribbons is calculated to be σ* = 1.87 ± 1.00 GPa. **e**, AA nanoribbon mechanical properties, shown on an Ashby plot, place it among the strongest and stiffest biological materials.[48] Young's modulus and tensile strength values are reported as mean ± standard deviation.

A simple strategy for aligning self-assembled nanofibers into 1-dimensional gels in water has been previously demonstrated.[69] In this approach, peptide amphiphiles were thermally annealed to form liquid crystalline bundles, which were shear aligned in divalent counterion solution to produce macroscopic 1-dimensional gels.[69] These gels have been used for applications including cell scaffolding and protein delivery.[69, 113] We harnessed this processing strategy by annealing cationic nanoribbons (compound **3**) in water and pulling the suspension through a salt solution (Na_2SO_4) on a glass slide (Figure 2.1d). This process leads to the formation of a 1-dimensional gel that exhibits birefringence under polarized light (Figure 2.11a), indicating that the nanoribbons are aligned within the gel. We demonstrate the unique ability of the nanoribbon gel to withstand drying in air, forming a stable solid thread that can be handled, bent without breaking (Figure 2.1e), and can support over 200 times its weight (Figure 2.11b). Scanning electron microscopy (SEM) imaging of the AA threads in vacuum reveal thread diameters near 20 μm and striations consistent with the presence of nanoribbon bundles (Figure 2.12).

The formation of solid-state nanoribbon threads requires that individual nanoribbons exhibit significant structural integrity, which in the case of AAs is imparted by their aramid domain. However, neither the Young's modulus nor tensile strength of nanoribbons is expected to govern the threads' bulk mechanical properties. Rather, electrostatics dominate interribbon interactions, an effect that has been previously demonstrated at highly charged nanoscale surfaces.[114] We hypothesize that adjusting the nanoribbon surface chemistry and counterion pair provides a route to adjusting the elastic modulus and extensibility of the thread. Consistent with this hypothesis, we find that gelation is only possible when the counterion valency is greater than one.

We performed tensile tests to determine the effect of counterion charge density on the threads' elastic moduli and extensibilities (Figure 2.11c), providing a benchmark for future studies. Threads formed with two divalent anions, one with a high charge density, sulfate, and one with a lower charge density, methanedisulfonate, were measured. Threads with sulfate and methanedisulfonate counterions produced Young's moduli of 637 ± 114 MPa and 385 ± 77 MPa, respectively. As one point of comparison, the observed modulus values fall on the same order of magnitude as polyethylenes.[115] Further, we find

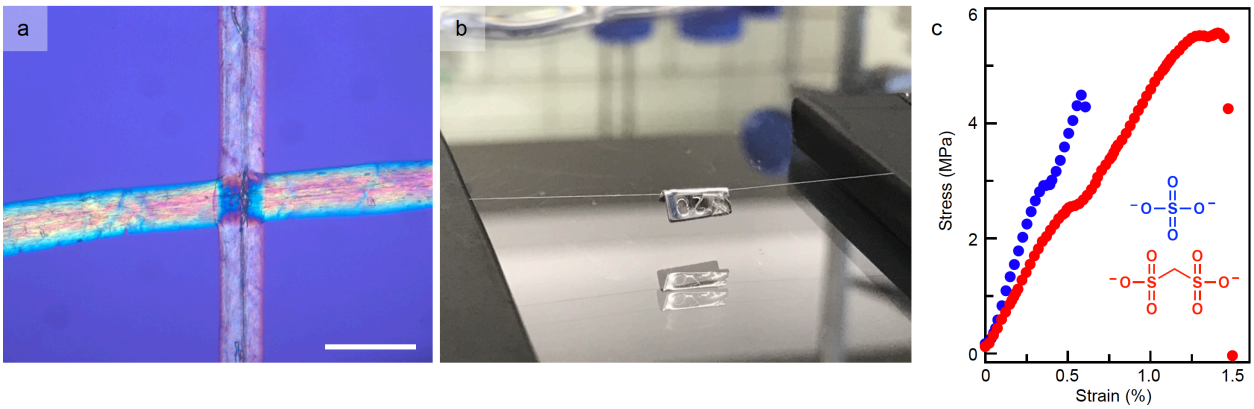

Figure 2.11 l Aramid amphiphile nanoribbons are aligned by shear forces and dried to form flexible threads. **a**, A polarized light micrograph shows the intersection of two nanoribbon threads. The birefringence observed under cross-polarizers indicates the nanoribbons are aligned within the threads (scale bar, 100 μm). **b**, A 5 cm nanoribbon thread whose mass totals 0.1 mg is suspended over a trough and supports a 20 mg weight. **c**, Representative tensile tests of AA threads formed with sulfate (blue) and methanedisulfonate (red) counterions are shown. Tensile tests of twelve samples reveal Young's moduli of 637 ± 114 MPa and 385 ± 77 MPa, respectively, and extensibility values of 0.6 ± 0.2 % and 1.1 ± 0.2 %, respectively. Data are reported as mean ± standard deviation.

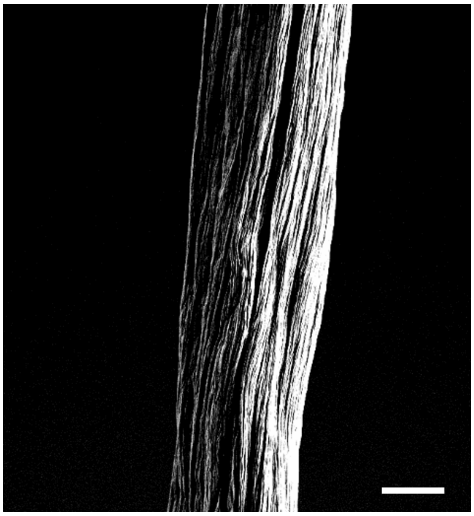

Figure 2.12 l Scanning electron microscopy of a 20 μm-diameter nanoribbon thread shows long-range alignment of nanoribbon bundles (scale bar, 10 μm).

that threads with the methanedisulfonate anion (elongation at break, $\varepsilon_{break} = 1.1 \pm 0.2$ %) are nearly twice as extensible as threads formed with the sulfate anion ($\varepsilon_{break} = 0.6 \pm 0.2$ %). We attribute the enhanced elastic modulus and decrease in extensibility of threads with sulfate counterions, compared to those with methanedisulfonate counterions, to the enhanced electrostatic interaction strengths between nanoribbons with counterions of greater charge densities.[116] These experiments reveal that nanoribbon surface and counterion chemistry are viable parameters to vary for controlling bulk mechanical properties.

We used X-ray scattering to study the structure within the nanoribbon thread and to confirm that nanoribbons remain intact after alignment and drying (Figure 2.13a). Wide-angle X-ray scattering (WAXS) of the dried thread in vacuum shows anisotropic peaks indicating nanoribbon alignment, with the strongest WAXS peak occurring at a d-spacing of 5.05 Å (Figure 2.13b). WAXS patterns of vertically oriented nanoribboon threads were collected and integrated to yield meridional and equitorial peaks. From these peaks, a simulated unit cell shows molecular packing resembling poly(*p*-benzamide) (Figure 2.13c).[117] This structure implies that even upon drying in vacuum, where the hydrophobic effect is absent, intermolecular aramid hydrogen bonding is dominant along the nanoribbon long axis with H-O hydrogen bond distances of 2.08 Å. Further, we infer that π-π stacking at an interplane distance of 3.61 Å laterally holds together hydrogen bonded sheets across the nanoribbon width (Figure 2.13d).

The anisotropy observed by X-ray scattering confirms the geometric configuration of the AA structures as nanoribbons within the solid-state thread. The uniform intermolecular distances of 5.05 Å observed along the length of the nanoribbon indicate that an extended hydrogen bonding network is likely unincumbered by torsion or strain. This observation is consistent with the absence of helical nanoribbons, as well as the extraordinary nanoribbon lengths. The attractive forces along the nanoribbon width are significantly weaker, dominated by π-π stacking at an off-ribbon axis angle of 64°. This π-π stacking enables lateral growth of the ribbons, but leads to dimensions of only approximately 5 nm in width. Differences in intermolecular interaction strength along the

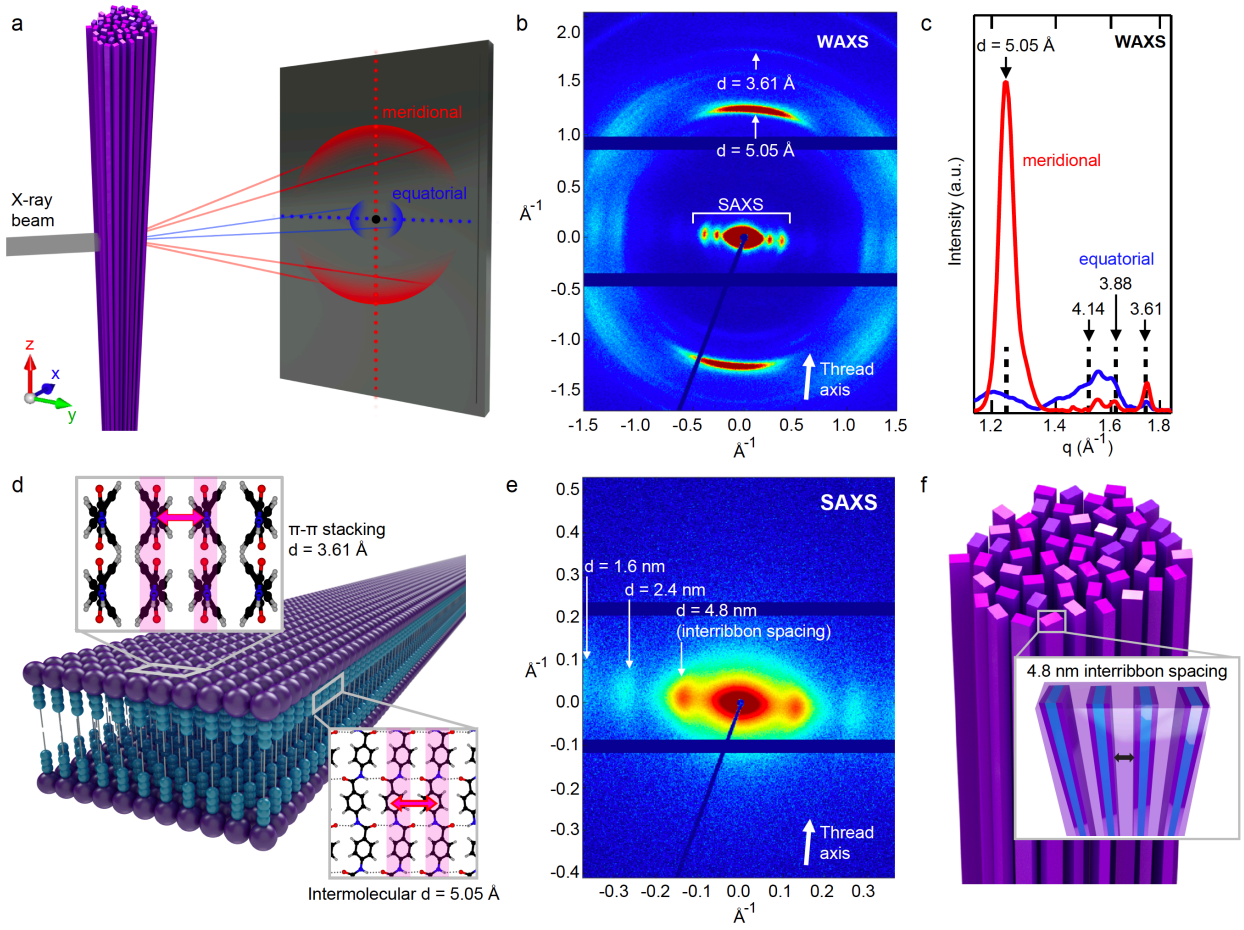

Figure 2.13 | X-ray scattering of solid-state nanoribbon threads demonstrates organized molecular packing, extended hydrogen bonding networks, and long-range hierarchical order. **a**, Meridional and equatorial scattering directions are depicted in X-ray scattering measurements of solid, aligned AA nanoribbon threads. **b**, A WAXS pattern of an AA nanoribbon thread indicates that precise molecular organization is maintained in the solid state, with significant anisotropy indicating nanoribbon alignment. **c**, A 1-D scattering profile is obtained by integrating meridional and equatorial axes of (b). Black dotted lines are simulated peak positions of a unit cell with a = 7.22 Å, b = 5.05 Å, and c = 11.10 Å, and space group 26:*P*mc2$_1$ based on poly(*p*-benzamide). **d**, Molecular packing in AA nanoribbons is illustrated as informed by the simulated unit cell in (c). 5.05 Å intermolecular distances are observed, corresponding to H-bonds of 2.08 Å (dotted lines in bottom inset) that form a network down the long-axis of the nanoribbon. 3.61 Å intermolecular π-π stacking lies at a 64° tilt with respect to the hydrogen bonding plane. Based on these distances, the surface area of AA nanoribbons within the thread is 200 m^2/g. **e**, SAXS of an AA nanoribbon thread shows anisotropic lamellar peaks corresponding to a 4.8 nm interribbon spacing. **f**, A hypothesized structure shows the alignment of individual AA nanoribbons to form semi-crystalline domains with 4.8 nm lamellar spacings informed by (e).

nanoribbon long axes versus across the widths have previously been shown to lead to high-aspect-ratio nanoribbons as opposed to lamellar sheets.[27]

While X-ray scattering supports the presence of nanoribbon geometries with rectangular cross-sections, this technique is largely insensitive to disordered and highly hydrated domains such as the head group domains of AA nanoribbons. Therefore, the scattering information used to designate the nanoribbons as planar with rectangular cross-sections arises primarily from the structured aramid domains. In reality, the head group domains of the nanoribbon are likely to survey the space surrounding the energetically disfavorable hydrophobic edge, shielding this region from solvent. The ability of the head groups to shield the nanoribbon edge is determined by head group size, hydration, and intermolecular electrostatic repulsion. Consequences of this effect include that the nanoribbon cross-sections are not perfectly rectangular but are rather distorted around the hydrophobic edge. Further, the nanoribbon width should be variable and sensitive to head group chemistry, while the length and thickness are not. To test this hypothesis, we synthesized AAs with neutral oligoethylene glycol head groups (Figure 2.14). OEG-AA is expected to exhibit minimal head group repulsion, leading to wider nanoribbons. Upon self-assembly in water, OEG-AA nanoribbon thicknesses and lengths are found to be comparable to nanoribbons of **1**, **2**, and **3**. Consistent with our hypothesis, we find their widths to be greater than those of **1**, **2**, and **3** nanoribbons, measured by cryo-TEM to be 7.0 nm (Figure 2.14).

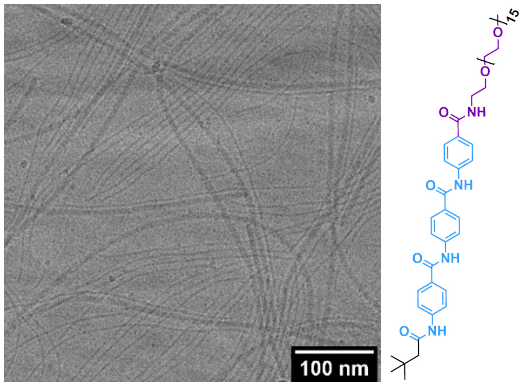

Figure 2.14 l Representative cryo-TEM image of the self-assembled nanostructure constructed of aramid amphiphiles with a 15-mer oligo(ethylene glycol) head group, OEG-AA.

Using the dimensions and spacings of compound **3** nanoribbons determined by X-ray scattering, we calculate a surface area within the dried thread as 200 m^2/g. At longer length scales, SAXS peaks in the equatorial direction result from AA nanoribbons aligned along the thread axis (Figure 2.13e), with 4.8 nm spacings between nanoribbons (Figure 2.13f). This spacing implies that most of the nanoribbon surfaces are accessible, even in the solid-state. AA threads offer precise internal molecular structure, uniform interribbon spacings, and tunable nanoribbon surface chemistries in a macroscopic 1-dimensional material from small molecule amphiphilic self-assembly.[78, 79, 118]

We have presented a molecular self-assembly platform, the aramid amphiphile (AA). Six hydrogen bonds fix each AA molecule within an extended network, which, when combined with lateral π-π stacking, gives rise to nanoribbons with 4 nm thicknesses, 5-6 nm widths, and lengths of up to 20 micrometers. These nanoribbons exhibit slow molecular exchange dynamics, and tensile strengths and Young's moduli on the order of gigapascals. We apply a shear alignment technique to form macroscopic threads composed of aligned nanoribbon bundles with uniform 4.8 nm interribbon spacings and surface areas of 200 m^2/g. We propose choice of nanoribbon head group and counterion chemistry as features that may be modified to optimize bulk mechanical properties. Further, we demonstrate that these nanoribbon threads are flexible, can be handled, and can support 200 times their weight, making them suitable for solid-state applications. The aramid amphiphile platform overcomes dynamic instabilities common in supramolecular small molecule assemblies and provides a route to nanostructured, solid-state molecular materials.

Methods

Synthesis and materials

The syntheses used in this study involve (1) carbodiimide-mediated coupling reactions to form amide linkages, (2) conventional deprotection reactions of *tert*-butyloxycarbonyl (Boc) and (3) hydrolysis of ester functionalities to produce carboxylic acid moieties. As the only exception, the zwitterionic head group of **2** is obtained by

quaternization of a tertiary amine with a propanesultone. Both ^{1}H and ^{13}C nuclear magnetic resonance (NMR; Bruker Avance III DPX 400) and mass spectrometry (MS; Bruker Omniflex) were used to confirm the chemical composition of intermediates and products. The observed solubilities of **1** and **2** are up to 1.0 mg/mL, and the solubility of **3** exceeds 20 mg/mL. Synthesis details on each of compounds **1**, **2**, **3**, OEG-AA and the FRET donor- and quencher-labelled AAs and their intermediates are provided in respective sections below.

Methyl 4-aminobenzoate (Sigma Aldrich, 98%), 3,3-dimethylbutyric acid (Sigma Aldrich, 98%), *N,N*-dimethyl-*p*-phenylenediamine (DPP, Sigma Aldrich, 97%), *N*-Boc-*p*-phenylenediamine (BPP, Sigma Aldrich, 97%), 1,3-propanesultone (PPS, Sigma Aldrich, 99%), 1,4-bis-Boc-1,4,7-triazaheptane (BBT, Chem Impex, 100%), diethylenetriamine-*N,N,N'',N''*-tetra-*tert*-butyl acetate-*N'*-acetic acid (DPTA, Combi Blocks, 95%), methoxypolyethylene glycol amine (Sigma Aldrich), 1-ethyl-3-(3-dimethylaminopropyl)carbodiimide hydrochloride (EDC, TCI Chemicals, 98%), 4-dimethylaminopyridine (DMAP, TCI Chemicals, 99%), 1-hydroxybenzotriazole hydrate (HOBt, TCI Chemicals, 97%), *N,N*-Diisopropylethylamine (DIPEA, Alfa Aesar, 99%), lithium hydroxide (LiOH, Alfa Aesar, 98%), sodium bicarbonate ($NaHCO_3$, Alfa Aesar, 99%), hydrochloric acid (HCl, Alfa Aesar, 36%), sodium sulfate (Na_2SO_4, Fisher Scientific, 99%), and trifluoroacetic acid (TFA, Alfa Aesar, 99%) were used as received without further purification.

Synthesis of the anionic aramid amphiphile and its intermediates

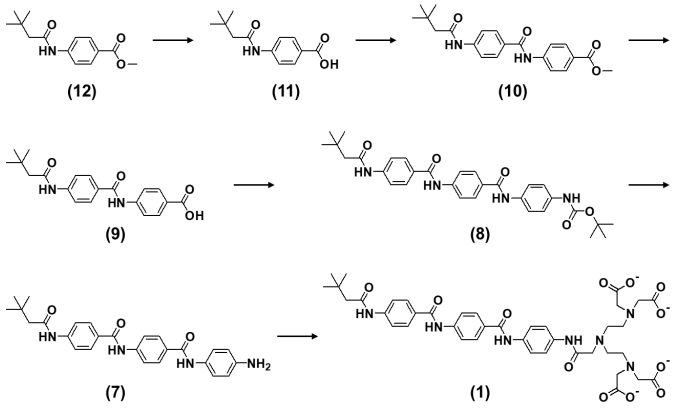

Scheme 2.1 I Synthesis scheme to obtain anionic amphiphile.

Methyl 4-(3,3-dimethylbutanamido)benzoate (**12**): A solution of methyl 4-aminobenzoate (11.01 mmol), 3,3-dimethylbutyric acid (16.52 mmol), EDC (33.03 mmol), and DMAP (33.03 mmol) in tetrahydrofuran (50 mL) was stirred at room temperature for 24 h. After the reaction, the solvent was removed in vacuum, and the residue was washed with distilled water and extracted in chloroform. The organic layer was purified by column chromatography with silica gel by using 1:1 ethyl acetate:hexane by volume (yield: 72%). ^{1}H NMR (400 MHz, DMSO-*d*): δ = 7.89 (d, 2H), 7.75 (d, 2H), 3.82 (s, 3H), 2.23 (s, 2H), 1.03 (s, 9H) ppm.

4-(3,3-dimethylbutanamido)benzoic acid (**11**): 10 M LiOH (10 mL) was added to a stirred solution of compound **12** (4.25 mmol) in ethanol (40 mL). The mixture was heated to 60°C and refluxed for 3 h, and then neutralized with an aqueous HCl solution. The precipitate was filtered off, and washed with water several times. The crude product was purified by reprecipitation from chloroform and methanol and dried under vacuum (yield: 98%). ^{1}H NMR (400 MHz, DMSO-*d*): δ = 7.87 (d, 2H), 7.72 (d, 2H), 2.23 (s, 2H), 1.03 (s, 9H) ppm.

Methyl 4-(4-(3,3-dimethylbutanamido)benzamido)benzoate (**10**): EDC (6.37 mmol), and DMAP (6.37 mmol) were added to a solution of compound **11** (2.13 mmol), and methyl 4-aminobenzoate (6.37 mmol) in dimethylformamide (30 mL). The solution was stirred for 24 h at 50 °C. After the reaction, the solvent was removed in vacuum, and the remaining residue was precipitated in water. The crude mixture was collected with filter flask. The filtered solid was washed with excess methanol and dried in vacuum (yield: 83%). ^{1}H NMR (400 MHz, DMSO-*d*): δ = 7.95 (m, 6H), 7.77 (d, 2H), 3.84 (s, 3H), 2.24 (s, 2H), 1.04 (s, 9H) ppm.

4-(4-(3,3-dimethylbutanamido)benzamido)benzoic acid (**9**): 10M LiOH (10 mL) was added to a stirred solution of compound **10** (2.55 mmol) in tetrahydrofuran (20 mL) and ethanol (10 mL). The mixture was refluxed for 6 h and then neutralized with an aqueous HCl solution. The precipitate was filtered off, washed with water, and dried under vacuum to afford the product (yield: 98%). ^{1}H NMR (400 MHz, DMSO-*d*): δ = 7.93 (m, 6H), 7.76 (d, 2H), 2.24 (s, 2H), 1.04 (s, 9H) ppm.

tert-Butyl 4-(4-(4-(3,3-dimethylbutanamido)benzamido)benzamido)phenylcarbamate (**8**): Into dimethylformamide (20 mL), compound **9** (0.85 mmol), BPP (2.55 mmol), EDC (2.55 mmol), and DMAP (2.55 mmol) were added. The well-dissolved solution was stirred at room temperature for 24 h. After solvent evaporation, the crude mixture was washed with water and methanol to give the desired white solid product (yield: 81%). ^{1}H NMR (400 MHz, DMSO-*d*): δ = 7.96 (m, 6H), 7.77 (d, 2H), 7.64 (d, 2H), 7.41 (d, 2H), 2.25 (s, 2H), 1.46 (s, 9H), 1.05 (s, 9H) ppm.

N-(4-(amino)phenyl)-4-(4-(3,3-dimethylbutanamido)benzamido)benzamide (**7**): TFA (500 µL) was added dropwise into the solution of compound **8** (0.55 mmol) in methylene chloride (15 mL). After stirring the mixture for 6 h at room temperature, the volatiles were distilled off and the remaining mixture was washed with saturated $NaHCO_3$ solution. The solid precipitate was filtered and dried in vacuum (yield: 99%). ^{1}H NMR (400 MHz, DMSO-*d*): δ = 7.95 (m, 6H), 7.75 (d, 2H), 7.48 (d, 2H), 6.72 (d, 2H), 2.25 (s, 2H), 1.05 (s, 9H) ppm.

2,2',2'',2'''-((((2-((4-(4-(4-(3,3-dimethylbutanamido)benzamido)benzamido)phenyl)amino)-2-ox-oethyl)azanediyl)bis(ethane-2,1-diyl))bis(azanetriyl))tetraacetate (**1**): A solution of compound **7** (0.29 mmol), DPTA (058 mmol), EDC (1.17 mmol), and DMAP (1.17 mmol) in dimethylformamide (20 mL) was stirred at 50 °C for 72 h. After the reaction, the solvent was removed in vacuum. The remaining residue was purified by flash column chromatography with silica gel by using 7:1 tetrahydrofuran : chloroform by volume as an eluent. The isolated compound was then reacted with TFA (500 µL) in methylene chloride (15 mL) for 48 h. The volatile fraction was removed under reduced pressure. Tetrahydrofuran was added to suspend the product and the product was collected by filtration (yield: 67%). ^{1}H NMR (400 MHz, DMSO-*d*): δ = 7.97 (m, 6H), 7.75 (m, 4H), 7.61 (d, 2H), 4.06 (s, 2H), 3.51 (s, 8H), 3.21 (t, 4H), 3.01 (t, 4H), 2.25 (s, 2H), 1.05 (s, 9H) ppm. ^{13}C NMR (400 MHz, DMSO-*d*): δ = 173.2, 170.9, 165.6, 165.1, 142.9, 135.7, 134.4, 128.9, 121.2, 119.8, 118.7, 55.1, 52.8, 50.1, 31.4, 30.1 ppm. MS (MALDI-ToF) m/z $[M + H]^+$ calculated: 820.34; $[M + H]^+$ found: 820.35.

Synthesis of the zwitterionic aramid amphiphile and its intermediates

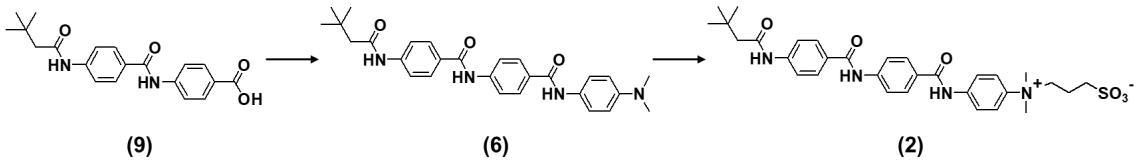

Scheme 2.2 I Synthesis scheme to obtain zwitterionic aramid amphiphile.

N-(4-(dimethylamino)phenyl)-4-(4-(3,3-dimethylbutanamido)benzamido)benzamide (**6**): A solution of compound **9** (0.85 mmol), DPP (2.55 mmol), EDC (2.55 mmol), and HOBt (2.55 mmol) in dimethylformamide (20 mL) was stirred at 50 °C for 24 h. After the reaction, the solvent was distilled off and the remaining residue was precipitated with water. The crude mixture was collected and washed with chloroform several times (yield: 78%). ^{1}H NMR (400 MHz, DMSO-*d*): δ = 7.95 (m, 6H), 7.77 (d, 2H), 7.57 (d, 2H), 6.73 (d, 2H), 2.88 (s, 6H), 2.25 (s, 2H), 1.05 (s, 9H) ppm.

3-((4-(4-(4-(3,3-dimethylbutanamido)benzamido)benzamido)phenyl)dimethylammonio)-propane-1-sulfonate (**2**): Compound **6** (1.85 mmol) was dissolved in dimethylformamide (15 mL) and tetrahydrofuran (15 mL). PPS (5 mL) was slowly injected using a syringe and the clear solution was stirred for 48 h in a sealed pressure tube at 70 °C. The volatile fraction was removed under reduced pressure and acetonitrile (50 mL) was added. The resulting precipitate was filtered and dried in vacuum (yield: 85%). ^{1}H NMR (400 MHz, DMSO-*d*): δ = 7.98 (m, 8H), 7.90 (d, 2H), 7.78 (d, 2H), 3.99 (m, 2H), 3.58 (s, 6H), 2.39 (t, 2H), 1.66 (m, 2H), 1.05 (s, 9H) ppm. ^{13}C NMR (400 MHz, DMSO-*d*): δ = 170.9, 165.8, 143.2, 140.9, 139.6, 129.1, 122.2, 121.1, 119.8, 118.7, 68.1, 54.4, 50.1, 47.9, 34.4, 30.1, 20.3 ppm. MS (MALDI-ToF) $[M + H]^+$ m/z calculated: 595.26; $[M + H]^+$ found: 595.41.

Synthesis of the cationic amphiphile and its intermediates

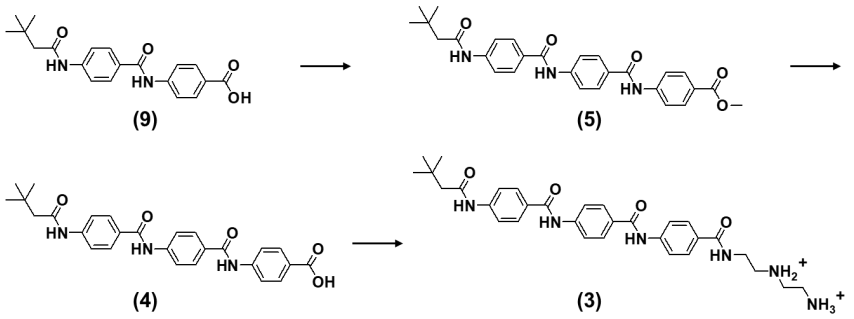

Scheme 2.3 I Synthesis scheme to obtain the cationic aramid amphiphile.

Methyl 4-(4-(4-(3,3-dimethylbutanamido)benzamido)benzamido)benzoate (**5**): EDC (4.23 mmol) and DMAP (4.23 mmol) were added to a solution of compound **9** (1.41 mmol) and methyl 4-aminobenzoate (4.23 mmol) in dimethylformamide (20 mL). The solution was stirred for 24 h at 50 °C. After the reaction, the solvent was removed in vacuum, and the remaining residue was precipitated with water. The collected crude mixture was further washed with methanol and dried in vacuum (yield: 75%). ^{1}H NMR (400 MHz, DMSO-*d*): δ = 7.97 (m, 8H), 7.78 (d, 2H), 3.85 (s, 3H), 2.25 (s, 2H), 1.05 (s, 9H) ppm.

4-(4-(4-(3,3-dimethylbutanamido)benzamido)benzamido)benzoic acid (**4**): 10M LiOH (10 mL) was added to a stirred solution of compound **5** (1.05 mmol) in tetrahydrofuran (20 mL), and ethanol (10 mL). The mixture was refluxed for 12 h and then neutralized with an aqueous HCl solution to obtain a precipitate. The crude product was purified by reprecipitation with chloroform and ethanol and dried under vacuum (yield: 93%). ^{1}H NMR (400 MHz, DMSO-*d*): δ = 7.94 (m, 8H), 7.78 (d, 2H), 2.25 (s, 2H), 1.05 (s, 9H) ppm.

1-(2-(4-(4-(4-(3,3-dimethylbutanamido)benzamido)benzamido)benzamido)ethyl)-ethane-1,2-diaminium (**3**): A solution of compound **4** (0.42 mmol), BBT (1.27 mmol), EDC (1.27 mmol), HOBt (1.27 mmol) and DIPEA (1.27 mmol) in dimethylformamide (20 mL) and dichloromethane (20 mL) was stirred at room temperature for 24 h. After the reaction, the solvent was removed in vacuum, and the remaining residue was washed with water several times. The isolated compound was then reacted with TFA (4 mL) in methylene

chloride (40 mL) for 24 h. The volatile fraction was evaporated under reduced pressure. Diethyl ether was added to collect the product by filtration (yield: 85%). ^{1}H NMR (400 MHz, DMSO-*d*): δ = 7.98 (m, 10H), 7.76 (d, 2H), 3.58 (m, 2H), 3.39 (m, 2H), 3.13 (m, 4H), 2.25 (s, 2H), 1.04 (s, 9H) ppm. ^{13}C NMR (400 MHz, DMSO-*d*): δ = 171.1, 167.1, 165.7, 142.9, 129.1, 128.7, 128.4, 120.1, 119.4, 118.7, 50.1, 47.4, 44.6, 35.8, 31.4, 30.1 ppm. MS (MALDI-ToF) $[M + H]^+$ m/z calculated: 559.30; $[M + H]^+$ found: 559.29.

Synthesis of compounds for Förster resonance energy transfer

Molecular exchange was measured by Förster resonance energy transfer (FRET) dark quenching when two nanoribbon populations, one containing a donor fluorophore and the other containing a dark quencher, were introduced into the same suspension. EDANS ((5-((2-aminoethyl)amino)naphthalene-1-sulfonic acid)) was used as the donor fluorophore and DABCYL (4-(dimethylaminoazo)benzene-4-carboxylic acid) was used as the dark quencher.

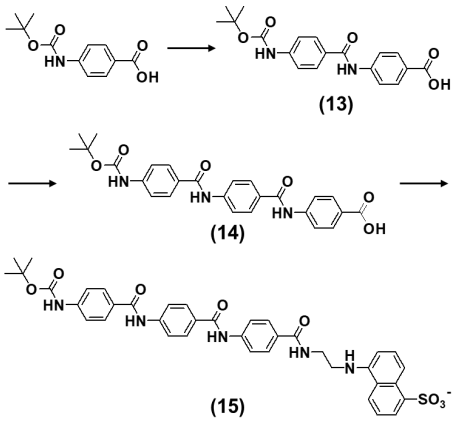

Scheme 2.4 I Synthesis scheme to obtain the EDANS-tagged amphiphile.

4-(4-(*tert*-Butoxycarbonyl)benzamido)benzoic acid (**13**): A solution of 4-(Boc-amino)benzoic acid (4.21 mmol), methyl 4-aminobenzoate (8.42 mmol), EDC (8.42 mmol), and DMAP (8.42 mmol) in chloroform (100 mL) were stirred at room temperature for 12 h. After the reaction, the solvent was evaporated under reduced pressure, and the remaining residue was precipitated with water. The mixture was filtered, and the

precipitate was washed with methylene chloride several times. The solid material was dissolved in tetrahydrofuran (40 mL) and ethanol (20 mL). LiOH (21.1 mmol) in water (10 mL) was added to this solution, which was then refluxed at 70 °C for 3 h. The reaction mixture was shifted to room temperature and acidified to pH 2 with the addition of 5M HCl solution. The precipitate was collected by filtration and dried in vacuum (yield: 87%). ^{1}H NMR (400 MHz, DMSO-*d*): δ = 7.93 (m, 6H), 7.66 (d, 2H), 1.49 (s, 9H) ppm.

4-(4-(4-(*tert*-Butoxycarbonyl)benzamido)benzamido)benzoic acid (**14**): A solution of compound **13** (2.11 mmol), methyl 4-aminobenzoate (4.22 mmol), EDC (4.22 mmol), and DMAP (4.22 mmol) were in dimethylformamide (30 mL) was stirred at room temperature for 24 h. After the reaction, the solvent was distilled off, and the remaining residue was washed with water and methanol. The solid material was dissolved in tetrahydrofuran (20 mL) and ethanol (10 mL). LiOH (10.5 mmol) in water (10 mL) was added to this solution, which was then refluxed at 70 °C for 6 h. The reaction mixture was shifted to room temperature and acidified to pH 2 with the addition of 5M HCl solution. The precipitate was collected by filtration and dried in vacuum (yield: 82%). ^{1}H NMR (400 MHz, DMSO-*d*): δ = 7.95 (m, 10H), 7.67 (d, 2H), 1.49 (s, 9H) ppm.

EDANS-tagged amphiphile, 5-((2-(4-(4-(4-(3,3-dimethylbutanamido)benzamido-)benzamido)benzamido)ethyl)amino)naphthalene-1-sulfonic acid (**15**): A solution of compound **14** (0.21 mmol), EDC (0.25 mmol), and DMAP (0.25 mmol) in dimethylformamide (10 mL) was stirred for 30 min. EDANS (0.25 mmol) was then added into the solution and the solution was stirred for 24 h at room temperature. Water was poured into the solution to yield a precipitate, which was obtained by filtration and washed with chloroform (yield: 64%). ^{1}H NMR (400 MHz, DMSO-*d*): δ = 8.02 (m, 1H), 7.97 (m, 10H), 7.62 (d, 2H), 7.34 (m, 4H), 6.57 (d, 1H), 3.85 (m, 1H), 3.43 (m, 2H), 3.16 (m, 2H), 1.51 (s, 9H) ppm. MS (MALDI-ToF) $[M + H]^+$ m/z calculated: 723.23; $[M + H]^+$ found: 723.24.

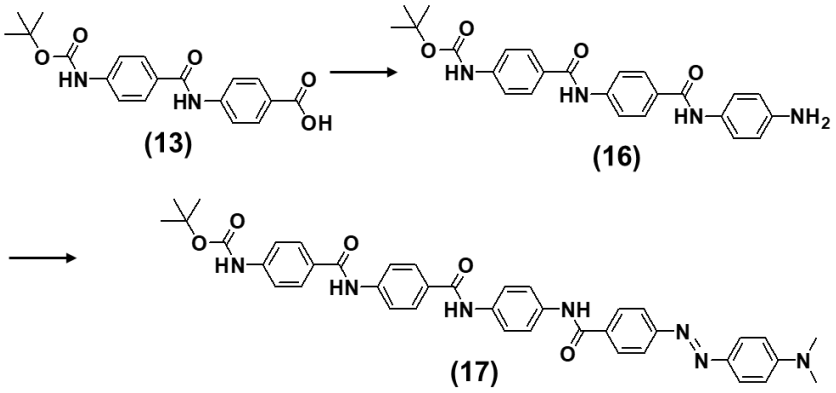

Scheme 2.5 I Synthesis scheme to obtain the DABCYL-tagged amphiphile.

tert-Butyl 4-((4-((4-aminophenyl)carbamoyl)phenyl)carbamoyl)phenylcarbamate (**16**): A solution of compound **13** (0.56 mmol), 1,4-diaminobenzene (11.22 mmol), EDC (0.67 mmol), and DMAP (0.67 mmol) in dimethylformamide (80 mL) was stirred at 25 °C for 24 h. The volatile fraction was removed under reduced pressure and the remaining residues were washed several times with methanol and filtered to obtain the product (yield: 59%). ^{1}H NMR (400 MHz, DMSO-*d*): δ = 7.92 (m, 6H), 7.60 (d, 2H), 7.36 (d, 2H), 6.54 (d, 2H), 4.91 (s, 2H), 1.51 (s, 9H) ppm.

DABCYL-tagged amphiphile, (E)-4-((4-(dimethylamino)phenyl)diazenyl)-N-(4-(4-(4-(3,3-dimethylbutanamido)benzamido)benzamido)phenyl)benzamide (**17**): A solution of compound **16** (0.67 mmol), DABCYL (0.81 mmol), EDC (0.81 mmol), and DMAP (0.81 mmol) in dimethylformamide (10 mL) was stirred at 25 °C for 48 h. The solvent was then evaporated under reduced pressure. The crude mixtures were purified with water and chloroform and filtered to obtain the product (yield: 71%). ^{1}H NMR (400 MHz, DMSO-*d*): δ = 7.94 (m, 12H), 7.62 (d, 4H), 7.45 (d, 2H), 6.66 (d, 2H), 3.10 (s, 6H), 1.51 (s, 9H) ppm. MS (MALDI-ToF) $[M + Na]^+$ m/z calculated: 720.29; $[M + Na]^+$ found: 720.30.

Synthesis of the oligo(ethylene glycol) amphiphile

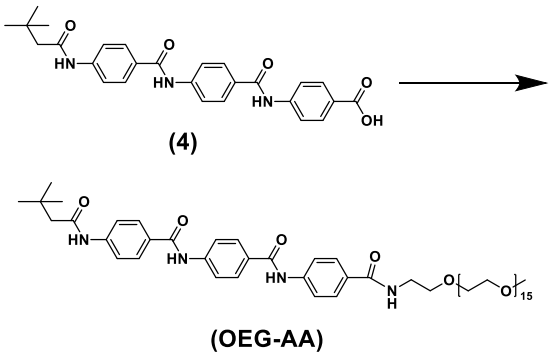

Scheme 2.6 I Synthesis scheme to obtain the oligo(ethylene glycol) amphiphile.

N-(4-((2,5,8,11,14,17,20,23,26,29,32,35,38,41,44,47-hexadecaoxanonatetracontan-49-yl)carbamoyl)phenyl)-4-(4-(3,3-dimethylbutanamido)benzamido)benzamide (**OEG-AA**): A solution of compound **4** (0.1 mmol), methoxypolyethylene glycol amine (M_w = 750 g/mol, 0.2 mmol), EDC (0.2 mmol), and HOBt (0.2 mmol) in dimethylformamide (10 mL) was stirred at rt for 24 h. The solvent was then evaporated under reduced pressure and the remaining residue was dissolved in dichloromethane. The solution was washed by ice water twice via solvent extraction and the organic fraction in dichloromethane was retained. The final product in dichloromethane was obtained by removing the solvent under reduced pressure and lyophilizing the remaining semi-solid (yield: 62%). ^{1}H NMR (400 MHz, DMSO-*d*): δ = 7.97 (m, 6H), 7.84 (m, 2H), 7.76 (d, 2H), 7.49 (d, 2H), 3.51 (s, 70H), 2.25 (m, 2H), 1.05 (s, 9H) ppm. Major peak: MS (MALDI-ToF) $[M + Na]^+$ m/z calculated for n = 15 is 1213.64; $[M + Na]^+$ Found: 1213.61. Minor peak: MS (MALDI-ToF) $[M + Na]^+$ m/z calculated for n = 13 is 1125.58; $[M + Na]^+$ Found: 1125.56. Minor peak: MS (MALDI-ToF) $[M + Na]^+$ m/z calculated for n = 14 is 1169.61; $[M + Na]^+$ Found: 1169.59. Minor peak: MS (MALDI-ToF) $[M + Na]^+$ m/z calculated for n = 16 is 1257.66; $[M + Na]^+$ Found: 1257.64. Minor peak: MS (MALDI-ToF) $[M + Na]^+$ m/z calculated for n = 17 is 1301.69; $[M + Na]^+$ Found: 1301.67

Shear alignment to form macroscopic AA threads

A 2.0 wt% aqueous solution of **3** was bath sonicated for 24 h, rested for 12 h, annealed in a heating block at 80 °C for 10 h and then slowly cooled to room temperature. This solution was extruded into a bath of 40 mM sodium sulfate (Na_2SO_4) or 40 mM disodium methanedisulfonate ($Na_2CH_2S_2O_6$) to produce one-dimensional gels, which were pulled out of the solution and dried under ambient conditions to form the final macroscopic AA threads.

Infrared spectroscopy

ATR-FTIR spectra of aqueous samples of compound **3** dissolved at a 20 mg/mL concentration in deuterated water (D_2O) were acquired using an ATR-FTIR spectroscope (Bruker ALPHA II) at room temperature with a diamond crystal. Three different solvent ratios were used (D_2O/DMSO = 50:50, 75:25 and 100:0), and spectra were captured upon mixing sample into the solvent as well as with 10 min, 1 h and 24 h of bath sonication after mixing. Solvent background with the same sonication time was subtracted from each spectra, and the spectra were normalized to the amide I stretching peak at 1,672 cm^{-1}. D_2O was selected in place of water to provide less interference in the infrared region of interest.

Powder FTIR spectra were acquired on a Thermo Fisher Scientific Nicolet 6700. Potassium bromide pellets were prepared by mixing 0.1 mg of lyophilized sample with 0.5 g of KBr (Fisher Scientific, FTIR grade). The ambient background of carbon-dioxide-free air was subtracted from each spectra.

Transmission electron microscopy

TEM images were captured on an FEI Tecnai G2 Spirit TWIN microscope at an accelerating voltage of 120 kV. Grids were prepared by depositing 10 µl of a 1 mg/mL amphiphile solution onto a continuous carbon grid (Electron Microscopy Sciences, 200 mesh, copper) for 20 s, blotting to remove the solution, depositing 10 µl of a 0.1% phosphotungstic acid solution onto the grid (Electron Microscopy Sciences) and blotting to remove the stain.

X-ray scattering

SAXS samples were prepared by dissolving lyophilized powders of **1**, **2** and **3** in deionized water above the solubility limit. To avoid artefacts associated with nanostructure aggregation, each sample was centrifuged at 3,000 r.p.m. and its supernatant was loaded into 2-mm-diameter quartz capillary tubes (Hampton Research). Variable temperature SAXS profiles were performed on compounds **1** and **2** in water at 1 mg/mL, and on **3** at 20 mg/mL.

Solution SAXS measurements and WAXS measurements on nanoribbon threads were performed at Beamline 12-ID-B of the Advanced Photon Source at Argonne National Laboratory with an X-ray radiation energy of 13.3 keV. DECTRIS PILATUS 300 K and PILATUS 2 M detectors were used for SAXS and WAXS, respectively. The two-dimensional X-ray scattering patterns were background subtracted to remove the water and capillary background, and processed using beamline software for reduction to one-dimensional data curves. The higher resolution of the compound **3** SAXS profile relative to those of compounds **1** and **2** is due to the notably higher solubility of compound **3**.

SAXS profiles of AA nanoribbons best fit to a core-shell lamellar model, which describes a lyotropic lamellar phase with head and tail group domains of different scattering length densities (SLDs).[90, 91] Estimates for the SLDs of the hydrated hydrophilic head group domain (9.40×10^{-6} Å^{-2}) and the aramid-containing hydrophobic domain (11.13×10^{-6} Å^{-2}) were calculated based on the molecular formulae and input into SasView software. The solvent SLD (water) is 9.44×10^{-6} Å^{-2}. The model was adjusted to the appropriate scale and background, and fit for thickness of the two domains. The following models were also attempted for fitting: lamellar, cylinder, flexible cylinder, core-shell cylinder*, parallelepiped, and core-shell parallelepiped*. Fits marked with an asterisk (*) allow for differing SLDs between the head and tail group domains. Despite a careful consideration of input parameters, each of these models, other than the lamellar model, fit to non-physical geometries based on Cryo-TEM images of the AA nanoribbons. In addition to the geometry of the amphiphilic nanostructures, the SAXS line shape can be affected by nanostructure aggregation, concentration, orientation/alignment, and dispersity, and instrument resolution. However, we still find this fitting useful as an

indication of nanostructure geometry, complementary to other characterization techniques. From this fitting, the hydrophobic core was found to be 2.8 ± 0.1 nm and the combined hydrophilic head group thickness was found to be 1.1 ± 0.4 nm, for a total bilayer thickness of 3.9 ± 0.5 nm. The higher error in the hydrophilic region is likely due to its similar SLD as the solvent. The lamellar fits shown in Figure 2.3 support that the nanoribbons adopt a rectangular cross-section as schematically illustrated in Figure 2.1, surrounded by a flexible, hydrated head group domain.

SAXS of all aramid amphiphile assemblies was also captured at 80 °C to probe the thermal stability of the nanostructure (Figure 2.6). Capillaries were heated from room temperature to 80 °C at 10 °C/min in a Linkam TMS600 heating stage and synchrotron SAXS profiles were captured at 0 min., 5 min., and 10 min. after reaching 80 °C. All profiles are background subtracted using a water-filled capillary which underwent the same heating. The lower signal-to-noise observed in SAXS of compounds **1** and **2**, compared to compound **3**, is due to their limited solubility.

WAXS and SAXS measurements on dried macroscopic AA threads were performed in vacuum on a SAXSLAB instrument using a Rigaku 002 microfocus X-ray source (CuKα radiation, 1.5418 Å) and a DECTRIS PILATUS 300 K detector. WAXS and SAXS profiles were measured at a sample-to-detector distance of 109 mm and 459 mm, respectively.

Cryogenic transmission electron microscopy

Cryo-TEM grids were prepared with an FEI Vitrobot Mark IV. Holey carbon grids (Ted Pella, 300 mesh, copper) were glow-discharged, before a 3.0 µl drop of a 2.0 mg/mL amphiphile solution was pipetted onto the grids in a chamber with 100% humidity. The grids were blotted for 4 s and then plunged into liquid C_2H_6 followed by transferring to liquid N_2. Images were captured in an FEI Tecnai Arctica microscope at an accelerating voltage of 200 kV. The defocus in data collection ranged from –1.5 to –3.5 µm.

Observation of nanoribbon length by atomic force microscopy

Compound **3** solution (2.0 wt%) was prepared for AFM by following the sonication and heat treatment for making nanoribbon thread solutions prior to their shear alignment:

bath sonication for 24 h, resting for 12 h, annealing in a heating block at 80 °C for 10 h and then slow cooling to room temperature. The solution was then diluted to 0.01 wt% and a 100 µl droplet of this diluted solution was deposited onto a cleaned mica substrate and analysed by AFM. The mica substrate was prepared through plane cleavage and cleaning with deionized H_2O. After 3 h of incubating the amphiphile solution on the clean mica, the solution was removed and then used directly for AFM imaging. Nanoribbons were imaged in tapping mode in air using a Cypher (Asylum Research, Oxford Instruments) atomic force microscope. We used AC160TS-R3 cantilevers from Olympus (nominal spring constant 26 N m^{-1} and resonance frequency of 300 kHz in air). AFM images were recorded at 512 pixels × 512 pixels at a scanning speed of 0.65 Hz.

Scanning electron microscopy

SEM images were recorded on a Zeiss MERLIN field emission microscope operating at a 1–3 kV accelerating voltage to resolve the higher-order structure of the dried AA nanoribbon threads. A secondary electron detector set to 120–200 pA was used for imaging. Samples were coated with 10 nm Au by sputtering on a MS Q150T ES coater.

Förster resonance energy transfer

A fluorescent donor (EDANS) and quencher (DABCYL) were each covalently tethered to the head group region of an AA (Figure 2.15). AAs were prepared at concentrations of 0.1 to 0.5 mM in water and co-assembled with 5 mol% donor- or quencher-tagged analogues. Fluorescence intensities were measured on a Varian Cary Eclipse spectrophotometer operating at an excitation wavelength of 334 nm with excitation and emission slits set at 5 nm. A fluorimeter scan rate of 600 nm/min was used, and the photomultiplier tube detector voltage was 600 V.

EDANS and DABCYL serve as a typical Förster resonance energy transfer (FRET) pair with a Förster radius of 3.3 nm.[101] When the donor and quencher approach the Förster radius, energy transfer from the donor to the quencher results in a reduction of fluorescence intensity through vibrational relaxation pathways. Therefore, decreases in fluorescence intensity correlate to molecular exchange between adjacent nanoribbons.

As a control, completely mixed co-assemblies of amphiphiles labeled with both a donor fluorophore and dark quencher show a 76% reduction in fluorescence intensity relative to assemblies labeled solely with the fluorophore (Figure 2.16).

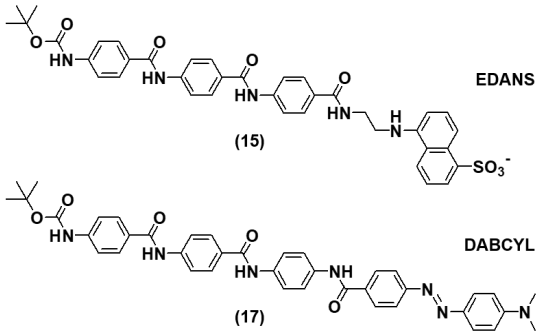

Figure 2.15 l EDANS and DABCYL-based aramid amphiphiles used in the FRET study.

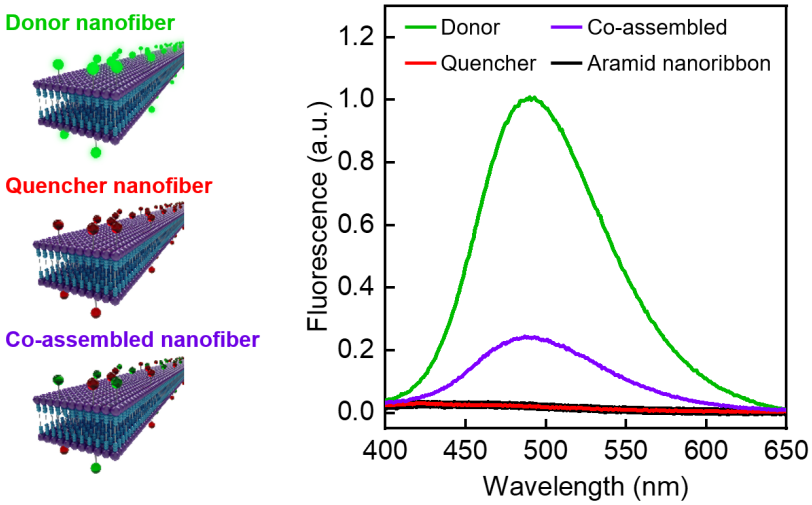

Figure 2.16 l The fluorescence intensity of nanoribbons labeled with the FRET donor EDANS is quenched by 76% when co-assembled with FRET quencher DABCYL.

Stiffness determination by topographical analysis of nanoribbon contours

Compound **3** nanoribbons were imaged in tapping mode in water using a Bruker/JPK Nanowizard 4 atomic force microscope using BL-AC40-TS cantilevers from Olympus

(nominal spring constant 0.1 N/m and resonance frequency of ~25 kHz in water). AFM images were recorded at 512 pixels × 512 pixels at a scanning speed of 10 Hz.

Compound **3** was chosen for analysis by atomic force microscopy (AFM) because of its high solubility and favorable surface interaction with AFM substrates. DI water was added to a lyophilized sample of **3** to reach 30 mg/mL. A sonicator bath was used to accelerate self-assembly. After 24 h at room temperature, the suspension was diluted to 0.03 mg/mL and deposited on a clean glass surface. The glass substrate was prepared through cleanings with DI H_2O and ethanol, drying with stream of N_2 (g), and activation by UV/ozone treatment. After 5 min of incubating the nanoribbon suspension on the clean glass, the surface was rinsed with DI water and used directly for AFM imaging.

AFM images (Figure 2.17) were used to determine the persistence length and Young's modulus of the ribbons. Fluctuations of ribbon shape are statistically processed using the Easyworm software tool,[105] which traces parametric splines to the contours of many ribbons of the same sample (in this experiment, n = 29 ribbons). Parametric splines store the $x - y$ coordinates of all the knots along the ribbons. Each combination of two knots gives a secant length L, and the midpoint of this secant deviates from the ribbon contour by a distance δ. The persistence length P is then obtained by least-square fitting the data to the worm-like chain model for semi-flexible polymers, $< \delta^2 > = L^3/(48 \times P)$, for ribbons equilibrating in 2-D. The persistence length reflects how much a ribbon bends as a result of thermal fluctuations. A higher persistence length of a ribbon corresponds to a lesser change in orientation over a given distance along its contour. The flexural rigidity F is the result of scaling the persistence length to the thermal energy according to $F = P \times k_B T$. Finally, the Young's (elastic) modulus E is obtained using $E = F/I$, where I is the area moment of inertia, which reflects the resistance to bending of a cross-section. For the circular cross-section observed in AFM measurements, the moment of inertia, $I = \pi \cdot d^4/64$, where d is the ribbon diameter. Heights of each nanoribbon were estimated by analysis of nanoribbon cross-sections observed in the AFM images. The AFM height measurements are consistent with cryo-TEM and SAXS measurements, and therefore we use $d = 3.7 \pm 0.5$ nm to calculate I.

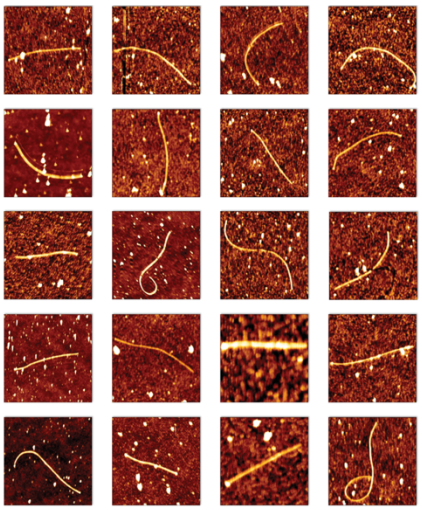

Figure 2.17 I Contour traces of AFM images of AA nanoribbons, a representative set of which are shown here, were used for determining nanoribbon stiffness by statistical topographical analysis. Image dimensions are 1 μm x 1 μm.

Yield strength determination by sonication-induced scission

A Qsonica Q500 sonicator with a 2-mm-diameter microtip was used to sonicate 10 mL of a 0.5 mg/mL aqueous solution of compound **3** nanoribbons. A vibrational frequency of 20 kHz and amplitude of 25% were used during the experiment, which lasted for 2 h of 'sonication on' time with a 5-seconds-on/3-seconds-off pulse. Sonicating power was held at 30 W/cm^2 to ensure cavitation. The solution was held in an ice bath for the duration of the experiment to prevent solvent evaporation and tip breakage during sonication. Images of fragments after sonication were captured by TEM and AFM.

We measure the yield (tensile) strength σ* by using a sonication-induced fibril scission technique, as detailed in our previous work.[106] In short, sonication creates collapsing cavitation bubbles, causing fluid velocity fields to trap fibrils and exert shear forces on them. This leads to fibril extension in opposite directions and mechanically-induced rupture at the site of highest stress. The model developed by Huang et al. implies that the forces exerted on the fibril decrease dramatically with the fibril length.[106] Hence there is a threshold length L_{lim} below which a fibril of a given cross-section will not break anymore. We plot the length of hundreds of fibril fragments as a function of their cross-sectional size (Figure 2.17), and derive σ from the relationship:[106]

$$L_{\mathrm{lim}} = \alpha C \sqrt{\sigma} \qquad (1)$$

where $\alpha = 7.10^{-4}$ is a prefactor that depends on the experimental conditions, and C reflects the cross-sectional size of the fibril fragments. For a rectangular cross-section fibril with long edge w (i.e. TEM width), and short edge h (i.e. AFM height), it is given by:[110]

$$C = \left[\frac{\gamma}{2w^2}\left[\left(\ln\left(\gamma + \sqrt{\gamma^2 + 1}\right) + \ln\left(\gamma^{-1} + \sqrt{\gamma^{-2} + 1}\right)\right]\right]^{-1/2} \qquad (2)$$

where $\gamma = w/h$ is the aspect ratio. After prolonged sonication time, fibril length distribution reaches a plateau and the size of fragments that belong to a sample fall in a "terminal range" defined by $\left[{}^{L_{lim}}/_{2}, L_{\mathrm{lim}}\right]$. However, we expect an even broader distribution of fragment lengths L, because both the cross-sectional area and intrinsic strength can vary. This broadening of the terminal range is considered by determining the lines of best fit from the extremities of the distribution.[110] We represent the extremities by the 5–10 data points corresponding to the smallest and longest aspect ratios L/C (see the black dots in Figure 2.18), discarding obvious outliers. The lowest slope s reflects the low boundary of the shortest terminal range (i.e. the smallest aspect ratio), and the highest slope S exposes the high boundary of the longest terminal range (*i.e.* the longest aspect ratio). The shortest and longest terminal ranges are thus defined by intervals $[s, 2s]$ and $[S/2, S]$, respectively. L_{lim} is the averaged top of any terminal range given by:

$$\frac{L_{\mathrm{lim}}}{C} = \frac{2s + S}{2} \pm \frac{2s - S}{2} \qquad (3)$$

Combining the results of Eq. 2 with Eq. 1 we obtain the tensile strength σ. This method is particularly solid to reveal at least the position of the lower edge of the terminal distribution, which corresponds to the lowest possible strength of the fibril sample. Using the absolute error ± (2*s* – *S*)/2 provides a simple way to account both for any experimental source of error and for the strength variability within a given sample. In this study all fibril fragments have a similar cross-sectional area, with w = 6.0 ± 1.3 nm and h = 3.1 ± 0.5 nm. Consequently, most fragment lengths are distributed in one single terminal range

$\left[\frac{L_{\mathrm{lim}}}{2}, L_{\mathrm{lim}}\right]$, as displayed in the histogram of the fragment length distribution (see Figure 2.17). In order not to overestimate the strength, we use a cut-off value to discard all fibril fragments with L > 134 nm. These fragments most likely escaped sonication-induced breakage because the initial fibril concentration was relatively high (~0.5 mg/mL); as a result, their lengths did not end up into the terminal range. To calculate the cut-off, we assume the most prominent peak of the distribution to correspond to $L_{\mathrm{lim}}/2$ and fit a Gaussian to that peak, which gives $L_{\mathrm{lim}}/2$ = 55 ± 12 nm for TEM. We then estimate L_{lim} = 110 ± 24 for TEM and use it to derive the cut-off.

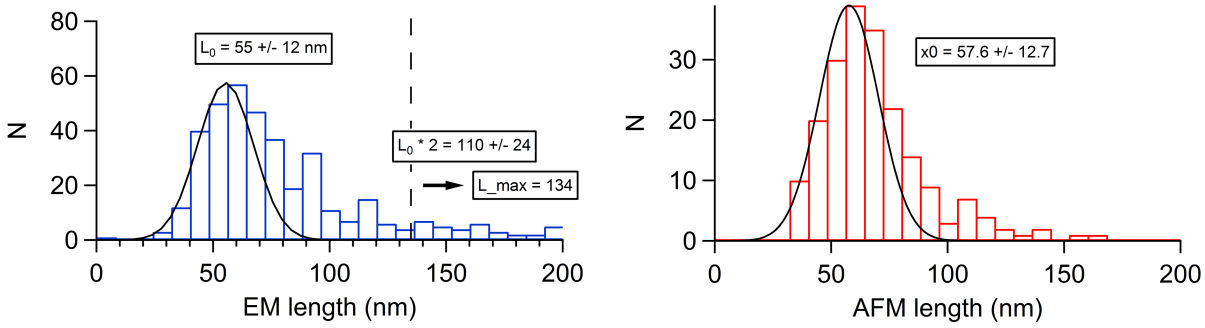

Figure 2.17 I The distribution of fragment lengths after sonication-induced scission of nanoribbons of **3** as measured by **a**, TEM and **b**, AFM.

Here the fragment lengths were independently estimated in both TEM and AFM measurements. Both techniques give similar results, also translating in similar strength values. For the determination of the cross-sectional parameter C, we used the AFM-determined mean height of the fibril fragments $h = 1.96 \pm 0.55$ nm in the analysis of the TEM data (Figure 2.18a), and we used the TEM-determined mean width of the fibril fragments $w = 6.0 \pm 1.3$ nm in the analysis of the AFM data (Figure 2.18b). Note that the mean AFM height of the fibril fragments is lower than that of non-sonicated fibrils, possibly because non-sonicated fibrils are higher-order assemblies and sonication leads to partial disassembly of the several protofilaments that form a “mature” fibril. The highest and lowest lines in this plot identify L_{lim} and the smallest fragments produced by sonication,

respectively, and the yellow region considers a broadening of these bounds due to variations in cross-sectional area and intrinsic strength.

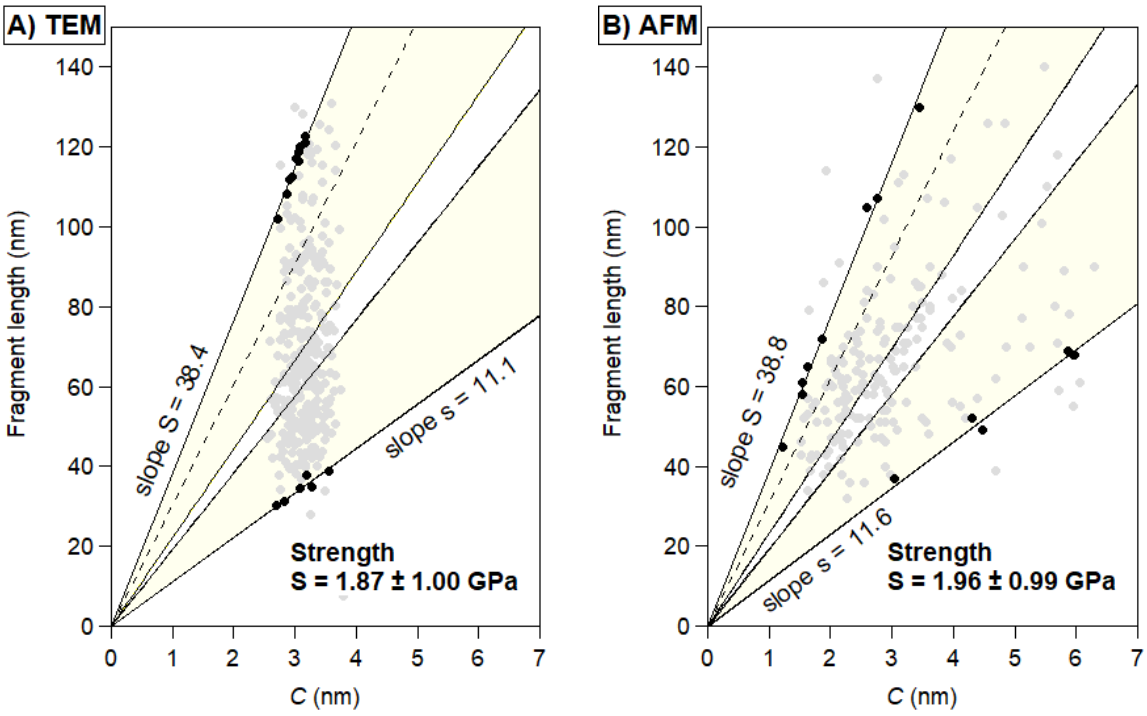

Figure 2.18 l Yield strength analysis of nanoribbons of **3** from sonication-induced scission identifies strengths of **a**, 1.87 ± 1.00 GPa based on TEM and **b**, 1.96 ± 0.99 GPa based on AFM analysis of the nanoribbon fragments, showing a close convergence between the two techniques.

Polarized light microscopy

The liquid crystalline state of gelled AA nanoribbons was observed using an Olympus BH-2 microscope equipped for polarized light imaging. Gelled nanoribbons were analysed immediately after extrusion onto a cleaned glass microscope slide while still wet. Images were captured with a Pixelink PL-E535CU camera.

Tensile testing of macroscopic AA threads

Macroscopic mechanical properties of compound **3** AA threads were characterized using a uniaxial bench-top tester (CellScale UStretch) equipped with a 0.5 N load cell. Threads were prepared following the shear alignment procedure described previously,

then fixed with epoxy glue on two tailored cardboard supports gripped to the standard spring-loaded clamps of the testing machine. The glue was allowed to set for 24 h. Threads with counterions of either sulfate (n = 6) or methanedisulfonate (n = 6) were tested at a constant stretch velocity of 25 µm/s. Each thread was imaged with an optical microscope to determine its mean diameter from multiple cross-sections, which varied between 55 µm and 80 µm for all threads.

Raw data from the UStretch software was exported and analysed separetly in MATLAB. Force measurements were converted to stress using the initial cross-sectional area. Displacement of the moving end (u_L) was converted into engineering strain using the initial length of each thread (L_0) as u_L/L_0. The Young's modulus was extracted by fitting each experiment to a linear elastic constitutive equation using a nonlinear least-squares algorithm. The extensibility (maximum strain at failure) was extracted directly from the stress–strain curves at the maximum stress before breakage. Values are reported as average ± one standard deviation.

Chapter 3

Morphological transitions of a photoswitchable aramid amphiphile nanostructure

This chapter was adapted from the publication "Morphological transitions of a photoswitchable aramid amphiphile nanostructure," originally published in Nano Letters.[119]

Abstract: Self-assembly of small amphiphilic molecules in water can lead to nanostructures of varying geometries with pristine internal molecular organization. Here we introduce a photoswitchable aramid amphiphile (AA), designed to exhibit extensive hydrogen bonding and robust mechanical properties upon self-assembly, while containing a vinylnitrile group for photoinduced cis–trans isomerization. We demonstrate spontaneous self-assembly of the vinylnitrile-containing AA in water to form nanoribbons. Upon UV irradiation, trans-to-cis isomerizations occur concomitantly with a morphological transition from nanoribbons to nanotubes. The nanotube structure persists in water for over six months, stabilized by strong and collective intermolecular interactions. We demonstrate that the nanoribbon-to-nanotube transition is reversible upon heating and that switching between states can be achieved repeatedly. Finally, we use electron microscopy to capture the transition and propose mechanisms for nanoribbon-to-nanotube rearrangement and vice versa. The stability and switchability of photoresponsive AA nanostructures make them viable for a range of future applications.

Introduction

Molecular self-assembly of amphiphilic small molecules in water provides a route to nanostructures with high surface areas and versatile surface chemistries.[25, 68, 120] The dimensions of self-assembled nanostructures are determined by the lengths of their constituent molecules; in turn, amphiphilic molecules assemble to form nanostructures with dimensions on the order of 10 nm along at least one axis, and high surface areas.[19, 52, 121] Further, these architectures readily allow for the inclusion of functional molecules by co-assembly, facilitating reactions or recognition events at their surfaces.[122-124] Amphiphilic self-assembly is governed by noncovalent interactions and therefore leads to dynamic and path-dependent morphologies.[48, 125, 126] Such materials have shown great promise as biomaterials, where fast conformational dynamics are an important feature,[24, 53, 127, 128] and also in the area of *systems chemistry*, which exploits collective behaviors of ensembles of molecules governed by their dynamic nature.[31]

Imparting photoswitching capabilities within self-assembled small molecule nanostructures is an im-portant target for introducing new functions. Phototriggers have been combined with amphiphilic self-assembly for a variety of purposes: to liberate surface-bound cell signaling moieties from bioactive nanofiber matrices,[129] to modulate bilayer membrane fluidity,[130] to disrupt the balance of *cis-trans* equilibria by selectively arresting one isomer into an assembled structure,[131] to modulate mechanical properties for photolithography and adhesion/lubrication applications,[132] and for photoinitiated synthesis of amphiphiles in water.[133] However, photoisomerization in these systems has generally so far only led to relatively short-lived metastable states, with half-lives ranging from seconds to days.[134] We hypothesize that achieving a morphological transition whose reverse reaction also requires input energy may be accomplished by tuning the intermolecular interac-tion strengths within the metastable nanostructure.

Though less frequently used, the isomerized products of stilbene-derived chromophores are more stable in contrast to those from conventional azobenzene dyes and can be used to enhance the half-life of a metastable nanostructure.[135-138] Vinylnitrile-based groups – a class of stilbene-derived chromophores – incorporated in a molecular

structure can be isomerized by irradiation from the *trans* to *cis* state, and spontaneously reverts slowly (on the order of minutes to days) at room temperature.[134, 139, 140] Thus, programming the design of photoresponsive small molecules can allow us to tune molecular self-assembled nanoarchitectures with desirable dimensions and time-stable morphologies.

Here, we investigate the phototriggered isomerization reaction of amphiphiles after self-assembly into strongly cohesive nanoribbons in water. The chemical structure of the small molecule constituents is designed to exhibit (1) strong and extensive intermolecular interactions and (2) a photoactive moiety known for a dramatic geometric transition upon a 365 nm UV (UVA) light irradiation. This approach is hypothesized to induce molecular isomerization for reversible morphological transitions, with structural stability in both the *trans* and *cis* morphological states.

A strong and extensive network of intermolecular interactions within the nanostructure is achieved by employing aramid amphiphile (AA) molecules. AAs have previously been show to assemble spontaneously in water to form nanoribbons with thicknesses and widths under 10 nanometers, and lengths greater than tens of microns.[51] Within AA nanoribbons, each molecule is fixed in place by six in-register hydrogen bonds propagating down the length of the nanoribbon, and π-π stacking across its width. This network of strong interactions suppresses molecular exchange and migration within assemblies and produces nanoribbons with robust mechanical properties, rivaling silk.[51]

Results and Discussion

AAs are composed of a hydrophilic head group, an aramid structural domain, and a hydrophobic tail (Figure 3.1a). Here, we design a photoswitchable analogue to the conventional AA molecule which incorporates a vinylnitrile group into the center of the aramid structural domain (Figure 3.1b). This molecule is designed to similarly form nanoribbons in water but further exhibit a morphological transition upon UVA irradiation. The effect of isomerization of adjacent vinylnitrile groups and the strong intermolecular

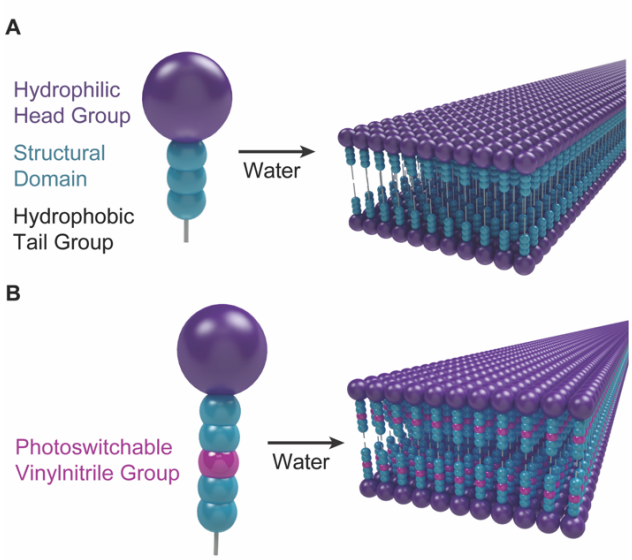

Figure 3.1 I Aramid amphiphiles (AAs) self-assemble in water to form nanoribbons. Their stabilities are bolstered by strong intermolecular hydrogen bonding between adjacent aramid structural domains. **a**, Conventional AAs self-assemble in water to form planar nanoribbons with no stimuli-responsive behavior. **b**, Photoresponsive AAs, designed analogously to conventional AAs but with a vinylnitrile moiety in the center of the aramid domain, are designed to assemble into nanoribbons in water with triggerable morphological transitions.

interactions within the nanostructure are hypothesized to dramatically increase the lifetime of the isomerized product. Compound **1** (Figure 3.2a) is selected as a control for this experiment for its similar chemical structure and equivalent number of hydrogen bonds as compound **2** (Figure 3.2d).

Compound **1** is a conventional AA whose significant internal cohesion results in nanoribbons with suppressed exchange dynamics.[48, 51] In water, **1** spontaneously self-assembles into high-aspect-ratio nanoribbons (Figure 3.2b). Small angle X-ray scattering (SAXS) at a 30 mg/mL concentration and its fitting (Figure 3.2c) is used to extract that nanoribbons of **1** exhibit 3.9 nm by 5.8 nm cross-sections.[91]

Compound **2** is obtained following similar reactions as previously reported. In short, the molecule is built up with alternating carbodiimide-mediated amidation coupling reactions and standard deprotection reactions, and uses the Knoevenagel reaction to obtain the target compound. Detailed synthetic methods are described in the Methods section. The chemical structures and purities are confirmed by ^{1}H and ^{13}C nuclear

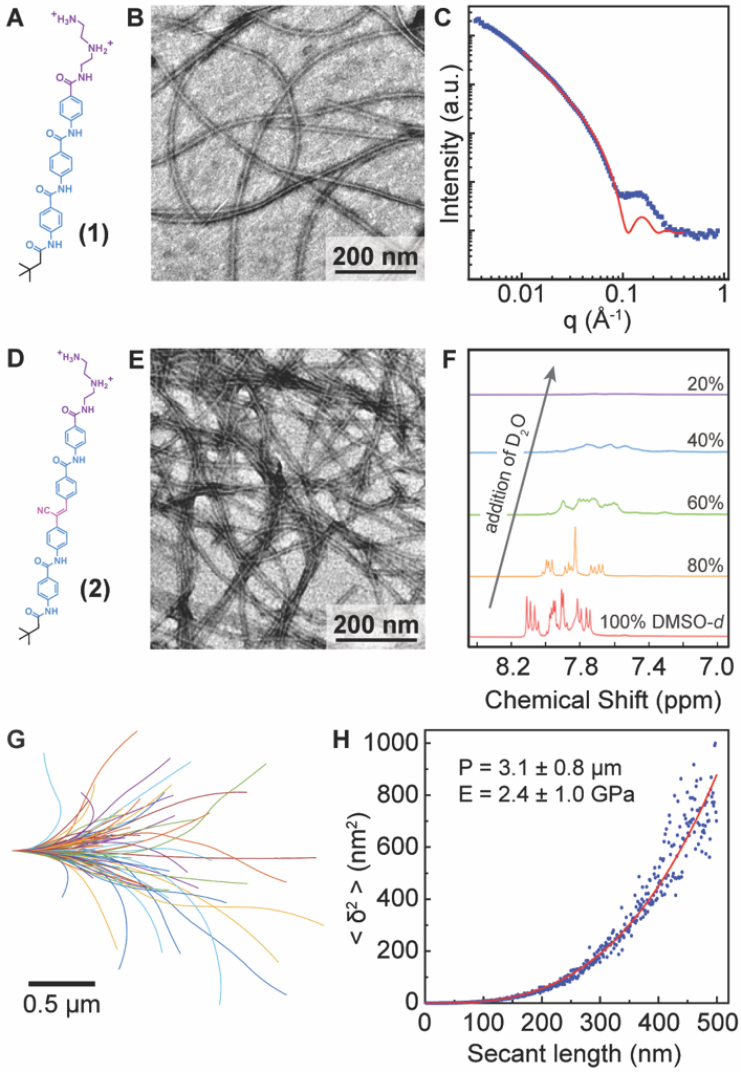

Figure 3.2 I Both conventional and photoswitchable AAs form nanoribbons in water. **a - b**, Compound **1** is a conventional AA with a cationic head group (purple), aramid structural domain (blue), and short aliphatic tail (black) that spontaneosuly forms nanoribbons with 5.8 nm widths upon assembly in water. **c**, Compound **1** nanoribbons are determined to have 3.9 nm thicknesses based on lamellar fitting (red line) to SAXS. **d**, Compound **2** incorporates a photoswitchable vinylnitrile moiety (pink) into the aramid amphiphile design. **e**, Compound **2** forms nanoribbons mimicking those of compound **1** upon spontaneous assembly in water. **f**, The assembly of compound **2** is observed by ^{1}H NMR of the aromatic molecular region as the ratio of D_2O to DMSO-*d* increases. Assembly of the amphiphiles in D_2O results in an upfield proton shift from magnetic shielding and peak broadening from slowing conformational dynamics. **g**, Contours of compound **2** nanoribbons (n = 96) are traced from AFM profiles for statistical topographical analysis. **h**, Midpoint deviations (δ) from the contour traces of compound **2** nanoribbons are used to derive a Young's modulus of E = 2.4 ± 1.0 GPa from calculating a persistence length, P = 3.1 ± 0.8 µm, by least-squares fitting of a worm-like chain model for semi-flexible polymers (red line) to the data. This stiffness value closely matches that of conventional AAs.[51]

magnetic resonance (NMR), matrix assisted laser desorption and ionization time-of-flight (MALDI-ToF) mass spectrometry, and elemental analysis.

We first seek to understand the self-assembly behavior of compound **2** in water. As previously observed for compound **1**, compound **2** spontaneously forms high-aspect-ratio nanoribbons with lengths on the order of microns upon assembly in water (Figure 3.2e). Hydrogen bonding between amides in the aramid structural domain is likely the main driving force in forming the elongated nanoribbon structure. π-π stacking assists in holding the hydrogen bonding sheets laterally, and the local dipole moments of the cyanide can further help to induce side-to-side intermolecular coupling.

Molecular interaction resulting from the self-assembly of **2** in water can be investigated via solvent variation (Figure 3.2f). Compound **2** is highly soluble in deuterated dimethylsulfoxide (DMSO-*d*), resulting in a monomeric state. This is observed in the ^{1}H NMR spectra of **2** by well-resolved, sharp peaks, shown for aromatic rings in the structural domain. These proton peaks widen and shift upfield when deuterated water (D_2O) is titrated into the solution. The gradual broadening of these peaks is concomitant with the formation of strong intermolecular interactions and the slowing of conformational dynamics upon self-assembly of **2** in water. The upfield shift of protons results from the tightening of intermolecular distances with assembly that induces a magnetic shielding effect. No nanoribbons or other nanostructures are observed by TEM when **1** or **2** are dissolved in 100% DMSO-*d*.

Compound **1** nanoribbons were previously shown to exhibit a Young's moduli of E = 1.7 ± 0.7 GPa.[51] Here, we employ a statistical topographical analysis of nanoribbon contours to determine if incorporating the photoswitchable vinylnitrile moiety impacts the nanoribbons' mechanical properties. This technique overcomes the lower size bound limitations of direct mechanical measurements, enabling stiffness measurements on nanofilaments with diameters below 10 nm.[104, 107] The contours of n = 96 compound **2** nanoribbons in water were captured by atomic force microscopy (Figure 3.2g). Parametric splines were extracted from each contour and used to obtain a nanoribbon persistence length of P = 3.1 ± 0.8 μm, from which a Young's modulus of E = 2.4 ± 1.0 GPa is calculated (Figure 3.2h).[104, 105] This stiffness closely matches the previously reported

stiffness for compound **1** nanoribbons,[51] likely resulting from similar intermolecular interaction strengths and hydrogen bond densities between the amphiphiles.

Molecular scale isomerizations of photoresponsive aromatic molecules result in changes in absorbance that can be detected by UV-Vis absorption spectroscopy. As expected, we observe no change in absorbance of aqueous solutions of **1** upon 1 h of irradiation with UVA light (0.1 mg/mL, 1500 mW/cm^2, Figure 3.3). In contrast, a 0.1 mg/mL solution of compound **2** dissolved in DMSO shows a dramatic reduction in peak intensity at λ_{max} = 350 nm under the same conditions (Figure 3.4). This spectral change indicates that the vinylnitrile *cis* isomer is increased during irradiation with a corresponding decrease in the amount of *trans* isomer (isomer nomenclature discussion in Methods).

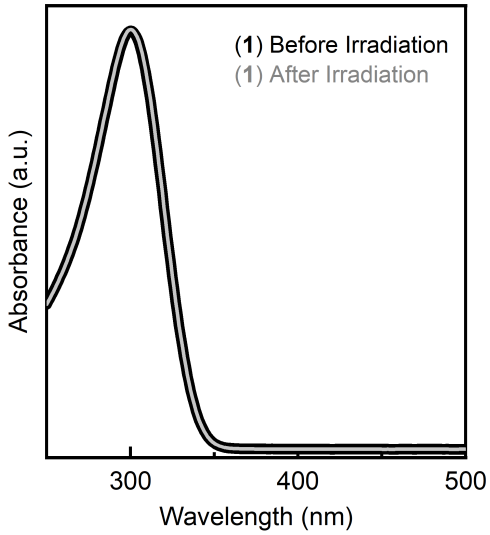

Figure 3.3 | A suspension of compound **1** nanoribbons shows no change in UV-Vis absorbance after irradiation for 1 h with UVA light.

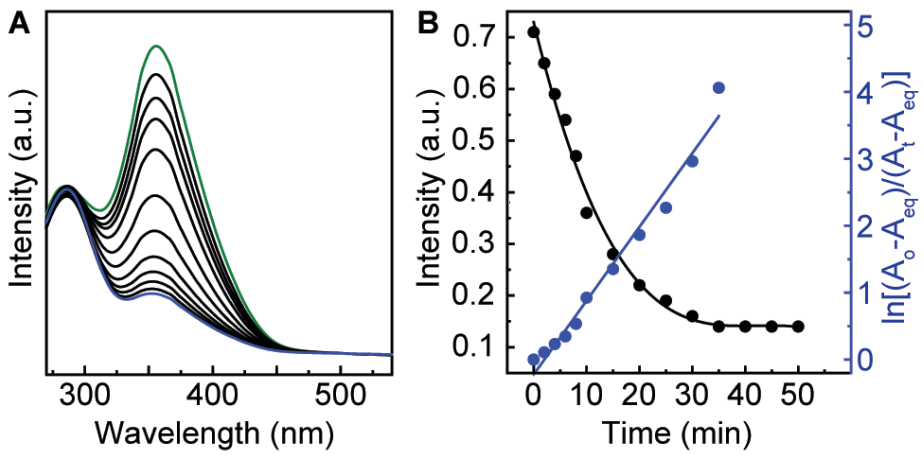

Figure 3.4 | a, UV-Vis spectra of compound **2** dissolved in DMSO with over 50 min of irradiation with UVA light irradiation. The initial state is the green line, and the final state is the blue line. **b**, Time-dependent absorbance changes are used to calculate a photoisomerization rate constant of $K = 1.10 \times 10^{-1}$/min of compound **2** in DMSO.

Compound **2** assembled in water (0.1 mg/mL) also shows a spectral change after 1 h of irradiation with UVA light similar to that observed in DMSO (Figure 3.5a). The photochemical reaction rate of **2** in water ($K = 5.44 \times 10^{-2}$/min, Figure 3.5b) is slightly suppressed compared to its rate in DMSO ($K = 1.10 \times 10^{-1}$/min). In addition, the reduction in peak absorbance intensity corresponding to the photoisomerization is decreased from 80% in DMSO to 67% in water. Changes in the state of soft matter driven by photochemical reactions are sensitive to their local environments, including polarity, viscosity, and light polarization, as well as the strength of intermolecular interactions when photochromic molecules are dissolved or dispersed in solvent.[141] Thus, we infer that the significant change in the molecules' local environments afforded by self-assembly impacts their measured photoisomerization kinetics.

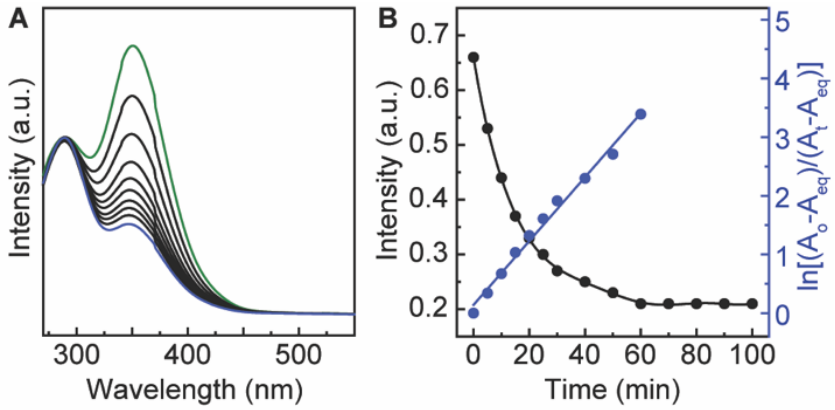

Figure 3.5 l Nanoribbons from compound **2** in water show triggerable isomerization upon UVA irradiation. **a**, Compound **2** exhibits a 67% drop in peak absorbance after 1 h min of irradiation. The initial state is shown in green, and the photostationary state is shown in blue. **b**, Time-dependent absorbance changes upon UVA irradiation of compound **2** is used to create a first-order plot of the *trans* to *cis* isomerization and extract a photoisomerization rate constant of $K = 5.44 \times 10^{-2}$/min.

We verify that nanostructures persist in water after photoisomerization by observing the Tyndall effect in solution. Compound **2** dissolved in DMSO before and after UVA exposure does not exhibit Tyndall scattering (i.e. light scattering upon red laser illumination indicative of the presence of nanostructures), and correspondingly no nanostructures are observed by AFM (Figure 3.6). Conversely, **2** in water displays significant Tyndall scattering before and after UVA irradiation, indicating the maintenance of nanostructures throughout the photoisomerization (Figure 3.6).[142] AFM verifies the presence of nanoribbons before UVA irradiation, and suggests a different nanotube structure afterwards. We further demonstrate that the morphological transition of compound **2** in water is facilitated when the intensity of UVA light is increased (Figure 3.7).

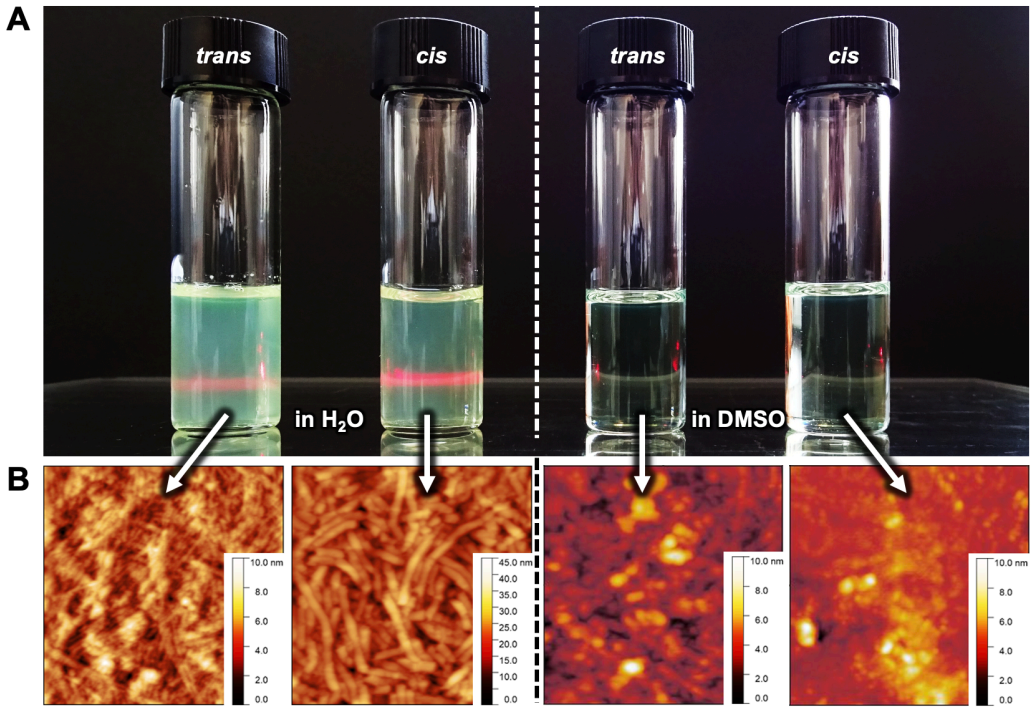

Figure 3.6 | a, Observation of the Tyndall effect of 7 mg/mL solutions of compound **2** in water (left two vials) or DMSO (right two vials) in its *trans* or *cis* state. The scattering observed by compound **2** in water is indicative of the maintenance of a nanostructure; its absence in DMSO indicates that compound **2** does not form an ordered nanostructure. **b**, AFM micrographs of the solutions from each vial indicate show, from left to right, nanoribbons from the assembly of compound **2** in water in its *trans* state; nanotubes following the irradiation of compound **2** in water into a *cis*-rich state; and no ordered nanostructure when compound **2** is dissolved in DMSO in either its *trans* or *cis* states.

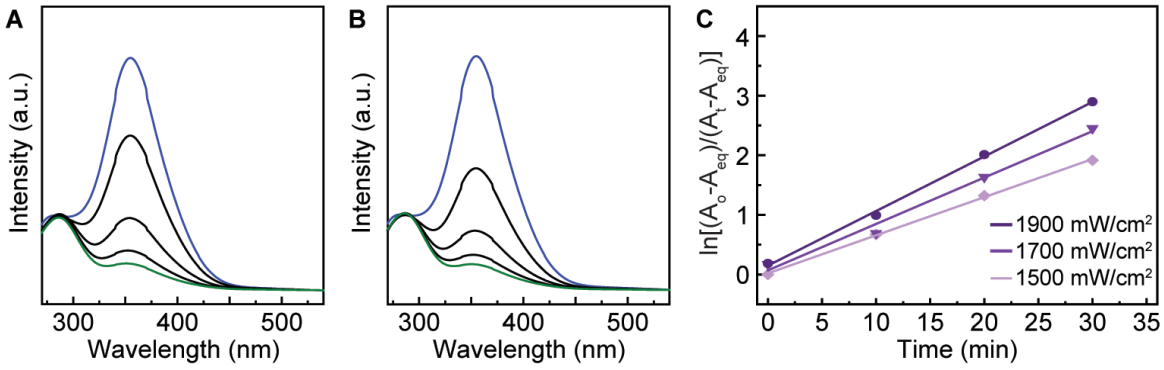

Figure 3.7 | a, Time-dependent UV-Vis spectra of compound **2** under medium intensity UVA light (1700 mW/cm^2; initial line in blue, final line in green). **b**, Time-dependent UV-Vis spectra of compound **2** under high intensity UVA light (1900 mW/cm^2; initial line in blue, final line in green). **c**, From a first-order plot of the *trans* to *cis* isomerization of compound **2** at each irradiation power level, we extract photoisomerization rate constants of 5.44 × 10^{-2}/min, 7.77 × 10^{-2}/min, and 9.15 × 10^{-2}/min for irradiation powers of 1500 mW/cm^2, 1700 mW/cm^2, and 1900 mW/cm^2, respectively.

With this information, we seek to understand the morphology of the *cis* rich compound **2** assembly. We observe that compound **2** nanoribbons convert into nanotubes as the vinylnitrile moiety undergoes a *trans*-to-*cis* isomerization. Initially, compound **2** nanoribbons mimic the structure of **1** nanoribbons, as shown by TEM and SAXS (Figures 3.2e and 3.8a). The SAXS profile of an aqueous solution of **2** was best fit to a rectangular prism model, returning nanoribbon dimensions of 4.7 nm in thickness and 5.4 nm in width.[143] Upon UVA irradiation of an aqueous solution of **2** nanoribbons for 1 h, the nanoribbons converted into nanotubes with a shell thickness comparable to the nanoribbon thickness (Figure 3.8b). The SAXS profile of the aqueous nanotube solution was fit to a hollow cylinder model with a 19.4 nm core diameter and a 6.1 nm shell thickness (Figure 3.8c).[144]

The structural transition demonstrated in Figures 3.8a-c led us to investigate the mechanism of nanoribbon-to-nanotube morphological conversion in order to further understand the switching phenomena. We irradiated nanoribbons of **2** for just 10 min, rather than the typical irradiation time corresponding to the *PSS*, to capture its intermediate state. TEM of the solution at this time point shows an intermediate coiled ribbon nanostructure (Figure 3.8d). By comparing the dimensions of the nanoribbon coils to those of the nanotube itself, we can conclude that the photochemical reaction of amphiphiles within the nanoribbon assembly results in twisting of the nanoribbons to form tight coils, which then fuse to yield nanotubes. For context, folding of supramolecular nanoribbons into helical shapes without fusing,[145, 146] toroid stacking to form tubular or helical structures,[147] and light-induced tubular disassembly[148] have been previously reported, but the mechanism shown here in the case of aramid amphiphiles has not previously been demonstrated as a response to photoisomerization in supramolecular assemblies. Similar mechanisms have been observed for chiral amphiphiles, bent core liquid crystals, and discotic polyaromatic hydrocarbons.[149-151]

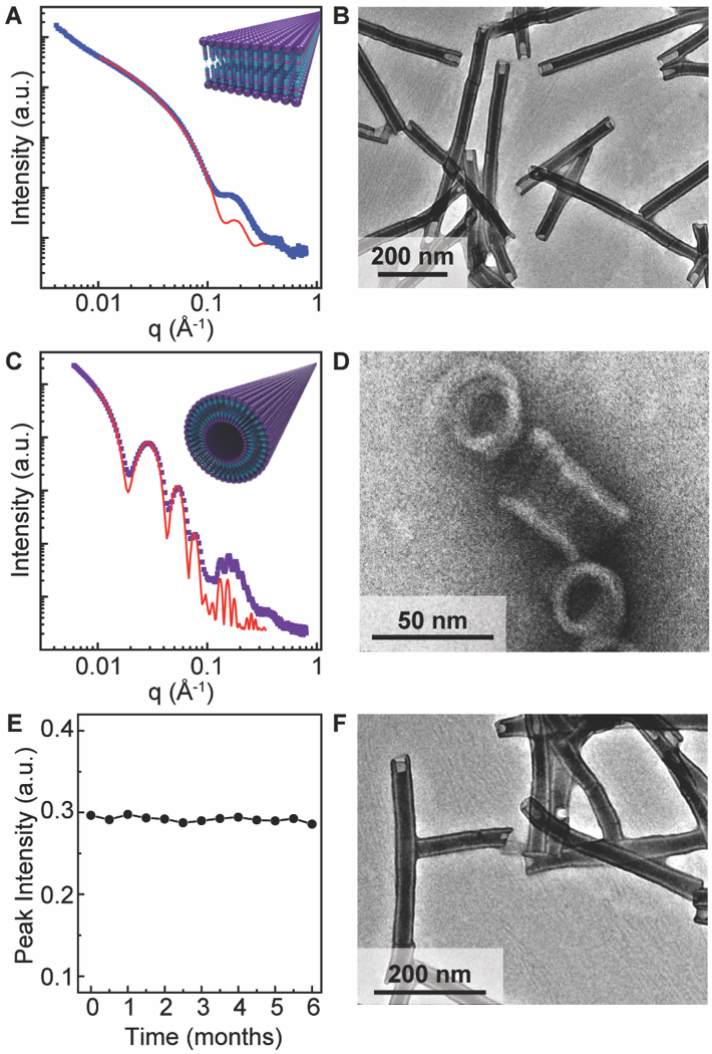

Figure 3.8 l Compound **2** nanoribbons triggerably transition into nanotubes upon UVA irradiation and maintain their isomerized structure for at least six months. **a**, Fitting of a rectangular prism model to SAXS of compound **2** nanoribbons is used to extract a 4.7 nm x 5.4 nm cross-section. **b**, After 1 h of UVA irradiation, compound **2** nanoribbons convert into nanotubes observable by TEM. **c**, Fitting of a hollow cylinder model to SAXS of compound **2** nanotubes reveals a 6.1 nm shell thickness and 19.4 nm core diameter. **d**, Planar **2** nanoribbons coil under UVA light to form tight spirals in the nanoribbon to nanotube transition. The edges of the spirals fuse to form the observed final nanotube structure. **e**, UV-Vis absorption spectroscopy shows the maintenance of the same peak absorbance intensity corresponding to the *cis* state for six months, measured in half-month intervals. **f**, Representative TEM of compound **2** nanotubes six months after UVA irradiation shows no evidence of nanoribbon formation.

Formation of lamellar nanoribbons by the *trans* state of **2** is driven by dense intermolecular interactions between amphiphilic molecules. **2** nanoribbons are constructed from layers of molecules aligned normal to the nanoribbon length axis. In the *trans* state, the molecules have a rod-like geometry, providing a feasible path for the formation of a nanoribbon morphology. Upon UVA irradiation of conversion of **2** to the *cis* state, the molecules take on a bent-shape geometry and flexible conformation, resulting in local reorganization to compensate for space requirements. Diffraction on the sub-nanometer length scale provides local molecular packing information, so we perform 1D wide-angle X-ray diffraction (WAXD) on lyophilized samples of compound **2** nanostructures to elucidate this effect.[152] Weakening and broadening of sharp reflection peaks after UVA irradiation indicates that long-range molecular and short-range positional orders are partially disrupted compared to the *trans* state (Figure 3.9). To maintain favorable interactions, we infer that the hydrophilic cationic head groups orient toward their aqueous environment, inducing curvature to the assembly.[153] Torsion induced by this curvature leads to the nanoribbon twisting, which ultimately fuse at the energetically unfavorable hydrophobic edges to produce nanotubes.[154]

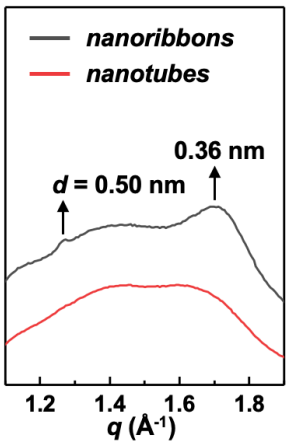

Figure 3.9. 1D WAXD pattern of lyophilized compound **2** nanoribbons and nanotubes. The geometries of these nanostructures are observed to retain their shape when dried by AFM.

Reaching the *PSS* of **2** is similar to typical light-driven responses, but in contrast to that of previously reported materials, the isomerized product of **2** remains unchanged for several months after turning off UVA light (Figures 3.8e-f). The strongly-interacting nature of **2** molecules in an assembled state, aided by hydrogen bonding and π-π stacking in the aramid structural domain, drastically enhances their activation barrier for *cis*-to-*trans* isomerization, thereby increasing the nanotube lifetime. Consequently, we observe no nanotube-to-nanoribbon reversal at time points up to six months by UV-Vis spectroscopy and TEM.

Finally, we investigated whether the isomerization reaction and consequent morphological transition is reversible by providing sufficient thermal energy for the vinylnitrile to revert to its *trans* ground state. Unable to overcome the activation barrier for reversibility at room temperature, we hypothesized adding thermal energy could induce the reverse reaction as it increases the conformational dynamics within the nanostructure, facilitating the one-bond-flip isomerization reaction from *cis*-to-*trans*.[155, 156] Upon heating a solution of compound **2** nanoribbons to 80 °C for 1 h and cooling slowly, we observe a recovery in UV-Vis absorbance to its original peak value. This heating and irradiation process can be repeated at least five times, indicating that the isomerization transition can be repeatedly performed on the nanostructures without loss (Figure 3.10a, Figure3.11). The nanotube heating process fully regenerates the nanoribbons with the same dimensions as their original assembled state (Figures 3.10b-c).

We again sought to capture the intermediate state of the morphological transition occurrng with the reverse isomerization. The vinylnitrile *cis*-to-*trans* isomerization induces strain that causes rupture of the nanotube (Figure 3.10d). This rupture propagates across the nanotube to sciss the nanostructure (Figure 3.10e) and enables nanoribbon formation by unraveling of the nanotube at the interfaces (Figure 3.10f).

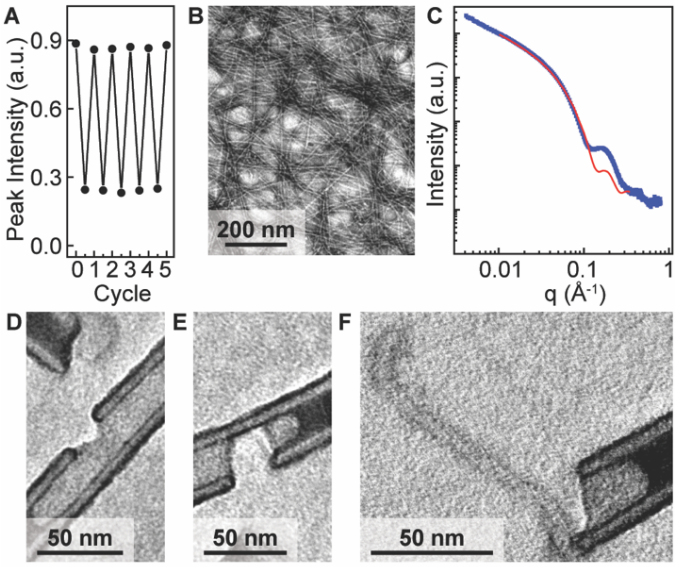

Figure 3.10 l The photoisomerization of compound **2** to nanotubes is reversible to nanoribbons by heating at 80°C for 1 h. **a**, **2** isomerization is cyclically modulated over five cycles from repeated UVA irradiation and heating, as captured by tracking the peak absorbance intensity by UV-Vis spectroscopy. **b,** Representative TEM of compound **2** nanoribbons after 1 h of heating compound **2** nanotubes at 80 °C. **c**, SAXS of compound **1** nanoribbons after heating from the nanotube morphology shows a return to its original dimensions, based on a rectangular prism fit (red). **d-f**, Upon heating, compound **2** nanotubes rupture under torsional strain from isomerization, releasing nanoribbons that resemble the initial assemblies.

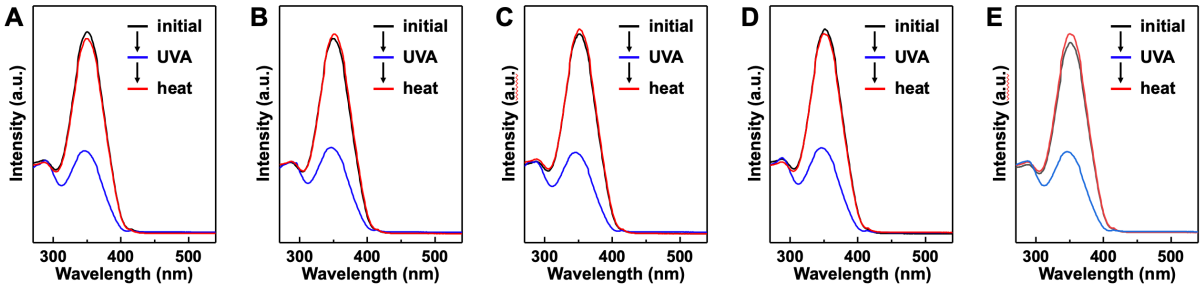

Figure 3.11 | UV-Vis spectra of compound **2** in water initially, after UVA irradiation, and after annealing over five cycles: **a**, cycle one, **b**, cycle two, **c**, cycle three, **d**, cycle four, and **e**, cycle five. The recovery of the absorbance to its initial state after annealing suggests that little to no photobleaching occurs during this process.

Here, we presented a molecular self-assembly platform: photoresponsive aramid amphiphile (AA) nanostructures. We demonstrate that the *trans*-to-*cis* photoisomerization of constituent molecules triggers a morphological transition from nanoribbons to nanotubes. The nanotube state exhibits an extraordinarily long lifetime, especially for vinylnitrile moieties, of at least six months, achieved by employing the AA motif; a structure that exploits extraordinarily strong and extensive intermolecular interactions. We further demonstrated reversibility of the morphological transition by providing sufficient thermal energy to induce the *cis*-to-*trans* conversion and recover the initial nanoribbon morphology. We captured the intermediate states of both morphological transitions to reveal their mechanisms: nanoribbon coiling and edge-to-edge fusion to form nanotubes, and nanotube fracture to release nanoribbons from the interfaces. This self-assembly platform could meet pressing challenges in responsive nanomaterials design by combining exceptional nanostructure stability and long excited state lifetimes with the capability to undergo photo-triggered morphological transitions.

Methods

Materials

Methyl 4-aminobenzoate (Sigma Aldrich, 98%), 3,3-dimethylbutyric acid (Sigma Aldrich, 98%), 4-aminobenzyl cyanide (Sigma Aldrich, 99%), methyl 4-formylbenzoate (Sigma Aldrich, 99%), 1,4-bis-Boc-1,4,7-triazaheptane (Chem Impex, 99%), 1-ethyl-3-(3-dimethylaminopropyl)carbodiimide hydrochloride (EDC, TCI Chemicals, 98%), 4-dimethylaminopyridine (DMAP, TCI Chemicals, 99%), lithium hydroxide (LiOH, Alfa Aesar, 98%), potassium hydroxide (KOH, Alfa Aesar, 98%), hydrochloric acid (HCl, Alfa Aesar, 37%), trifluoroacetic acid (TFA, Alfa Aesar, 99%), diethylether (DEE, Acros Organics, 99%), tetrahydrofuran (THF, Acros Organics, 99%), ethyl acetate (EA, Acros Organics, 99%), hexane (HEX, Acros Organics, 99%), methanol (MeOH, Acros Organics, 99%), ethanol (EtOH, Acros Organics, 99%), dichloromethane (DCM, Acros Organics,

99%), and dimethylformamide (DMF, Acros Organics, 99%) were used as received without further purification.

Synthesis

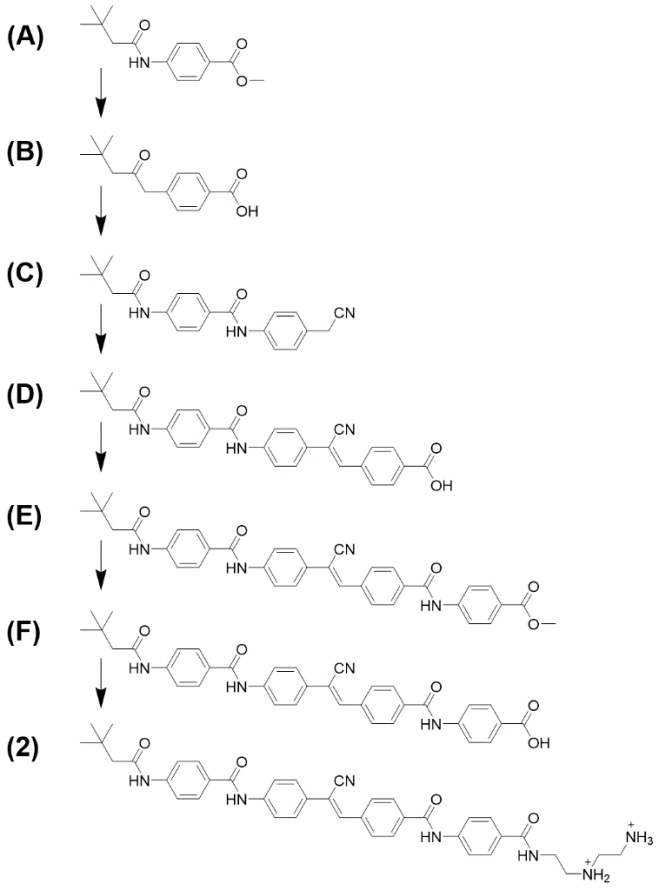

Figure 3.12 I Synthetic route to obtain the photoresponsive aramid amphiphile **2**.

Methyl 4-(3,3-dimethylbutanamido)benzoate (compound **A**): A solution of methyl 4-aminobenzoate (5.5 mmol), 3,3-dimethylbutyric acid (8.3 mmol), EDC (16.5 mmol), and DMAP (16.5 mmol) in DCM (40 mL) was stirred at room temperature for 24 h. The solution was washed with deionized water after the reaction and then extracted in DCM. The organic layer was purified by performing column chromatography with silica gel using EA:HEX = 1:1 as eluent. Yield: 81%. ^{1}H NMR (400 MHz, DMSO-*d*): δ = 7.92 (d, 2H), 7.73 (d, 2H), 3.82 (s, 3H), 2.27 (s, 2H), 1.07 (s, 9H) ppm.

4-(3,3-Dimethylbutanamido)benzoic acid (compound **B**): 10 M LiOH (5 mL) was added to a stirred solution of compound **A** (2.1 mmol) in EtOH (20 mL). The mixture was heated to 70 °C for 6 h, and then neutralized with 1M HCl solution. The precipitate was obtained by filtration and washed with water several times. The crude product was purified by reprecipitation from chloroform and methanol, and then dried under vacuum. Yield: 99%. ^{1}H NMR (400 MHz, DMSO-*d*): δ = 7.87 (d, 2H), 7.71 (d, 2H), 2.23 (s, 2H), 1.03 (s, 9H) ppm.

N-(4-(cyanomethyl)phenyl)-4-(3,3-dimethylbutanamido)benzamide (compound **C**): EDC (6.5 mmol) and DMAP (6.5 mmol) were added to a solution of compound **B** (2.1 mmol) in DMF (20 mL). After stirring at room temperature for 20 min, 4-aminobenzyl cyanide (6.5 mmol) was added as a solid and the solution was sonicated in an ultrasound bath until a clear solution was obtained. The solution was stirred for 24 h at room temperature. A precipitate formed after addition of distilled water (40 mL), which was was collected by filtration and purified by washing with copious MeOH. Yield: 79%. ^{1}H NMR (400 MHz, DMSO-*d*): δ = 7.94 (d, 2H), 7.84 (d, 2H), 7.72 (d, 2H), 7.34 (d, 2H), 4.05 (s, 2H), 2,27 (s, 2H), 1.03 (s, 9H) ppm.

(*Z*)-4-(2-cyano-2-(4-(4-(3,3-dimethylbutanamido)benzamido)phenyl)vinyl)benzoic acid (compound **D**): Compound **C** (1.6 mmol) and methyl 4-formylbenzoate (1.8 mmol) were dissolved in EtOH (40 mL) and THF (30 mL). The solution was heated in reflux under a nitrogen atmosphere, and KOH (10.3 mmol) was carefully added. The reaction mixture was cooled to room temperature after 24 h. 6M HCl solution was added to form a yellow precipitate which was filtered and washed with DCM. Yield: 88%. ^{1}H NMR (400 MHz, DMSO-*d*): δ = 8.07 (m, 3H), 8.03 (d, 2H), 7.95 (d, 4H), 7.81 (d, 2H), 7.75 (d, 2H), 2.24 (s, 2H), 1.04 (s, 9H) ppm.

Methyl (*Z*)-4-(4-(2-cyano-2-(4-(4-(3,3-dimethylbutanamido)benzamido)phenyl)-vinyl)benzamido)benzoate (compound **E**): A solution of compound **D** (0.6 mmol) in DMF (20 mL) was added to a solution of methyl 4-aminobenzoate (1.8 mmol), EDC (1.8 mmol), and DMAP (1.8 mmol) in DCM (20 mL). After stirring the mixture for 24 h at room temperature, the solvent was evaporated under reduced pressure. The product was obtained after washing with MeOH and drying. Yield: 83%. ^{1}H NMR (400 MHz, DMSO-

d): δ = 8.11 (m, 3H), 8.06 (d, 2H), 7.99 (m, 8H), 7.83 (d, 2H), 7.75 (d, 2H), 3.79 (s, 3H), 2.24 (s, 2H), 1.05 (s, 9H) ppm.

(*Z*)-4-(4-(2-cyano-2-(4-(4-(3,3-dimethylbutanamido)benzamido)phenyl)vinyl)benzamido)benzoic acid (compound **F**): 10 M LiOH (10 mL) was added to a stirred solution of compound **E** (1.5 mmol) in EtOH (30 mL). The mixture was refluxed for 3 h and then neutralized with an 1M HCl solution. The precipitate was obtained by filtration and washed with water several times. Yield: 98%. ^{1}H NMR (400 MHz, DMSO-*d*): δ = 8.13 (m, 3H), 8.01 (d, 2H), 7.97 (m, 8H), 7.83 (d, 2H), 7.74 (d, 2H), 2.25 (s, 2H), 1.04 (s, 9H) ppm.

(*Z*)-*N*1-(2-(4-(4-(2-cyano-2-(4-(4-(3,3-dimethylbutanamido)benzamido)phenyl)vinyl)benzamido)benzamido)ethyl)ethane-1,2-diaminium (**2)**: Compound **F** (0.3 mmol), 1,4-bis-Boc-1,4,7-triazaheptane (0.6 mmol), EDC (0.9 mmol), and DMAP (0.9 mmol) were dissolved in DMF (20 mL). The mixture was stirred at 25 °C for 72 h. The solvent was evaporated under reduced pressure. After addition of water, the crude mixture was filtered and washed with EA. The precipitate was then dissolved in the solution of DCM (20 mL). The mixture was held at 0 °C, and a solution of TFA (5 mL) in DCM (5 mL) was carefully added. The mixture was stirred for 3 h. After evaporating solvents, the resultant solid was washed with THF, DEE, and DCM several times. Yield: 54%.

Chemical characterization of **2**:

^{1}H NMR (400 MHz, DMSO-*d*): δ = 8.13 (m, 3H), 8.07 (d, 2H), 7.98 (m, 4H), 7.92 (m, 4H), 7.82 (d, 2H), 7.75 (d, 2H), 3.57 (m, 2H), 3.19 (m, 6H), 2.25 (s, 2H), 1.05 (s, 9H) ppm.

^{13}C NMR (400 MHz, DMSO-*d*): δ = 171.4, 167.5, 165.58, 143.2, 142.1, 141.4, 139.2, 138.3, 136.7, 129.4, 128.7, 126.9, 120.9, 119.2, 118.8, 116.9, 111.9, 49.6, 48.3, 45.1, 34.5, 32.3, 30.5 ppm.

MS (MALDI-ToF) m/z calculated: 687.84; m/z calculated for $[M+Na]^+$ adduct: 710.83; m/z found: 710.83.

Elemental Analysis calculated (%) for $C_{40}H_{45}N_7O_4$: C 69.85, H 6.59, N 14.25, O 9.30; found: C 69.84, H 6.57, N 14.24.

Sample preparation

Deionized water was added to a sample of **2** and a sonicator bath was used to promote self-assembly. After 24 h post-sonication at room temperature, **2** in its *trans* state in water was observed to form nanoribbons. Nanotubes were obtained by irradiating an aqueous solution of **2** with UV light for 1 h post-sonication. The reverse isomerization (*cis* to *trans*) was obtained by heating the solution at 80 °C for 1 h and cooling slowly to room temperature.

Characterization details

Proton (^{1}H) and carbon (^{13}C) nuclear magnetic resonance (NMR) measurements were performed on a Bruker Avance III DPX 400 with samples dissolved in deuterated dimethylsulfoxide (DMSO-*d*). The chemical shifts were measured in parts per million (ppm) downfield from tetramethylsilane.

Molecular weight analysis of final compounds was conducted on a Bruker Omniflex matrix-assisted laser desportion/ionization-time of flight (MALDI-ToF). A matrix solution was prepared by adding 15 mg of α-cyano-4-hydroxycinnamic acid to 1 mL of 1:1 water:acetonitrile by volume with 0.1% TFA, vortexing for one minute, centrifuging for 20 s, and retaining the supernatant. 10 µL of a 1 mg/mL amphiphile solution was then transferred into a centrifuge tube and diluted with the matrix solution to a 50 pmol/µL concentration. 1 µL of a 1 mg/mL calibrant solution (SpheriCal Peptide Low, Polymer Factory) in tetrahydrofuran was added to the solutions as an internal calibrant. 2 µL of the final solution was pipetted and dried onto a sample plate for analysis.

Elemental analysis (EA) of final compounds was determined using a Vario EL elemental analysis (EA) instrument. Three replicate experiments were conducted per compound.

Ultraviolet-visible (UV-Vis) absorption spectra were captured on a JASCO V760 spectrophotometer. 365 nm wavelength UV light used to irradiate samples was produced by an LED Hönle 2.0 Powerpen. UV-Vis solutions were prepared at 0.1 mg/mL.

Small angle X-ray scattering (SAXS) measurements were performed at Beamline 12-ID-B of Advanced Photon Source at Argonne National Laboratory. The X-ray radiation

energy was 13.3 keV and a Pilatus 2M detector was employed for data collection. The 2-D X-ray scattering patterns were background subtracted and processed using beamline software for reduction to 1-D data curves. Amphiphile solutions at a 30 mg/mL concentration were used for SAXS measurements.

Transmission electron microscopy (TEM) images were captured on a FEI Tecnai G2 Spirit TWIN microscope at an accelerating voltage of 120 kV. Grids were prepared for TEM experiments by depositing a 7 mg/mL amphiphile solution onto a continuous carbon grid for 10 sec, blotting to remove the solution, depositing a 1% phosphotungstic acid solution onto the grid, and blotting to remove the stain.

Nanostructure fitting to small angle X-ray scattering profiles

Fitting of SAXS data was completed in SasView software to determine the morphology of compound **1** and **2** nanostructures. Compound **1** was best fit to a lamellar_hg model, which provides separate scattering length densities for the head group and tail (including the structural domain) group. Compound **2** in its initial assembled state was best fit to a rectangular prism model; in its post-UV irradiation state was best fit to a hollow cylinder model; and in its post-annealing state was best fit to a rectangular prism model.

Statistical topographical analysis of nanoribbon contours

A solution of compound **2** nanoribbons was prepared for atomic force microscopy (AFM) analysis by sonicating for 24 h at room temperature at 30 mg/mL and diluting to a final concentration of 0.03 mg/mL. This solution was deposited onto a glass substrate which was cleaned with DI water and ethanol, dried with N_2 (*g*), and activated with a UV/ozone treatment. The solution was incubated for 5 min, and then rinsed off with DI water and dried with a N_2 stream prior to AFM imaging.

Images of compound **2** nanoribbons were captured in tapping mode in ambient air on a Bruker/JPK Nanowizard 4 AFM. Olympus AC160TS-R3 cantilevers were used, with a nominal spring constant of 26 N/m and a resonance frequency of approx. 300 kHz 512

x 512 pixel AFM images were produced at a 3 – 10 Hz scanning speed. A representative AFM image is shown in Fig. S17.

Nanoribbon shape fluctuations were extracted from AFM images and statistically processed using Easyworm software.[34] In this study, the software was used to produce parametric splines from the contours of n = 96 nanoribbons. These parametric splines record coordinates of all knots along the ribbons, and each combination of knots is analyzed to obtain a secant length L from which the midpoint of the secant deviates from the nanoribbon contour by the distance δ. A persistence length *P* is subsequently extracted via a least-squares fitting a worm-like chain model for semi-flexible polymers to the data, which relates the mean-square of δ to the secant length L according to: $< \delta^2 > = \mathrm{L}^3/(48 \times \mathrm{P})$. Thus, a higher persistence length corresponds to a smaller orientation change over a given distance along a nanoribbon's contour. The flexural rigidity F is calculated using $\mathrm{F} = \mathrm{P} \times \mathrm{k_B T}$, where the persistence length is scaled by thermal energy. Using this, the Young modulus *E* is obtained by dividing the flexural rigidity by the nanoribbon's area moment of inertia, $\mathrm{E} = \mathrm{F}/\mathrm{I}$. We use the AFM height of d = 3.2 ± 0.8 nm as the nanoribbon diameter in calculating the moment of inertia, $\mathrm{I} = \pi \cdot \mathrm{d}^4/64$, as in our previous study.[30]

Atomic force microscopy

Atomic force microscopy (AFM) images which complement the investigation into the Tyndall effect were recorded on a Park Systems NX10. A 7 mg mL^{-1} solution of **2** after self-assembly in water was diluted to 0.01 wt. %, and then a 50 μL droplet solution was deposited onto a freshly cleaned substrate. This substrate was prepared through a plane cleavage of mica, and cleaning with water several times. A PPP-NCHR non-contact cantilever was utilized to produce these images.

Wide-angle X-ray diffraction

One dimensional (1D) wide-angle X-ray diffraction (WAXD) experiments were conducted on a Bruker D8 Discover using Cu K_α radiation. The diffraction peak positions and widths were calibrated with crystalline silicon powder. Background scattering was

subtracted from the samples using instrument software. 30 mg mL^{-1} solutions of compound **2** nanoribbons and nanotubes were lyophilized for WAXD analysis.

Chapter 4

Antifouling surface coatings from self-assembled zwitterionic aramid amphiphile nanoribbons

This chapter was adapted from the publication "Antifouling surface coatings from self-assembled zwitterionic aramid amphiphile nanoribbons," originally published in Advanced Materials Interfaces.[157]

Abstract: Zwitterionic surfaces have been increasingly explored as antifouling coatings due to their propensity to resist protein, bacterial, and cell adhesion, and are typically applied as polymeric systems. Here, we report the self-assembly of strongly interacting small molecule amphiphiles to produce nanoribbons for antifouling applications. Synthesized amphiphiles spontaneously form microns-long nanoribbons with nanometer-scale cross-sections, and intrinsically display a dense coating of zwitterionic moieties on their surfaces. Substrates coated with nanoribbons demonstrate concentration-dependent thicknesses and near superhydrophilicity. We then probe these surface coatings for antifouling properties and demonstrate substantial reductions in protein adsorption, bacterial biofilm formation, and cell adhesion relative to uncoated controls. Harnessing cohesive small molecule self-assembling nanomaterials for surface coatings offers a facile route to effective antifouling surfaces.

Introduction

The adsorption of biomolecules, microorganisms, and cells to material surfaces is a long-standing challenge for a wide range of biomedical and industrial applications, including preserving safe hospital environments,[158, 159] maintaining sterile medical devices and minimizing degradation-inducing immune responses to implants,[160-164] reducing impacts to energy infrastructure,[165, 166] and sustaining materials in marine environments.[167, 168] Currently, harmful biocidal chemicals are used in industrial settings, risking public health and environmental contamination, spurring interest in alternative strategies.[169-171] Furthermore, the U.S. Centers for Disease Control and Prevention estimates that 1 in 31 U.S. patients has at least one infection during their hospital care via exposure to foreign microbes. These healthcare-associated infections result in close to 100,000 deaths annually.[163, 168, 172, 173]

Historically, antifouling material design has used hydrophilic surface chemistries to control interactions at the interface between the material and its microenvironment. Rapid adsorption of proteins (i.e. biofouling) onto a material surface occurs immediately upon exposure to a non-sterile environment, facilitating the attraction of other biological components and determining the material's biological fate and function.[174, 175] Hydrophilic surfaces form a strong hydration layer that inhibits protein adhesion by creating significant energetic penalties to disrupt tightly coordinated solvent interactions, which may be further aided by steric effects.[176-178] The hallmark example of this application is the coating of surfaces with poly(ethylene glycol) (PEG) to imbue antifouling properties. These "PEGylated" materials are widely accepted to resist nonspecific protein adsorption, but PEG is susceptible to loss of function in biological milieu from long-term oxidation, and requires optimization for grafting to many substrates.[179-182] An increasing body of evidence also indicates that the nonspecific adsorption of immunogenic proteins on PEG-coated surfaces implanted *in vivo* can induce the production of PEG-specific antibodies, in turn eliciting rejection of implanted devices.[183, 184]

Zwitterionic chemistries have been increasingly explored as an alternative to PEG-modified surfaces because of their intrinsic capacity to resist biofouling. Zwitterionic materials, composed of molecules with both positive and negative charges, provide a physical and electrostatic barrier to adsorption through robust surface hydration.[72, 185-187] Polymers containing phosphorylcholine, sulfobetaine, and carboxybetaine zwitterionic moieties have been demonstrated to significantly reduce nonspecific protein adsorption,[179, 185, 188] and paved the way for research into a growing number of polymeric zwitterionic systems.[189-191]

Obtaining nanomaterials through small molecule self-assembly offers an alternative approach to polymeric systems for producing zwitterionic-coated surfaces. Amphiphilic self-assembly produces internally organized nanostructures with surface presentations, chemistries, and dynamics that are tunable through molecular design.[41, 68, 192-194] Importantly, nanomaterials constructed through the self-assembly of zwitterionic small molecule amphiphiles offer extremely high surface densities of zwitterionic moieties that are resistant to biofouling. To this end, we propose that several criteria should be met to form effective antifouling surface coatings from small molecule supramolecular assemblies: (1) the molecular assemblies should be sufficiently stable to maintain their structure upon drying for application; (2) the nanostructures should take on an appropriate geometry for substrate coating and aspect-ratio to provide dense surface coverage; and, (3) the surface should produce a substantial hydration layer that is protective against biofouling.

Here, we report the application of supramolecular nanoribbons from zwitterionic aramid amphiphiles (ZAAs) to antifouling surface coatings (**Figure 1**). ZAAs have previously been shown to undergo spontaneous self-assembly in water to form microns-long nanoribbons with robust mechanical properties.[51] To meet the above criteria, we: (1) synthesize amphiphiles with a triaramid structural domain – the aramid amphiphile motif – into the molecular design to tightly coordinate adjacent amphiphiles; (2) select an unobtrusive branched aliphatic tail group to promote assembly into high-aspect-ratio nanoribbons; and (3) incorporate a sulfobetaine head group to form nanostructures with zwitterionic surfaces. This molecular design imparts stability on the resulting self-

assembled nanostructures by incorporating a dense network of hydrogen bonds and π-stacking interactions between neighboring molecules. As a consequence, aramid amphiphile-based nanomaterials exhibit suppressed dynamic instabilities relative to conventional small molecule assemblies and realize mechanical properties rivaling silk.[51] To produce antifouling surface coatings, we self-assemble the ZAAs in water, drop-cast the resulting nanoribbon suspension onto substrates, and form thin film coatings via air drying, which we subsequently test for resistance to fouling by proteins, bacteria, and cells.

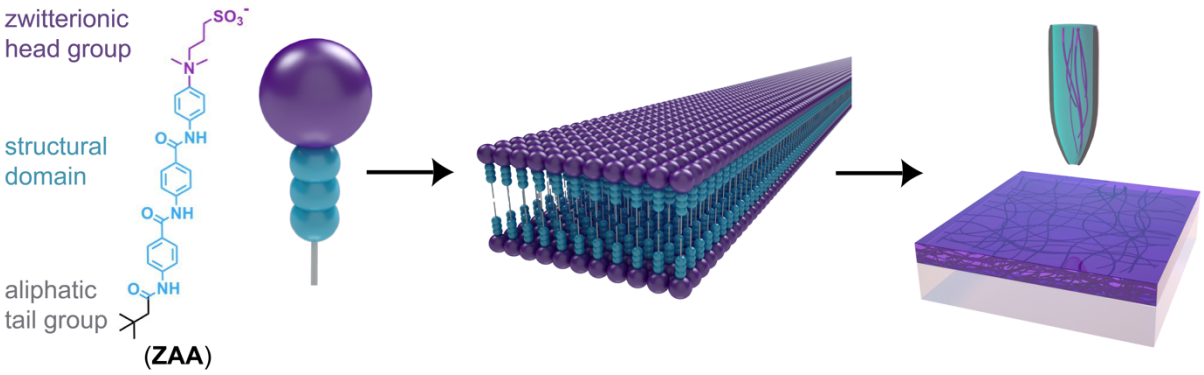

Figure 4.1 l Surfaces coated with zwitterionic aramid amphiphile (ZAA) nanoribbons are resistant to biofouling. Aramid amphiphiles composed of a zwitterionic head group, triaramid structural domain, and hydrophobic tail spontaneously self-assemble in water to form microns-long nanoribbons. Suspensions of these stable nanoribbons can be deposited and dried onto surfaces to form a dense nanoribbon mesh that is resistant to biofouling. Molecule and nanoribbon schematic reproduced with permission.[41] 2021, Springer Nature.

Results and Discussion

We prepared ZAAs by first synthesizing the hydrophobic portion of the molecule (aliphatic tail and aramid repeat units) via alternating carbodiimide-mediated coupling reactions and conventional deprotection reactions. We subsequently added the zwitterionic head group through quaternization of a pendant tertiary amine with propanesultone (molecule in Figure 1). The protocol to obtain this compound is described elsewhere.[51] A combination of proton (^{1}H) NMR and mass spectrometry were used to characterize the product (see Experimental Details).

ZAAs spontaneously self-assemble to form microns-long nanoribbons in water after 1 h of sonication at room temperature (1 mg mL^{-1}, deionized water), as observed with transmission electron microscopy (**Figure 2A**). We combine cryogenic transmission electron microscopy (cryo-TEM, **Figure 2B**), atomic force microscopy (AFM, **Figure 2C**), and small angle X-ray scattering (SAXS, **Figure 2D**) to determine the dimensions of the nanoribbon cross-sections. The SAXS profile is best fit to a lamellar model, which defines a nanoribbon thickness of 3.9 nm, and AFM identifies a nanoribbon width of 5.1 nm. These cross-sectional dimensions are corroborated by cryo-TEM and match previously reported dimensions.[51]

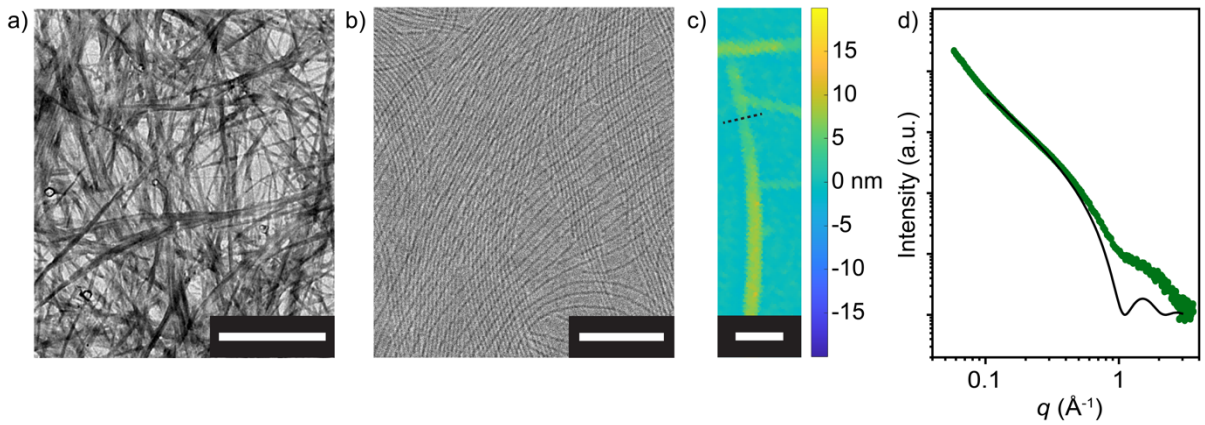

Figure 4.2 I ZAAs form nanoribbons upon self-assembly in water. **a,** The self-assembly of ZAAs into microns-long nanoribbons is observed in transmission electron microscopy. Scale bar: 1 μm. **b,** Analysis of cryogenic transmission electron microscopy images of the nanoribbons is used to extract 3.9 x 5.1 nm nanoribbon dimensions. Scale bar: 100 nm. **c,** Atomic force microscopy corroborates a 5.1 nm nanoribbon width (dotted line). Scale bar: 200 nm. **d,** Fitting the small angle X-ray scattering profile (green circles) of a ZAA nanoribbon suspension in water to a lamellar model (black line) corroborates a nanoribbon thickness of 3.9 nm.

Aqueous nanoribbon suspensions were deposited and air-dried onto substrates as a simple route to producing antifouling surface coatings. These coatings harness the thermal stability of ZAA nanoribbons, which has been previously demonstrated up to 250 °C.[195] We find with scanning electron microscopy that the nanoribbons maintain their three-dimensional architecture, aggregate into bundles, and form a dense mesh (**Figure 3A**). 250 μL of a 1 mg mL^{-1} nanoribbon solution is observed as the minimum volume

needed to fully disperse across 15 mm diameter circular glass discs, which fit the bottom of a 24-well plate. Therefore, we select 250, 300, 500, and 700 µL depositions onto the discs for further analysis, which equates to 1.4, 1.7, 2.8, and 4.0 µg mm^{-2} coatings, respectively. Through surface profilometry, we find that coating thickness linearly increases with coating density ($R^2 > 0.99$), with 1.4, 1.7, 2.8, and 4.0 µg mm^{-2} coatings having average thicknesses of 1.08, 1.24, 1.79, and 2.48 µm, respectively (**Figure 3B**).

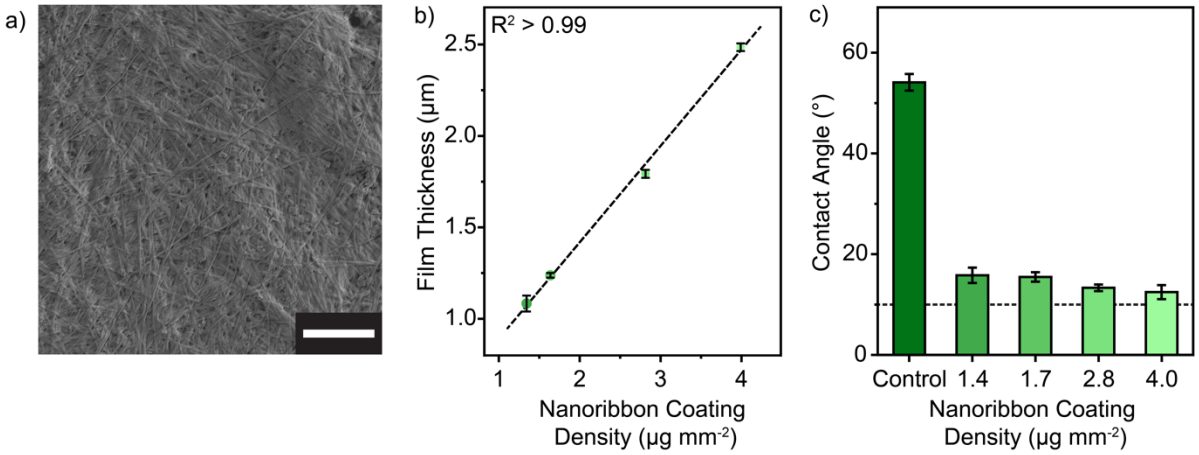

Figure 4.3 l Nanoribbon-coated surfaces show a linear thickness dependence with coating density and are highly wetting. **a**, A representative scanning electron micrograph of nanoribbon coated surfaces shows maintenance of the three-dimensional structure of the nanoribbons upon drying to form a dense mesh of nanoribbon bundles. Scale bar: 2 µm. **b**, Profilometry measurements of zwitterionic nanoribbon coatings indicate a linear relationship (dotted line) between coating density and film thickness. Measurements are shown as mean ± standard deviation (n = 5). **c**, Contact angle measurements as a function of nanoribbon coating density show coated surfaces are highly hydrophilic and offer a significantly lower contact angle than an uncoated glass control. The horizontal dashed line at a 10º contact angle indicates the threshold for superhydrophilicity. Measurements are shown as mean ± standard deviation (n = 5).

Finally, we employ contact angle goniometry to probe the wetting properties of nanoribbon-coated surfaces (Figure 4.3C). We hypothesize that the surfaces should be highly wetting due to the propensity of the zwitterionic moieties to form a hydration layer. The uncoated glass disc control exhibits a water contact angle of approx. 54º. In contrast, surfaces with ZAA nanoribbon coatings have water contact angles ranging approx. 13 to 16º, nearing superhydrophilicity.[196] The high wettability of the nanoribbon coated surfaces confirm favorable water-nanoribbon interaction.

The instantaneous adsorption of proteins onto the surface of any biomaterial has drastic effects on its downstream performance. Therefore, albumin and lysozyme were initially chosen as model proteins to quantify antifouling. Anionic albumin proteins, measuring approx. 40 mg/mL in blood, are the most prevalent proteins within human serum.[197] Lysozyme, an innate immune response enzyme, is positively charged at physiologic pH and is commonly used as a representative cationic macromolecule.[198] Studying antifouling of these two model proteins offers insight into the broad-ranging capabilities of the nanoribbon coatings to prevent fouling from different charges and classes of proteins.

We observe that the nanoribbon surface coating greatly decreases albumin and lysozyme fouling, in line with similar contact angles across thicknesses. Average adsorption values of bovine serum albumin (BSA) on coated substrates range from approx. 2 to 3 percent relative to uncoated glass controls (Figure 4.4a). Similarly, average lysozyme adsorption values range from approx. 2 to 5 percent relative to uncoated glass controls (Figure 4.4b). The nanoribbon coatings also prevent the adsorption of proteins within human serum, a complex system representative of biological environments. Average protein adsorption decreases to between approx. 47 and 75 percent fouling relative to uncoated glass controls for human serum incubated on nanoribbon coated surfaces (Figure 4.4c). The lower effectiveness of the nanoribbon coatings against human serum and its sensitivity to coating thickness is likely influenced by its higher total concentration of proteins (approx. 60-80 mg/mL in blood[199], diluted here 1:10) than in the individual BSA and lysozyme experiments (performed at 1 mg mL^{-1}). Furthermore, smaller proteins and peptides present in human serum may diffuse more easily through the nanoribbon mesh to the glass substrate.[199]

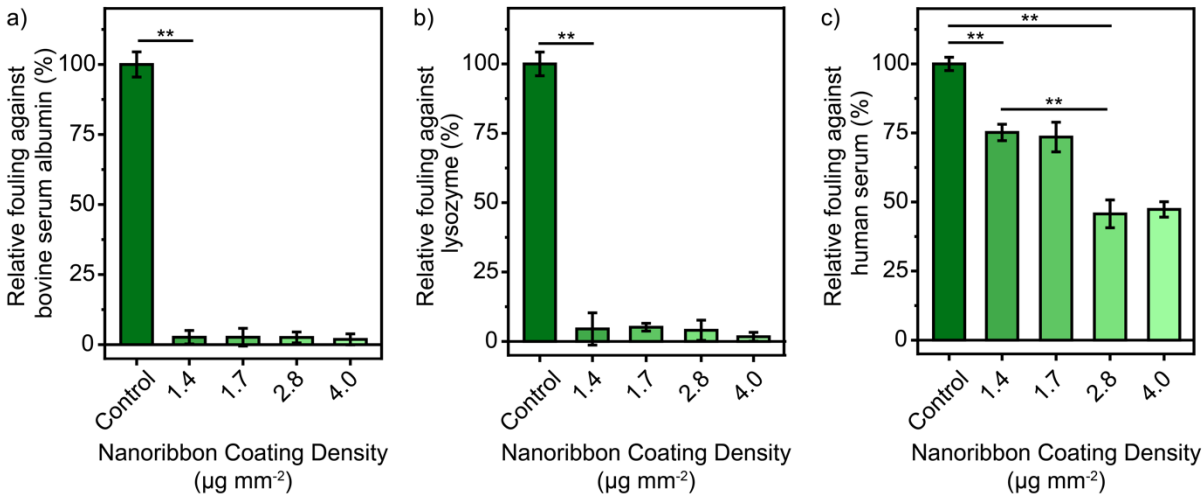

Figure 4.4 l ZAA nanoribbon coatings resist nonspecific protein adsorption. **a,** The nanoribbon coating reduces bovine serum albumin adsorption 98% relative to an uncoated control, statistically independent of coating density. **b,** The nanoribbon coating reduces lysozyme adsorption 95-98% relative to an uncoated control, nearly independently of coating density. **c,** The nanoribbon coating reduces nonspecific protein adsorption from human serum approximately 25% for 1.4 and 1.7 μg mm^{-2} nanoribbon coatings, and approximately 50% for 2.8 and 4.0 μg mm^{-2} nanoribbon coatings relative to an uncoated control. Data shown as mean ± standard deviation of n = 3 samples for each coating density. Statistical significance determined by a two-tailed Welch's t-test followed by a Bonferroni correction (**, $p < 0.05$ after Bonferroni correction).

Next, we investigated the adsorption of microbes onto surfaces coated with ZAAs. Bacteria readily colonize abiotic surfaces,[200, 201] and adhesion on biomaterials can enable the production of biofilms[202] that are known to require 100- to 1000-fold increases in antibiotics to eradicate relative to their planktonic, free-swimming counterparts. *Pseudomonas aeruginosa*, a model Gram-negative opportunistic bacterium, is an infamous 'ESKAPE' pathogen that poses a dire public health threat.[203] Notably, its biofilm formation is in part responsible for its antibiotic tolerance, rendering most current therapies ineffective.[203, 204] Reducing surface attachment of microbes, such as *P. aeruginosa*, onto substrates represents a promising solution to inhibit biofilm production without the use of biocides, negating the most important factor leading towards antibiotic resistance.[205]

We cultured *P. aeruginosa*, stained in green, for 48 h on an uncoated glass surface and observe a dense attachment of microbes and production of a biofilm matrix (Figure 4.5A). When we cultured the same bacterium on nanoribbon-coated surfaces, we identify

a sensitivity to increasing nanoribbon coating concentrations, whereby fewer and fewer bacteria attach onto the surface (Figures 4.5B-E). We observe no difference in surface roughness, porosity, morphology, or coverage through profilometry and SEM between substrates with different surface coating densities. Therefore, we attribute this dependence to increasing tortuosity to reach the glass substrate and decreasing adhesion sites for bacterial attachment. By quantifying the biofilm biomass using COMSTAT2,[206, 207] a statistically significant reduction can be observed even with the lowest coating thickness used (Figure 4.5F). At and above a 2.8 μg/mm^2 coating, virtually no biofilm biomass is detected, indicating complete surface antifouling.

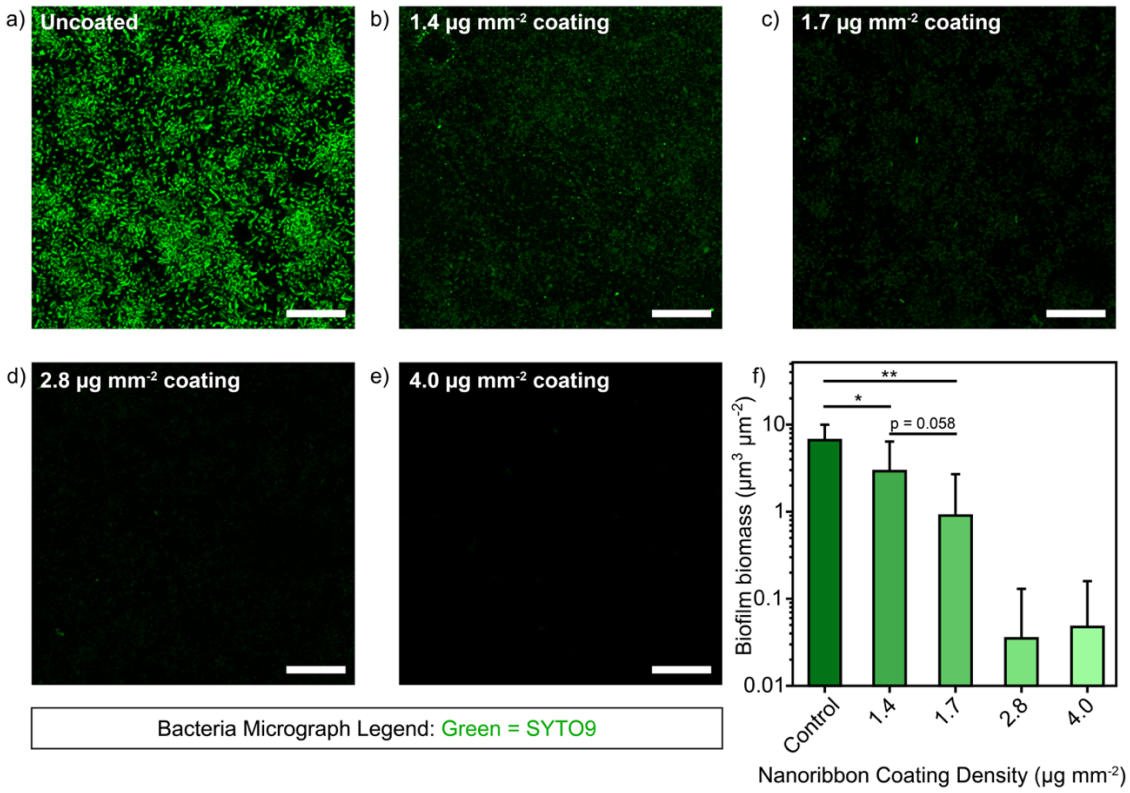

Figure 4.5 I Increasing densities of surface-bound ZAA nanoribbons results in significant reduction of biofilm biomass over 48 h of culturing. **a**, A representative max intensity z-stack confocal microscope image illustrates microbial (green) adhesion on glass surfaces with no surface treatment. Scale bar: 25 μm. **b-e**, Representative microscope images demonstrate reductions in biomass with increased concentrations of nanoribbon deposition onto the surface. Scale bar: 25 μm. **f**, Statistically significant reductions in biofilm biomass are seen at all coating densities tested, as calculated by COMSTAT2.[206, 207] Data shown as mean ± standard deviation of triplicate wells with five different fields for each well. Statistical significance determined by a two-tailed Welch's t-test followed by a Bonferroni correction (*, $p < 0.05$ before Bonferroni correction; **, $p < 0.05$ after Bonferroni correction).

Finally, we investigated the prevention of cell attachment to ZAA nanoribbon-coated substrates. We selected the hASC-SVG-p12 cell line, a type of human adipose stem cell (hASC), for this study. hASC-SVG-p12 is a cell line used in a broad range of research, including studies of human immunodeficiency virus (HIV) and Alzheimer's disease.[208, 209] Notably, this cell line is capable of being cultured directly on uncoated glass substrates with high attachment, viability, and proliferation.

To test for inhibition of cell attachment to nanoribbon-coated surfaces, we cultured hASC on uncoated and nanoribbon-coated discs for three days and analyzed the surface-bound cell number and density using a live-dead assay. The cell density was calculated for live and dead cells, stained in green and red, respectively, with fifteen randomly chosen fields in each group. Cells cultured on the uncoated substrate show the highest density as expected (**Figure 6A**). In contrast, cells cultured on nanoribbon coated-discs demonstrate a significantly lower density (**Figure 6B-F**). We observe fewer viable cell clusters and dead cells on the nanoribbon-coated surfaces. Of note, we observe a steep decrease in the total cell density from the control group to the less dense nanofiber coating and a coating thickness-dependence to cell density, likely resulting from inhibited diffusion to the glass substrate and lower adhesion sites with increasing coating thicknesses. We also observe that while the total density of dead cells decreases with the addition of a nanoribbon coating, the ratio of dead-to-live cells increases with higher surface coating densities. This indicates some evidence of cytotoxicity which is likely attributed to lowered cell adhesion caused by the coating, and may partially also be attributed to the stiffness of the nanoribbons comprising the coating.[51]

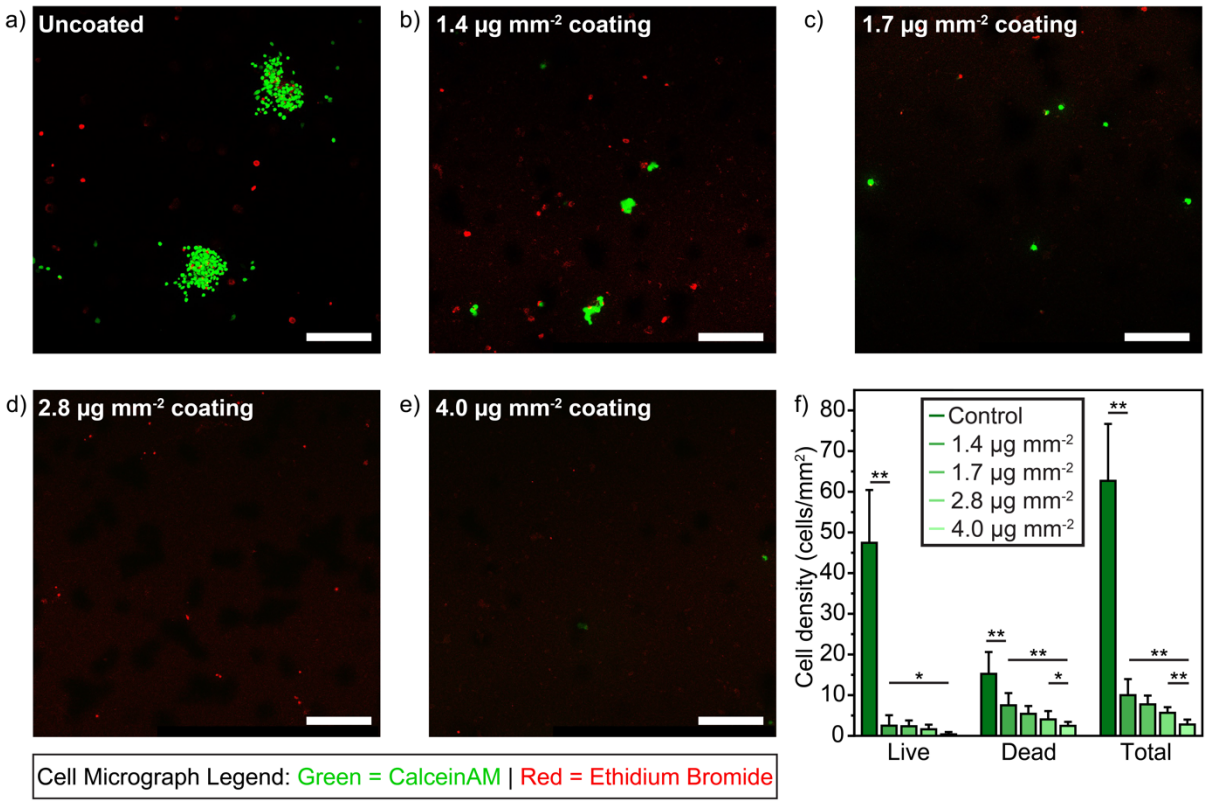

Figure 4.6 l Nanoribbon-coated surfaces show significantly lower adhered cell densities than uncoated controls after 3 days. Fluorescent microscopy images at a 20X magnification of **a**, an uncoated control; and **b**, 1.4 μg/mm^2; **c**, 1.7 μg/mm^2; **d**, 2.8 μg/mm^2; and **e**, 4.0 μg/mm^2 nanoribbon coatings illustrate decreasing cell attachment with increasing nanoribbon coating thickness. Scale bars: 250 μm. **f**, Computational analyses of the fluorescence micrographs reveal statistically significant adhered cell densities between coated and uncoated substrates. Data shown as mean ± standard error measurement of triplicate wells with 15 different fields for each well. Statistical significance determined by a two-tailed Welch's t-test followed by a Bonferroni correction (*, $p < 0.05$ before Bonferroni correction; **, $p < 0.05$ after Bonferroni correction).

Readily applied coatings which offer protection against the adhesion of biological components are critical to the function of materials in a broad range of application spaces.[158-173] Harnessing control over the surface chemistry, internal stability, and geometry of supramolecular nanostructures offers a route to produce thin films which minimize nonspecific interactions with biomolecules. In this work, we investigated zwitterionic aramid amphiphile (ZAA) nanoribbons which incorporate: a zwitterionic head group to produce a highly hydrated surface; a structural domain to provide internal cohesion; and an optimized geometry to yield high-aspect-ratio nanostructures to

significantly reduce biofouling. Upon addition of water, ZAAs spontaneously formed microns-long nanoribbons that maintain structure when dried to readily produce dense nanoribbon mesh coatings. These coatings offered concentration-dependent thicknesses and contact angles approaching superhydrophilicity, indicative of strong nanoribbon-water interactions at the exposed coating surface. These surfaces showed resistance to protein fouling, a two orders of magnitude reduction in bacterial adhesion, and suppressed cell-mediated attachment. The simple strategy to producing water-coordinating surfaces reported here offers insight into extending small molecule self-assembled materials towards effective antifouling coatings.

Methods

All materials are from Sigma-Aldrich unless specified otherwise.

Chemical characterization

Proton (^{1}H) nuclear magnetic resonance (NMR) spectroscopy to analyze the chemical structure of the synthesized amphiphile and intermediates was performed on a Bruker Avance III DPX 400. NMR solutions were prepared by mixing 20 mg of dried sample powder with 500 µL deuterated dimethylsulfoxide (DMSO-d_6). (400 MHz, DMSO-d_6, δ): 10.56 (s, 1H, NH), 10.37 (s, 1H, NH), 10.11 (s, 1H, NH), 8.01 (m, 8H, Ar), 7.88 (d, 2H, Ar), 7.78 (d, 2H, Ar), 3.99 (m, 2H, CH_2), 3.57 (s, 6H, CH_3), 2.42 (t, 2H, CH_2), 1.67 (m, 2H, CH_2), 1.06 (s, 9H, CH_3) ppm.

Mass spectrometry to confirm the molecular weight of the synthesized zwitterionic aramid amphiphile was carried out on a Bruker Autoflex LRF Speed matrix assisted laser desorption/ionization-time-of-flight (MALDI-ToF) spectrometer. A matrix solution for analysis was prepared by mixing excess (>10 mg/mL) α-cyano-4-hydroxycinnamic acid (CHCA) with 500:500:1 solution (by vol.) of deionized water:acetonitrile:trifluoroacetic acid, vortexting for 30 s, centrifuging for 1 min, and retaining the supernatant. The solution for MALDI-ToF testing was prepared by mixing 25:25:1 (by vol.) of this matrix supernatant, a 1 mg/mL solution of the zwitterionic aramid amphiphile in deionized water,

and a 1 mg/mL solution of SpheriCal Peptide Low (Polymer Factory) in hexane as an internal calibrant. A 3 µL droplet of this MALDI-ToF solution was dried onto a sample plate for analysis. MALDI-MS, *m*/*z*: $[M + H]^+$ calc'd for $C_{31}H_{38}N_4O_6S$, 594.251; found, 594.257.

Observing nanoribbon self-assembly

Transmission electron microscope (TEM) images were captured on a FEI Tecnai G2 Spirit TWIN at an accelerating voltage of 120 kV. To prepare the sample for observation, 5 µL of a 1 mg/mL solution of assembled ZAAs was pipetted onto a TEM grid (200 mesh, carbon film, Electron Microscopy Sciences), allowed to rest for 20 sec, and wicked off with tissue paper. The grid was then stained with 5 µL of 1% phosphotungstic acid solution (Electron Microscopy Sciences) which was pipetted onto the grid, rested for 20 sec, and then wicked off.

Cryogenic transmission electron microscope (cryo-TEM) images were captured on an FEI Tecnai Arctica microscope at an accelerating voltage of 200 kV and with image defocus between -1.5 and -3.5 µm. Holey carbon grids (Ted Pella, 300 mesh, Cu) were prepared using an FEI Vitrobot Mark IV. A 3 µL droplet of a 2.0 mg/mL amphiphile solution was pipetted onto the glow-discharged grids in 100% humidity. Grids were blotted for 4 s, plunged into liquid ethane, and stored and imaged in liquid nitrogen.

The small angle X-ray scattering (SAXS) profile of a 1 mg/mL aqueous solution of nanoribbons in a quartz capillary (2 mm diameter, Hampton Research) was obtained at the Advanced Photon Source at Argonne National Laboratory (beamline 12-ID-B) with a 13.3 keV X-ray radiation energy. A DECTRIS PILATUS 300 K detector captured the two-dimensional X-ray scattering pattern. Beamline software was used to subtract water and capillary background and reduce the pattern to a one-dimensional curve. The data was fit in SasView using computed X-ray scattering length densities (SLDs) of 9.44×10^{-6} Å^{-2} for solvent (water), 9.49×10^{-6} Å^{-2} for the amphiphile head group region, and 10.9×10^{-6} Å^{-2} for the amphiphile structural domain and tail group region. Fitting was attempted to lamellar, rectangular prism, and cylindrical models which allow for separate SLDs for head and tail group domains. The rectangular prism and cylindrical models fit to non-

physical values based on dimensions observed in TEM and Cryo-TEM, so we selected the lamellar model to extract a nanoribbon thickness.

Surface coating properties

Scanning electron microscope (SEM) images were taken on a Zeiss Merlin High Resolution SEM with a 2 kV accelerating voltage in secondary electron mode. To prepare the sample for observation, a 50 µL droplet of a 1 mg/mL solution of assembled ZAAs was pipetted onto an SEM stub covered in copper tape and dried. The stub was then coated with a 10 nm Au layer (EMS Q150T ES coater) to prevent sample charging.

Coating thickness was analyzed on a Bruker Dektak DXT-A Stylus profilometer equipped with a 2 µm diameter stylus operating at a 2 mg stylus force. Nanoribbon-coated glass discs were scratched in their centers to reveal the underlying glass surface, and height profiles were captured across these scratches. The film thickness for each coating density is reported as average ± standard deviation for n = 5 technical replicates.

Contact angle measurements were performed on a Ramé-Hart 500-F1 goniometer. 2 µL droplets of deionized water (HPLC grade) were dispensed onto control and nanoribbon-coated glass coverslips and equilibrated for one minute. Side-view photographs of the droplets were then captured and contact angle was measured on both sides of the water spherical cap using DROPimage Advanced software. Contact angles are reported as average ± standard deviation for n = 5 independent replicates.

Protein fouling

Aqueous suspensions of ZAA nanoribbons (250 µg, 300 µg, 500 µg, and 700 µg from 1 mg/mL solutions) were dropcast onto glass discs (15 mm diameter, German glass, Electron Microscopy Sciences) and allowed to dry at room temperature. 100 µL droplets of 1 mg/mL solutions of bovine serum albumin (BSA) and lysozyme in phosphate buffered saline (PBS), and 10x diluted human serum (human male AB plasma, sterile-filtered) were dropcast onto the discs and incubated in a humidified oven at 37 ºC for 2 h. Discs were washed four times with PBS and transferred to 24-well plates with 1 mL of 2% (w/w) sodium dodecyl sulfate (SDS), which were placed on a shake plate for 1 h to detach

adsorbed protein. A Micro BCA Protein Assay Kit (ThermoFisher Scientific) was used to determine the concentration of adsorbed protein for each sample. Measurements were taken using a PerkinElmer LAMBDA 850+ UV/Vis spectrophotometer set to 562 nm and averaged between 3 replicates, with background contributions to the protein assay from nanoribbons desorbed by the SDS detergent solution subtracted from each sample.

Bacteria culture, growth, and imaging

P. aeruginosa PAO1 (ATCC 15692) from a 20% frozen glycerol stock stored at -80 ºC was streaked onto a Luria-Bertani agar (LB, Lennox) petri dish and grown overnight at 37 ºC. A single colony was picked, cultured overnight at 37 ºC, and shaken at 250 rpm in Cation Adjusted Mueller Hinton-Broth (CAMHB), which is Mueller-Hinton Broth supplemented with 25 μg mL^{-1} calcium chloride and 12.5 μg/mL magnesium chloride.

Biofilm Growth and Staining

Nanoribbons were dropcast into wells of a glass bottom, black chimney 24-well microtiter plate (Grenier Bio) and allowed to dry. Overnight cultures of PAO1 were subcultured in CAMHB for 4-6 h to reach mid-log phase growth and normalized to an optical density (OD_{600}) of 0.01. 1 mL of bacterial suspension in 10% CAMHB in 150mM sodium chloride was added on top of the dried nanoribbon coating in each of the wells. Biofilms were grown statically in a humid chamber at 37 ºC for 48 h.

After 48 h of growth, biofilms were washed three times with 150 mM sodium chloride, ensuring that 1mL of sodium chloride is added first before removing 1 mL so as not to dry out the biofilm. On the final wash, 1.1 mL of solution was removed and 100 μL of 20 μM SYTO9 dye was added to each well to stain the microbes. Biofilms were stained statically for 30 minutes in the dark at room temperature, and then washed again three times with 150 mM sodium chloride before imaging.

Image acquisition was performed using a confocal laser scanning microscope (LSM 800, Zeiss) with a 63x oil immersion magnification lens, and a step size of 0.5 μm. The excitation wavelength for SYTO9 was set to 488 nm, and fluorophore emission was read at 510 nm. At least three independent wells and five images from each well were taken

and analyzed for each condition. Biofilm biomass was quantified using COMSTAT2.[206, 207] Images shown in Figure 4.5 are Z-stack projections of the maximum intensity, as performed in FIJI.

Cell attachment and imaging

All human material work was performed with the approval of the Institutional Review Board of Harvard Medical School. Human astroglia cells SVG-p12 (hASC), obtained from ATCC (US), were described in previous studies [210]. Cells were grown onto Akron flask (surface 75 cm^2, vented cap, sterile, Nunclon Delta) in DMEM/F12 medium (Gibco) in a low oxygen condition incubator (37 ºC, 5% O_2, 5% CO_2, 100% humidity) as a monolayer culture to achieve high density. Upon reaching 80% confluence, cells were passaged using 10X TrypZean and Hank's Balanced Salt Solution (HBSS, no calcium, no magnesium, ThermoFisher). Cell number and viability were estimated after each passage using Trypan blue and a hemocytometer (Countess™ II FL Automated Cell Counter, Thermo Fischer scientific). Cells were then re-plated into a T75 flask at a density of 15,000 cells cm^{-2} in DMEM/F12 medium.

10^5 cells/mL suspended in saline or medium (previously described) were pipetted onto nanoribbon-coated or uncoated glass discs. After 3 days of incubation with medium or PBS, cells were incubated with 2.5 µM calcein AM (FITC laser line) and 10 µM ethidium bromide (Cy3 laser line) in PBS for 15 min at 37 °C and 5% CO_2. hASC were then washed three times with PBS for 10 min at room temperature. Nanoribbon-coated coverslips were mounted on poly-L-lysine microscope slides (1mm thickness, 75 mm length, 25 mm width, Thermo Scientific Shandon) with low viscosity slide mounting medium (Fisher Scientific) before imaging with an epifluorescence confocal microscope (Leica SP8, USA), for live/dead imaging.

All samples were analyzed and images were taken using a Leica SP8 confocal microscope. Images were taken with sequential scanning at 1024 x 1024 resolution with the following laser intensities and characteristics: FITC-HyD at 4.3% with line average of 2 and gain of 107%, Cy3-HyD at 3.9% with line average of 2 and gain of 105%. hASC viability images were taken at 20X magnification with a Z-stack of 50 µm and 10 steps,

and maximum projection was applied as quantification. Cells in 15 randomly-selected maximum-projected fields of view were counted with a cell counting and analyzing image processing algorithm.[211]

Chapter 5

Aramid amphiphile nanoribbons for the remediation of lead from contaminated water

This chapter was adapted from the publication "Aramid amphiphile nanoribbons for the remediation of lead from contaminated water," originally published in Environmental Science: Nano.[212]

Abstract: Lead poisoning causes over one million deaths annually, leading to the designation of lead as one of the World Health Organization's "ten chemicals of major public health concern". To address this crisis, high surface area nanomaterials offer promise for producing miniaturized technologies capable of effective lead remediation. We present small molecules that spontaneously self-assemble in water to form nanoribbons with lead-chelating surface groups. While supramolecular nanostructures are typically fragile, we incorporate hydrogen bonding aramid domains to suppress exchange dynamics, ultimately leading to nanoribbons with structural integrity. By designing each amphiphile to have a chelating head group, every moiety on the nanoribbon surface is capable of capturing lead from the aqueous environment. The nanoribbons' remediation capacity is affected by pH and the presence of competing cations, and can be modulated by head group choice. We demonstrate that design of small molecules is a route to new ion-selective chelating nanomaterials with tunable surface chemistries, and thereby demonstrate the potential of small molecule self-assembly for heavy metal remediation.

Introduction

Self-assembled nanostructures from small molecule amphiphiles exhibit high surface areas and tuneable surface chemistries, and are readily scalable.[42, 52, 68, 213, 214] These properties have led to their extensive investigation as a platform for biomedical applications, including as materials for regenerative medicine, drug delivery, or biosensing.[94, 215, 216] In these environments, the dynamic nature of small molecule assemblies is harnessed as a design feature to mimic those of natural systems.[74-76] Such dynamics further enable the sensitivity of molecular assemblies to changes in their solvent environments, such as fluctuations in pH or temperature.[217, 218] However, this property limits their application space to intentionally dynamic materials.

Molecular self-assembly could offer notable advantages to applications in non-biological contexts if their typical dynamic instabilities were overcome. In particular, self-assembled nanomaterials could provide a new strategy for point-of-use remediation of contaminants from drinking water. Surface areas on the order of hundreds of m^2/g, resulting from nanostructure length scales determined by the length of the constituent amphiphiles[68, 219], may provide a platform for sequestering heavy metals. Namely, these nanostructure surfaces could be entirely coated with moieties capable of heavy metal remediation by presenting a hydrophilic chelator on every molecule. Realizing this design rationale requires the suppression of amphiphile exchange to minimize the rearrangement and release of amphiphile molecules from their assembled structures into the solvent space. Suppression of these exchange dynamics may also reduce the sensitivity of the assembly to variations in its environment such and temperature and pH.[27]

The removal of lead ions, Pb^{2+}, from drinking water is a critical target. Inorganic lead is a potent toxin which can damage nearly all organs, with adverse health effects including neurotoxicity, cardiovascular complications, cancer, and death.[220, 221] Lead enters drinking water from a variety of sources, including the production and disposal of lead-acid batteries, alloy manufacturing, and, particularly, the erosion of plumbing.[222-224] Lead contamination crises persist globally, and increasing research indicates these

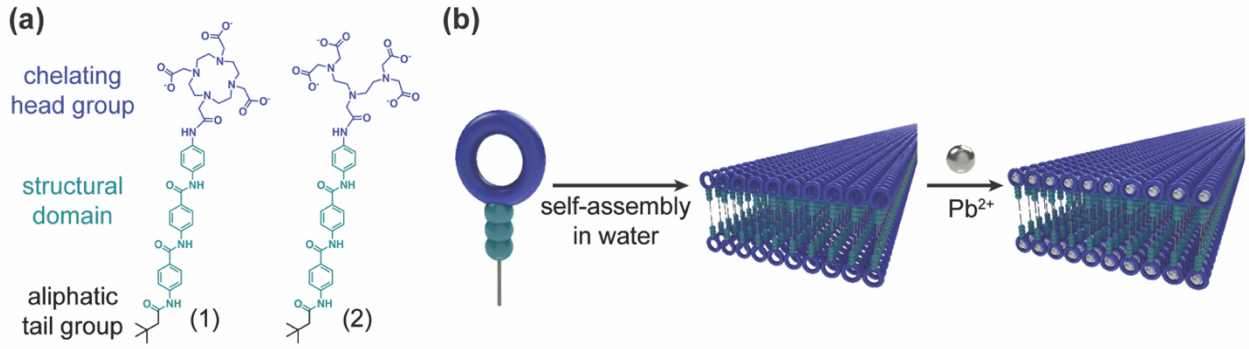

Figure 5.1 l Aramid amphiphiles with a heavy metal chelating head group self-assemble into nanoribbons for the remediation of lead from contaminated water. (a) Aramid amphiphiles contain an aliphatic, nonpolar tail group (black) and hydrophilic head group (purple) to induce self-assembly via the hydrophobic effect. A structural domain (turquoise) imparts structural stability to the assembled nanostructure. To chelate Pb^{2+} from water, head groups are selected with a DOTA (compound **1**) or DTPA (compound **2**) moiety. (b) Aramid amphiphiles spontaneously self-assemble upon the addition of water to form Pb^{2+}-chelating nanoribbons.

events disproportionately occur in the United States along racial and socioeconomic lines.[63, 225-227] Thus, there exists an urgent need to develop contemporary strategies for point-of-use remediation of lead from drinking water streams.

Here, we present the design of small molecule amphiphiles which exhibit three characteristics for the remediation of lead from contaminated water (Figure 5.1): (1) amphiphilicity to induce spontaneous self-assembly in water into high surface area nanostructures; (2) a structural domain to provide intermolecular cohesion and promote their assembly into long nanostructures that may be further aligned or entangled; and (3) a chelating head group capable of strongly binding to heavy metal cations in solution. To accomplish these goals, we use the aramid amphiphile (AA) motif as the platform for molecular self-assembly.[51] AAs take advantage of a dense hydrogen bonding network to impart structural stability on assembled nanoribbons with surface areas on the order of 200 m^2/g. Of particular note for this application, the amphiphiles exhibit suppressed exchange dynamics upon assembly, hindering the release of amphiphiles from their nanostructure. The supressed exchange dynamics differentiate this self-assembly approach from those that have been previously explored for water treatment.[228, 229] In previous reports, heavy metal cations initiate physical crosslinking that induces

hydrogelation – a process that may impede surface chelation events by limiting diffusion to the inside of the gel.[53] This design presents advantages over other soft materials systems, including polymers and polymer networks, because: (1) all chemical groups are expressed on the nanostructure surfaces, and are thermodynamically prohibited from being buried within a material; (2) surface chemistries and functionalities can be readily tuned through careful selection of the hydrophilic head group, enabling tuning of heavy metal remediation effectiveness and selectivity; and (3) the chemical character of the chelating compounds is minimally impacted by requiring only one covalent tether to the nanostructure surface, maximizing ionic interactions with dissolved lead species.

Results and Discussion

We designed and synthesized two AAs for the remediation of heavy metals from drinking water: compound **1**, an AA with a DOTA (dodecane tetraacetic acid; also known as tetraxetan) head group, and compound **2**, an AA with a DTPA (diethylenetriaminepentaacetic acid; also known as pentetic acid) head group (Figure 5.1a). These groups were selected for their high binding affinity to lead ions in solution and their capability of inducing amphiphilic self-assembly by providing sufficient head group hydrophilicity (Figure 5.1b). Both AAs with DOTA and DTPA head groups harness ionic interactions from charged carboxylic acid moieties and dipole interactions from tertiary amines to sequester lead ions from water.[230, 231] Compounds **1** and **2** were obtained by alternating carbodiimide-mediated amidation reactions and standard deprotection reactions. Synthetic details and characterization of the final compounds and their intermediates are provided in the Methods section.

We observe the spontaneous assembly of both compounds **1** and **2** in water into nanoribbons with lengths extending at least several microns (Figures 5.2a and 5.2c) by transmission electron microscopy (TEM). To ascertain cross-sectional dimensions, we use cryogenic TEM (Cryo-TEM) to obtain high-resolution images of the nanoribbons in a

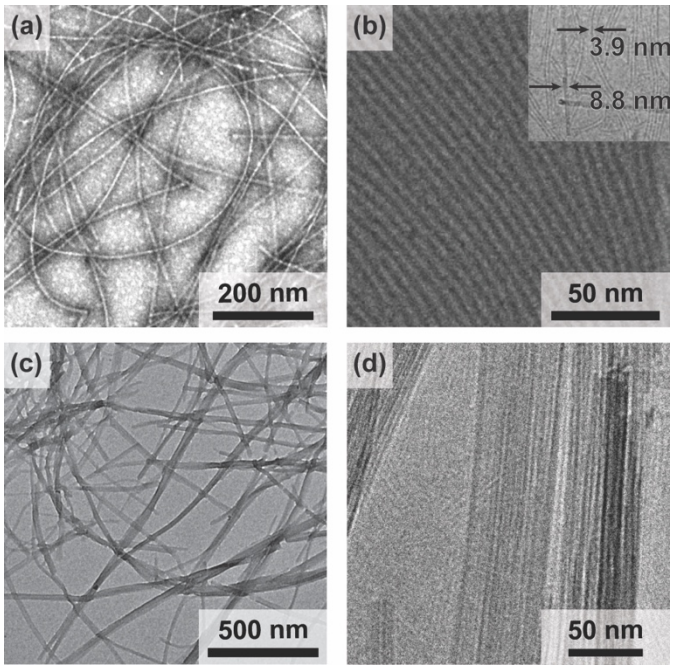

Figure 5.2 l Compounds **1** and **2** self-assemble into high aspect ratio nanoribbons in water. **a**, Conventional TEM of **1** illustrates its assembly into microns-long nanoribbons. **b**, Cryogenic TEM of **1** reveals a 3.9 nm x 8.8 nm nanoribbon cross-section (inset). **c**, Conventional TEM of **2** shows bundling of microns-long nanoribbons. **d**, Cryogenic TEM of **2** nanoribbons identifies a 3.9 x 5.1 nm cross-section.

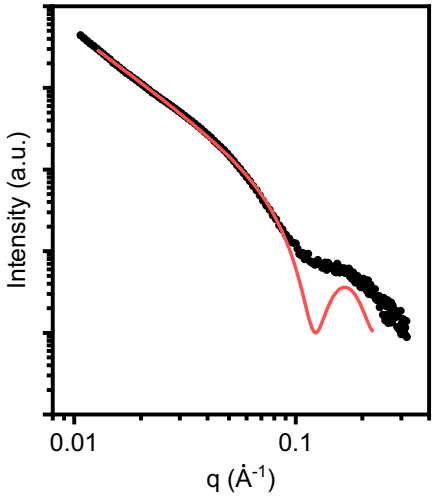

Figure 5.3 l SAXS of an aqueous suspension of compound **1** nanoribbons is fit to a lamellar model (red), which returns a 3.9 nm nanoribbon thickness.

solvated state and synchrotron small angle X-ray scattering (SAXS) for nanostructure characterization. From these techniques, we find a 3.9 nm thickness and 8.8 nm width for compound **1,** and a 3.9 nm thickness by 5.1 nm width for compound **2** (Figures 5.2b, 5.2d, and 5.3). These dimensions give rise to surfaces areas on the order of 200 m^2/g.[51]

Having identified the geometries of the self-assembled nanostructures, we use a variety of techniques to characterize the chelation performance of compound **1** nanoribbons. Ultraviolet-visible (UV-Vis) absorption spectroscopy allows us to observe the formation of the DOTA and lead complex.[232] An absorption peak at λ = 262 nm, characteristic of this complex, emerges as lead ions are titrated into a solution of compound **1** nanoribbons (Figure 5.4a). The rise of this peak plateaus at 50 mol% Pb^{2+}, most likely signifying a 2:1 complexation of DOTA to the lead ions. This sandwich-type complex has been previously observed in similar systems where cyclic chelating moieties are maintained in close proximity.[233]

We employ isothermal titration calorimetry (ITC) to quantify thermodynamic parameters of the lead-binding surface reaction (Figure 5.4b). This experiment captures the heat released from the injection of a concentrated lead solution into a dilute nanoribbon suspension. Injection of the concentrated lead solution into nanoribbon-free water is background-subtracted from these data to remove the heat of dilution. Negligible signal is detected by the injection of water into the nanoribbon suspension. From fitting sigmoidal curves to n = 3 runs, we calculate an equilibrium binding constant $K_b = 2.2 \pm 0.5 \times 10^5$ M^{-1}. This value indicates an equilibrium which strongly prefers the binding of lead ions to the nanoribbon surfaces, rather than the presence of lead ions free in solution, and suggests that the nanoribbons are successful in remediating the heavy metal from contaminated water. This equilibrium constant further suggests that compound **1** nanoribbons should be used in significant excess to the lead present in contaminated water to thermodynamically drive remediation below the 15 ppb regulatory level for toxicity.[220] We further observe the plateau of chelation signal at n = 0.5, corroborating the saturation of the nanoribbons at 50 mol% Pb, and that the nanoribbons maintain their morphology after lead chelation (Figure 5.5).

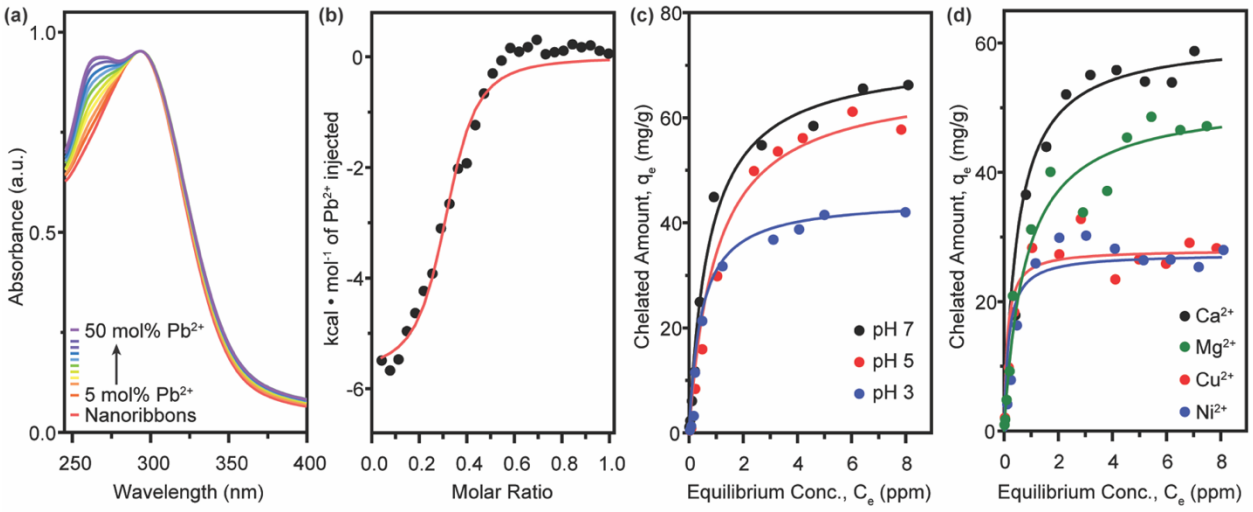

Figure 5.4 l Compound **1** nanoribbons remediate Pb^{2+} from water, exhibiting sensitivity to pH and the presence of competing divalent cations. **a**, UV-Vis absorption spectra show the appearance of a peak at $\lambda = 262$ nm, corresponding to the binding of Pb^{2+} to compound **1** nanoribbon DOTA groups. This peak intensity plateaus at 50 mol% Pb^{2+}, indicating a 2:1 amphiphile:Pb^{2+} stoichiometry of binding. **b**, ITC reveals an equilibrium binding constant $K_b = 2.2 \pm 0.5 \times 10^5$ M^{-1} of Pb^{2+} to compound **1** nanoribbons, while further corroborating a 2:1 amphiphile:Pb^{2+} stoichiometry. **c**, Adsorption isotherms illustrate a drop in equilibrium Pb^{2+} saturation on the nanoribbons from $Q_o = 72$ mg/g at pH 7, to $Q_o = 61$ mg/g at pH 5, to $Q_o = 45$ mg/g at pH 3. **d**, Adsorption isotherms with equimolar amounts of Pb^{2+} and either Ca^{2+}, Mg^{2+}, Cu^{2+}, or Ni^{2+} demonstrate lead saturation capacities of 61, 52, 32, and 27 mg/g, respectively.

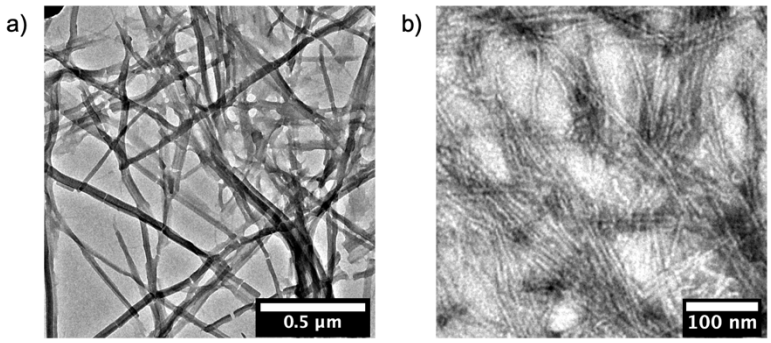

Figure 5.5 l Compound **1** and **2** nanoribbons maintain their morphology through (a) Compound **1** and (b) compound **2** nanoribbons after the chelation of lead.

We hypothesize that the remediation capacity of lead ions by AA nanoribbons should be affected by pH, as protonation of the nanoribbon head groups would hinder ionic interactions between the chelating moieties and lead ions.[234] Because lead species become insoluble in basic environments[235], we selected pH values of 7, 5, and 3 to test remediation capacity. We observe no change in assembly morphology of compound **1** nanoribbons when the pH is adjusted to 3 post-assembly (Figure 5.6), likely because of the stability imparted to the structure by the aramid domain.

Adsorption isotherm curves are constructed for the uptake of lead by compound **1** nanoribbons to test pH sensitivity (Figure 5.4c). Nanoribbons are mixed with Pb^{2+} 24 h before testing to ensure equilibrium is reached. Equilibrium data are fit to a Langmuir model, with R^2 values exceeding 0.97 in all cases (Figure 5.7). Compound **1** nanoribbons demonstrate adsorption capacities (Q_o) of 72, 61, and 45 mg/g at pH values of 7, 5, and 3, respectively. As predicted, the lead chelation capacity drops slightly when changing from pH 7 to 5, and drops significantly at pH 3.

We further expect that the nanoribbons' lead adsorption capacities may be sensitive to the presence of other multivalent cations which could compete with lead to occupy the chelation complex. To test this hypothesis, we constructed adsorption isotherms with equimolar amounts of lead and either calcium, copper, magnesium, or nickel ions (Figure 5.4d). Fits of the equilibrium data to a Langmuir model (Figure 5.8) are used to extract lead adsorption capacities in the equimolar presence of each ion: for Ca^{2+}, $Q_{o,Pb^{2+}}$ = 61 mg/g; for Mg^{2+}, $Q_{o,Pb^{2+}}$ = 52 mg/g; for Cu^{2+}, $Q_{o,Pb^{2+}}$ = 32 mg/g; and for Ni^{2+}, $Q_{o,Pb^{2+}}$ = 27 mg/g. Thus, from least to most interference with Pb^{2+} binding to compound **1** nanoribbons, we observe the following trend: $Ca^{2+} < Mg^{2+} << Cu^{2+}$, Ni^{2+}. This trend largely follows the equilibrium binding constants of the ions to the free DOTA molecule in solution.[236] To put this data in perspective, remediating 1 L of water with 50 ppb Pb to below 15 ppb Pb at pH 7 requires approximately 690 µg of compound **1** nanoribbons in the absence of competing counterions, and 820, 960, 1560, and 1850 µg compound **1** nanoribbons in the presence of equimolar amounts of Pb^{2+} and Ca^{2+}, Mg^{2+}, Cu^{2+}, and Ni^{2+}, respectively. These results confirm that the lead-binding capacity of compound **1**

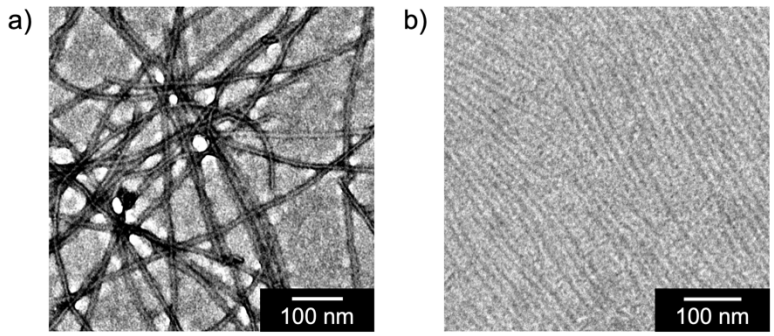

Figure 5.6 l a, Compound **1** and **b**, compound **2** nanoribbons retain their morphology after adjustment of the aqueous environment to pH 3.

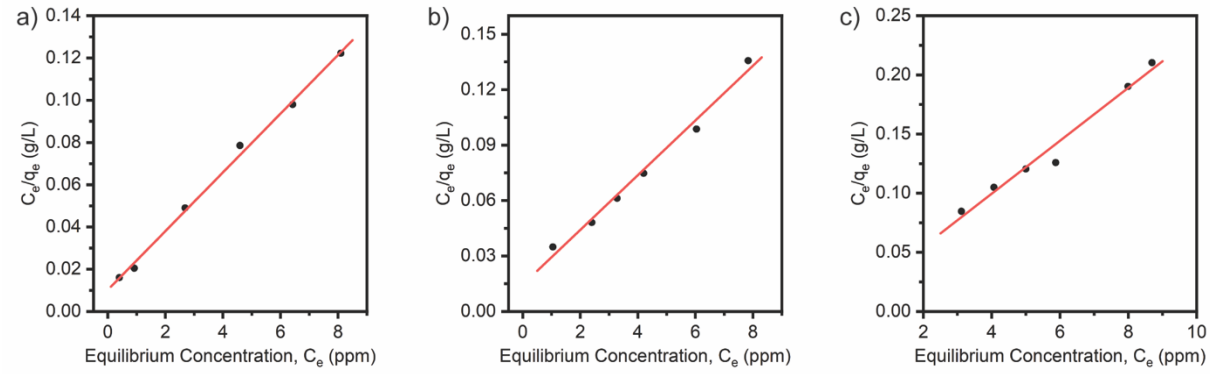

Figure 5.7 l Linear regression of pH-dependent lead adsorption for compound **1** obtained by fitting equilibrium data to a Langmuir adsorption model. The fittings shown here are for **a**, pH 7; **b**, pH 5; and **c**, pH 3.

nanoribbons is reduced by the presence of competing multivalent cations and suggests that this system may be used to simultaneously remove several contaminants from polluted water.

The capacity of amphiphilic nanoribbons to remediate heavy metal ions from water should be sensitive to the geometry and chemical structure of the head group. [234] Lead ions likely percolate into the head group domain of compound **1** to sandwich between neighbouring DOTA head groups. Conversely, the DTPA head group of compound **2** is prone to facing outwards from the nanoribbon core due to steric hinderance and has four carboxylic acids per molecule available for complexation. Therefore, we expect

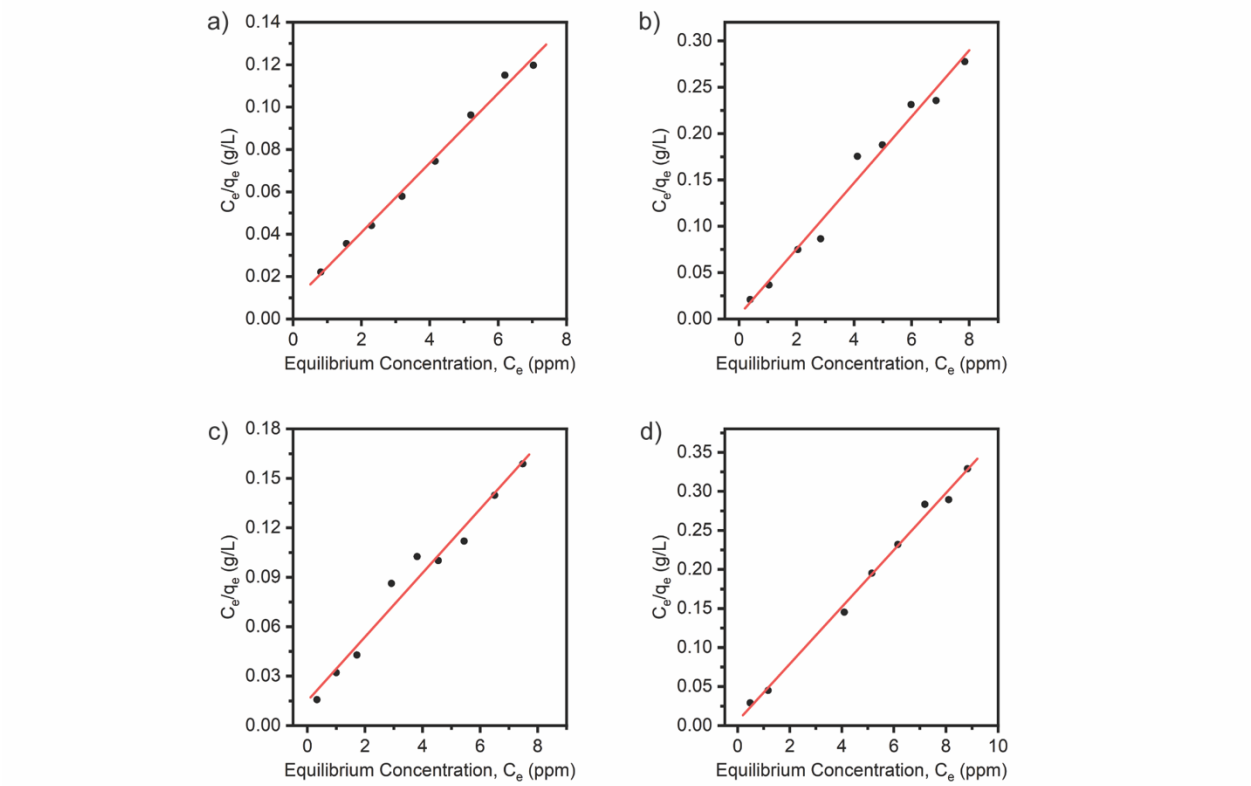

Figure 5.8 l Linear regression of competing counterion lead adsorption for compound **1** obtained by fitting equilibrium data to a Langmuir adsorption model. The fittings shown here are for Pb^{2+} adsorption when present in equimolar quantities with **a**, Ca^{2+}; **b**, Cu^{2+}; **c**, Mg^{2+}; and **d**, Ni^{2+}.

compound **2** nanoribbons to exhibit more effectively sequester Pb^{2+} from water than those of compound **1**.

The formation of a lead:amphiphile chelation complex on compound **2** nanoribbons is monitored by UV-Vis absorption spectroscopy with the emergence of a peak at 255 nm (Figure 5.9a). We observe that compound **2** nanoribbons maintain their morphology with chelation (Figure 5.5) and, interestingly, find compound **2** nanoribbon chelators saturate near 50 mol% Pb. This effect may result from hydrogen bonding between head groups, which leads to the bundling of nanoribbons (Figure 5.2c-d), reducing the effective accessible surface area. Compound **2** nanoribbons exhibit an equilibrium binding constant of K_b = 7.1 ± 1.6 x 10^5 M^{-1} in n = 3 background-subtracted ITC experiments (Figure 5.9b). This binding constant is statistically significantly higher than that of compound **1**, and predicts that compound **2** nanoribbons should thus exhibit enhanced

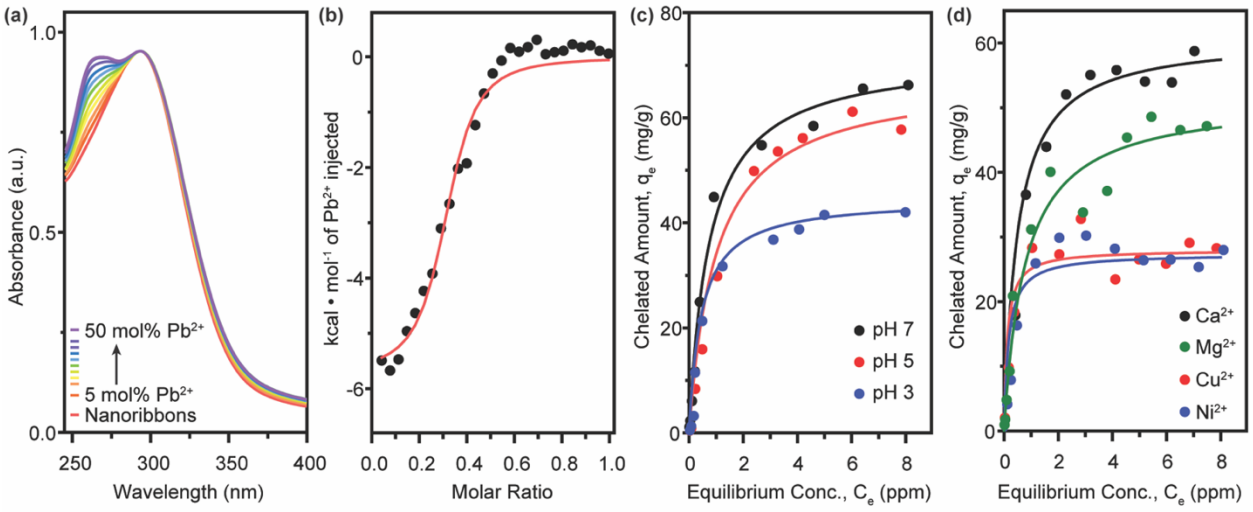

Figure 5.9 I Compound **1** nanoribbons remediate Pb^{2+} from water, exhibiting sensitivity to pH and the presence of competing divalent cations. **a**, UV-Vis absorption spectra show the appearance of a peak at $\lambda = 262$ nm, corresponding to the binding of Pb^{2+} to compound **1** nanoribbon DOTA groups. This peak intensity plateaus at 50 mol% Pb^{2+}, indicating a 2:1 amphiphile:Pb^{2+} stoichiometry of binding. **b**, ITC reveals an equilibrium binding constant $K_b = 2.2 \pm 0.5 \times 10^5$ M^{-1} of Pb^{2+} to compound **1** nanoribbons, while further corroborating a 2:1 amphiphile:Pb^{2+} stoichiometry. **c**, Adsorption isotherms illustrate a drop in equilibrium Pb^{2+} saturation on the nanoribbons from $Q_o = 72$ mg/g at pH 7, to $Q_o = 61$ mg/g at pH 5, to $Q_o = 45$ mg/g at pH 3. **d**, Adsorption isotherms with equimolar amounts of Pb^{2+} and either Ca^{2+}, Mg^{2+}, Cu^{2+}, or Ni^{2+} demonstrate lead saturation capacities of 61, 52, 32, and 27 mg/g, respectively.

lead-binding in adsorption isotherm experiments. As with compound **1** nanoribbons, this equilibrium constant also implies that achieving lead remediation below 15 ppb requires using a significant excess of compound **2** nanoribbons relative to the lead present in the water.[220]

As with compound **1**, the remediation capacity of compound **2** nanoribbons is expected to be sensitive to pH as head group protonation inhibits ionic interactions with lead ions (Figure 5.9c, Figure 5.10). Compound **2** nanoribbons are also demonstrated to maintain their nanostructure upon environmental adjustment to pH 3 (Figure 5.6). At pH 7, compound **2** nanoribbons have an equilibrium saturation capacity of $Q_o = 96$ mg/g. This saturation capacity drops slightly to $Q_o = 93$ mg/g at pH 5, and further declines to $Q_o = 81$ mg/g at pH 3, following the expected trend and matching the pattern of compound **1**. Notably, the saturation capacity of compound **2** nanoribbons is higher than those of **1** across all pH values. This result, in conjunction with the elevated thermodynamic

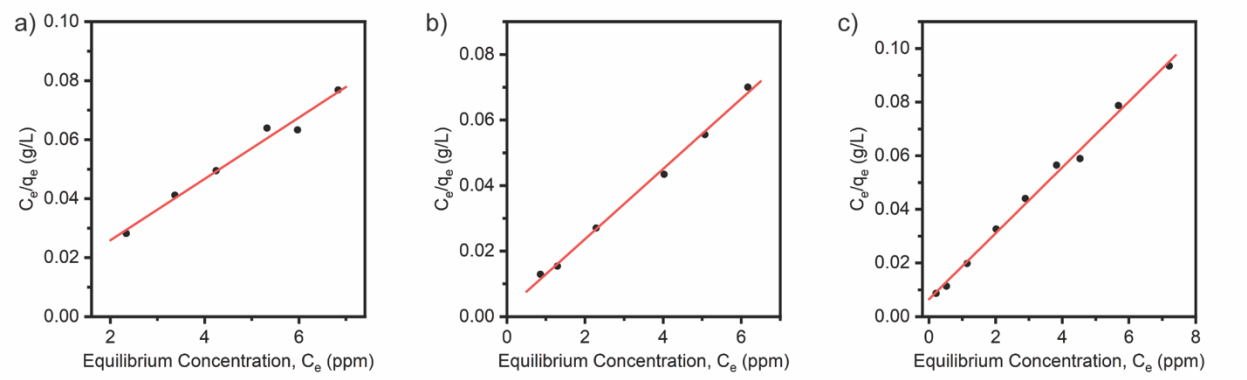

Figure 5.10 l Linear regression of pH-dependent lead adsorption for compound **2** obtained by fitting equilibrium data to a Langmuir adsorption model. The fittings shown here are for **a**, pH 7; **b**, pH 5; and **c**, pH 3.

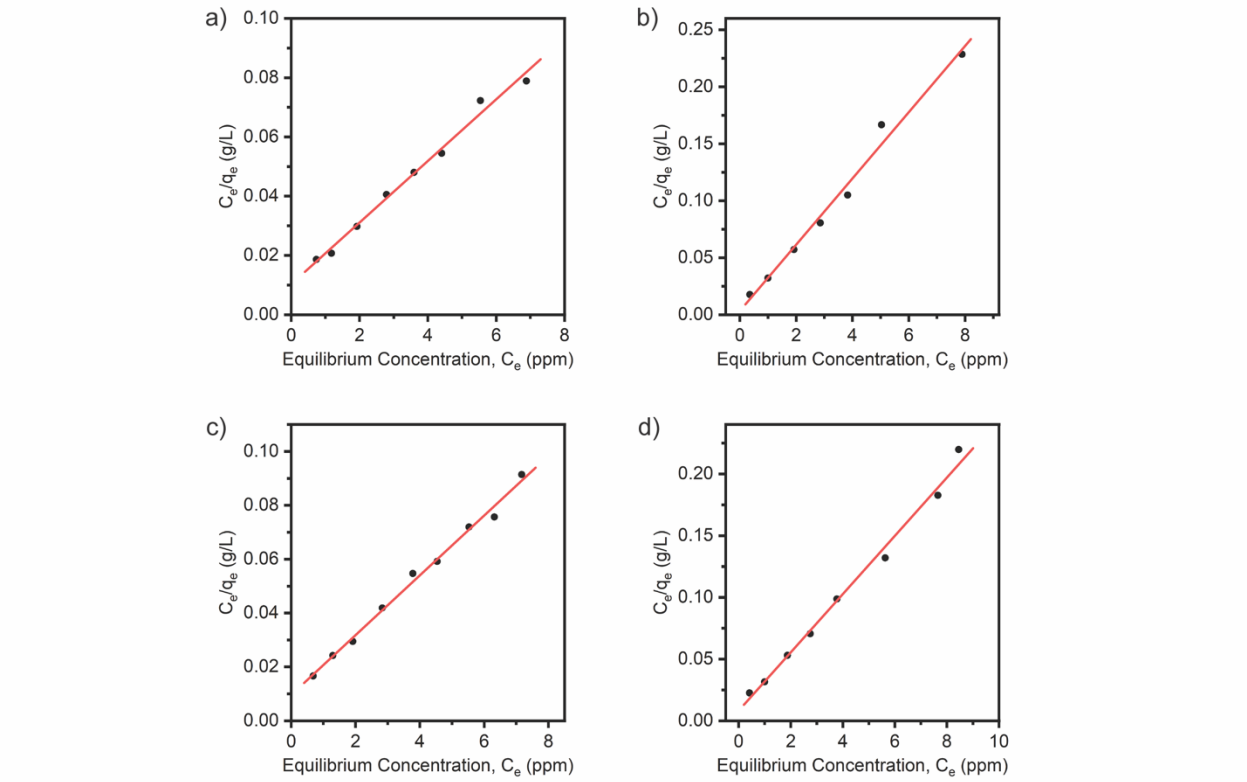

Figure 5.11 l Linear regression of competing counterion lead adsorption for compound **2** obtained by fitting equilibrium data to a Langmuir adsorption model. The fittings shown here are for Pb^{2+} adsorption when present in equimolar quantities with **a**, Ca^{2+}; **b**, Cu^{2+}; **c**, Mg^{2+}; and **d**, Ni^{2+}.

equilibrium binding constant of **2** nanoribbons, confirms that head group choice is a viable parameter for tuning chelation capacity of small molecule amphiphilic nanoribbons.

The saturation capacities of the nanoribbon materials presented here match or exceed those of functional materials investigated or in use today for lead remediation. For example, the equilibrium saturation capacities of compound **1** and **2** nanoribbons exceed that of activated carbon (50 mg/g)[237], sulfur-functionalized silica (46 mg/g)[238], acidified carbon nanotubes (17 mg/g)[239], and apricot stone (21 mg/g).[240] In contrast, compound **1** and **2** nanoribbons offer comparable performance to Fe(III)-modified zeolite (99 mg/g)[241] and iron oxide nanomaterials (98 mg/g).[242]

Finally, we sought to identify the effect of competitive binding for chelation sites by divalent cations on compound **2** nanoribbons. We again performed adsorption isotherm experiments with equimolar amounts of lead and either calcium, copper, magnesium, or nickel ions (Figure 5.9d, 5.11). For compound **2** nanoribbons, we find for Ca^{2+}, $Q_{o,Pb^{2+}}$ = 96 mg/g; for Mg^{2+}, $Q_{o,Pb^{2+}}$ = 90 mg/g; for Ni^{2+}, $Q_{o,Pb^{2+}}$ = 42 mg/g; and for Cu^{2+}, $Q_{o,Pb^{2+}}$ = 34 mg/g. From least to most interference with Pb^{2+} binding to **2** nanoribbons, we observe: $Ca^{2+} < Mg^{2+} << Ni^{2+} < Cu^{2+}$. These results indicate that remediating 1 L of water with 50 ppb Pb to below 15 ppb Pb at pH 7 requires approximately 520 µg of compound **2** nanoribbons in the absence of competing counterions, and 520, 560, 1190, and 1470 µg compound **2** nanoribbons in the presence of equimolar amounts of Pb^{2+} and Ca^{2+}, Mg^{2+}, Ni^{2+}, and Cu^{2+}, respectively. This trend generally follows that of equilibrium binding constants for these ions to free DTPA in solution.[236] Fractionally and in total saturation magnitude, compound **2** is affected less by competitive binding with these cations than compound **1**, with the exception of copper(II). This result suggests that head group choice can be used not only to improve adsorption capacity, but also to tune ion selectivity.

Here, we presented two aramid amphiphile (AA) molecules to spontaneously self-assemble in water, forming high-aspect-ratio nanoribbons, for the remediation of lead from contaminated water. Both AAs produced microns-long nanoribbons upon assembly with 4 nm x 5-9 nm cross-sections and surface areas on the order of hundreds of m^2/g. All nanoribbons exhibited the capacity to capture Pb^{2+} with a 2:1 chelator:lead stoichiometry. Nanoribbons coated with a surface of DTPA chelators expressed a higher

thermodynamic binding constant to lead than those with a DOTA surface, giving rise to higher equilibrium lead saturation capacities. The lead-binding capacity of the supramolecular nanoribbons was sensitive to pH, dropping as the head groups became protonated with decreasing pH. The lead-binding efficacy of the nanoribbons was also impacted by the presence of other divalent cations which compete for chelation sites. This result indicates that AA nanoribbons may be used for the synergistic removal of multiple contaminants. Amphiphile head group choice was also identified as a parameter for optimizing binding efficacy and ion selectivity. The small molecule self-assembly strategy described here offers a paradigm for remediating contaminants from water that takes advantage of the high surface areas, tunable chemistries, and scalability of supramolecular nanostructures.

Methods

Synthesis and chemical characterization

Methyl 4-aminobenzoate (Sigma Aldrich, 98%), 3,3-dimethylbutyric acid (Sigma Aldrich, 98%), *N*-Boc-*p*-phenylenediamine (BPP, Sigma Aldrich, 97%), diethylenetriamine-*N,N,N″,N″*-tetra-*tert*-butyl acetate-*N′*-acetic acid (DTPA-tetra(t-Bu ester), Combi Blocks, 95%), 1-ethyl-3-(3-dimethylaminopropyl)carbodiimide hydrochloride (EDC, TCI Chemicals, 98%), 4-dimethylaminopyridine (DMAP, TCI Chemicals, 99%), 1-hydroxybenzotriazole hydrate (HOBt, TCI Chemicals, 97%), lithium hydroxide (LiOH, Alfa Aesar, 98%), sodium bicarbonate ($NaHCO_3$, Alfa Aesar, 99%), hydrochloric acid (HCl, Alfa Aesar, 36%), trifluoroacetic acid (TFA, Alfa Aesar, 99%), and 2-(4,7,10-tris(2-tert-butoxy-2-oxoethyl)-1,4,7,10-tetraazacyclododecan-1-yl)acetic acid (DOTA-tris(t-Bu ester), AstaTech, 95%), were used as received without further purification.

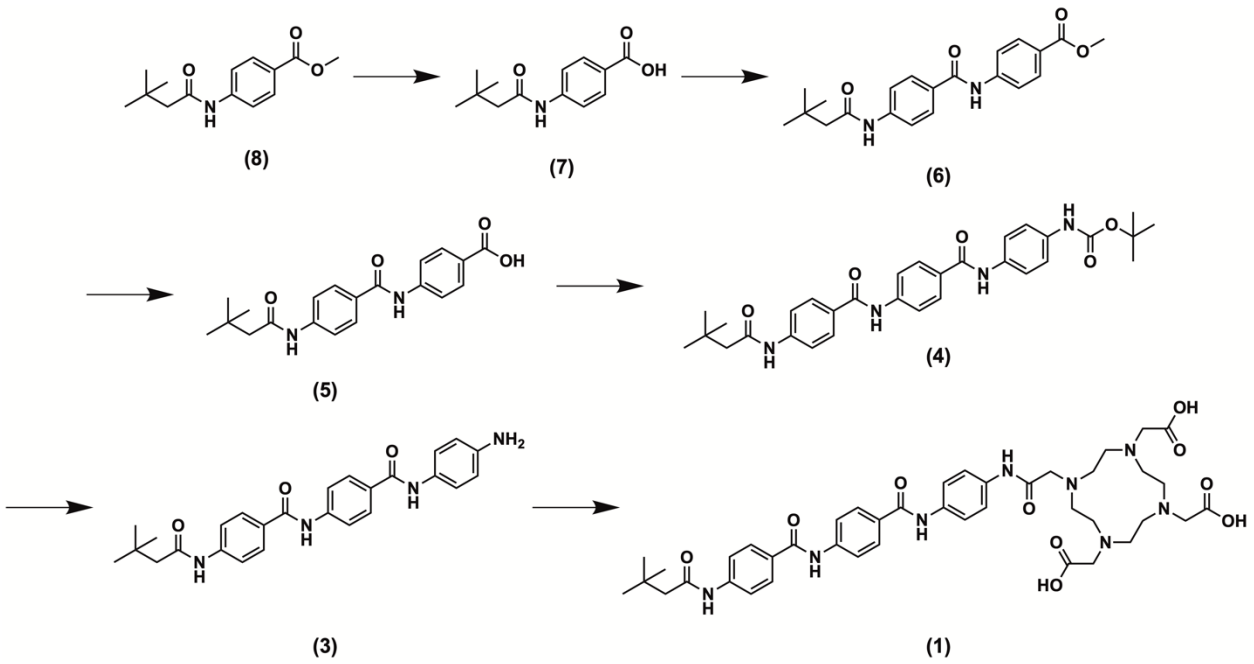

Scheme 5.1 I Synthesis scheme to obtain the tetraxeten amphiphile.

Compound **3** was prepared as previously described.[25] For reference, we briefly outline the synthesis details to obtain this compound below:

Methyl 4-(3,3-dimethylbutanamido)benzoate (**8**): We mix a solution of methyl 4-aminobenzoate (11.01 mmol), 3,3-dimethylbutyric acid (16.52 mmol), EDC (33.03 mmol), and DMAP (33.03 mmol) in tetrahydrofuran (50 mL) for 24 h at room temperature. To obtain the final compound, the solvent was removed in vacuum, and the residue was washed with deionized water and extracted in chloroform. The final product was obtained by performing column chromotagraphy of the organic layer using silica gel and 1:1 ethyl acetate:hexane by volume (yield: 72%).

4-(3,3-dimethylbutanamido)benzoic acid (**7**): A mixture of 10 M LiOH (10 mL) and compound **8** (4.25 mmol) in ethanol (40 mL) was heated to 60°C and refluxed for 3 h, and then neutralized using an aqueous HCl solution. The precipitate was obtained by filtration and washed with water several times, and the resulting crude product was purified by reprecipitation from chloroform and methanol (yield: 98%).

Methyl 4-(4-(3,3-dimethylbutanamido)benzamido)benzoate (**6**): A mixture of EDC (6.37 mmol), DMAP (6.37 mmol), compound **7** (2.13 mmol), and methyl 4-aminobenzoate

(6.37 mmol) in dimethylformamide (30 mL) was stirred for 24 h at 50 °C. To obtain the final product, the solvent was removed in vacuum and the remaining residue was precipitated in water. The crude mixture was collected by filtration, washed with excess methanol, and dried (yield: 83%).

4-(4-(3,3-dimethylbutanamido)benzamido)benzoic acid (**5**): A mixture of 10M LiOH (10 mL) and compound **6** (2.55 mmol) in tetrahydrofuran (20 mL) and ethanol (10 mL) was refluxed for 6 h and then neutralized with an aqueous HCl solution. To obtain the final product, the precipitate was filtered off, washed with water, and dried (yield: 98%).

tert-Butyl 4-(4-(4-(3,3-dimethylbutanamido)benzamido)benzamido)phenylcarbamate (**4**): A solution of compound **5** (0.85 mmol), BPP (2.55 mmol), EDC (2.55 mmol), and DMAP (2.55 mmol) in dimethylformamide (20 mL) was stirred at room temperature for 24 h. To obtain the final product, the solvent was evaporated, and then the crude mixture was washed with water and methanol (yield: 81%).

N-(4-(amino)phenyl)-4-(4-(3,3-dimethylbutanamido)benzamido)benzamide (**3**): A solution of TFA (500 µL) added dropwise into compound **4** (0.55 mmol) suspended in in methylene chloride (15 mL) was mixed for 6 h at room temperature. To obtain the final product, the volatile fraction was distilled off, the remaining mixture was washed with saturated $NaHCO_3$ solution, and the solid precipitate was filtered and dried (yield: 99%).

Synthesis of 2,2',2''-(10-(2-((4-(4-(4-(3,3-dimethylbutanamido)benzamido) benzamido)phenyl)amino)-2-oxoethyl)-1,4,7,10-tetraazacyclododecane-1,4,7-triyl)triacetic acid (**1**): A solution of **3** (1.35 mmol), DOTA-tris(t-Bu ester) (1.62 mmol), EDC (4.05 mmol), and DMAP (4.05 mmol) in dimethylformamide (20 mL) was stirred at 60 °C for 24 h. After the reaction, the solvent was removed *in vacuo*. The residue was suspended in deionized water and filtered to obtain a light-yellow precipitate. The isolated compound was then reacted with TFA (8 mL) in chloroform (20 mL) for 17 h. The volatile fraction was evaporated under reduced pressure. The remaining residue was suspended in ethyl acetate and filtered to obtain compound **1** by filtration (yield: 43%). ^{1}H NMR (400 MHz, Bruker Avance III DPX 400, DMSO-*d*): 7.95 (m, 8H), 7.75 (t, 4H), 7.57 (d, 2H), 4.04 (m, 1H), 3.88 (s, 6H), 3.74 (s, 3H), 3.63 (s, 1H), 2.7 (m, 4H) , 2.25 (s, 2H), 2.00 (s, 1H), 1.91

(s, 1H), 1.17 (m, 2H), 1.05 (s, 9H) ppm. MS (MALDI-ToF) $[M + H]^+$ m/z calculated: 831.40; $[M + H]^+$ found: 831.41.

Compound **2** was prepared as previously described.[25] For reference, we briefly outline the synthesis details to obtain this compound below:

2,2',2'',2'''-((((2-((4-(4-(4-(3,3-dimethylbutanamido)benzamido)benzamido)phenyl) amino)-2-ox-oethyl)azanediyl)bis(ethane-2,1-diyl))bis(azanetriyl))tetraacetate (**2**): A solution of compound **3** (0.29 mmol), EDC (1.17 mmol), DMAP (1.17 mmol), and DTPA-tetra(t-Bu ester) (0.58 mmol) in dimethylformamide (20 mL) was stirred at 50 °C for 72 h. After the reaction, the solvent was removed in vacuum and the remaining residue was purified by flash column chromatography using silica gel and 7:1 tetrahydrofuran:chloroform (by volume). The resulting compound was mixed with TFA (500 µL) and methylene chloride (15 mL) for 48 h. To obtain the final product, the volatile fraction was removed by vacuum, and tetrahydrofuran was added to suspend the product, which was collected by filtration and dried (yield: 67%).

Mass spectrometry

The molecular weight of **1** was determined using a Bruker Omniflex matrix assisted laser desorption/ionization-time-of-flight (MALDI-ToF) instrument with a Reflectron accessory. The matrix solution used α-cyano-4-hydroxycinnamic acid in 50:50:0.1 water:acetonitrile:TFA by volume. SpheriCal Peptide Low (Polymer Factory) was added to the MALDI-ToF solution as an internal calibrant.

Sample preparation

Nanoribbon suspensions were prepared by dissolving compounds **1** and **2** in deionized water and sonicating for ten minutes in a bath sonicator. Lead solutions were prepared by dissolving lead (II) nitrate (99.999% trace metals basis, Sigma-Aldrich) in deionized water. The concentrations of lead stock solutions were verified by ICP-MS.

Transmission electron microscopy (TEM)

Self-assembled nanostructures were observed by TEM using a FEI Tecnai G2 Spirit TWIN microscope at a 120 kV accelerating voltage. TEM grids were prepared by depositing 7.0 μL of a 1 mg/mL amphiphile solution onto a continuous carbon grid (Electron Microscopy Sciences, 200 mesh, copper) for 30 sec, blotting to remove the solution, depositing 7.0 μL of a 1% phosphotungstic acid aqueous solution (Electron Microscopy Sciences) onto the grid, and blotting to remove the stain.

Cryogenic transmission electron microscopy (Cryo-TEM)

Cryo-TEM images were captured on a Talos Arctica G2 Cryo-TEM at a 200 kV accelerating voltage. Grids were prepared with an FEI Vitrobot Mark IV. To prepare a sample for analysis, 3.0 μL of a 1.0 mg/mL nanoribbon solution was pipetted onto a glow-discharged holey carbon grid (Ted Pella, 300 mesh, copper) in a chamber set to 100% humidity. The grids were blotted for 4 sec and then immediately plunged into liquid ethane and subsequently retained in liquid nitrogen.

Small angle X-Ray scattering (SAXS)

SAXS profiles of aqueous nanoribbon solutions were captured at Beamline 12-ID-B of the Advanced Photon Source at Argonne National Laboratory using a 13.3 keV X-Ray radiation energy and DECTRIS PILATUS 300K detector. Solutions were loaded into 2 mm diameter quartz capillary tubes (Hampton Research) for analysis. Reported SAXS profiles were background subtracted using beamline software to subtract water and capillary background.

Ultraviolet-visible (UV-Vis) spectroscopy

UV-Vis absorbance profiles of aqueous amphiphile solutions with variable Pb^{2+} concentrations were captured on a PerkinElmer LAMBDA 850+ UV/Vis spectrophotometer. The amphiphile concentration was fixed at 0.05 mM.

Isothermal titration calorimetry (ITC)

Binding isotherms were captured on a Microcal VP-ITC ultrasensitive titration calorimeter. A 3.0 mM lead nitrate aqueous solution was injected into 0.3 mM nanoribbon solutions prepared from the same deionized water source. A buffer was not used due to the insolubility of lead species in most buffers. The ITC was run with 5 μL injection intervals over 10 seconds in five minute intervals at 25 ºC. Titrations were carried out three times to ensure consistency and reproducibility. Data analysis was conducted using instrument software.

Adsorption isotherms

Lead concentrations used to construct adsorption isotherms were analyzed on an Agilent 7900 inductively coupled plasma-mass spectrometer (ICP-MS). Concentration calibration curves were constructed using a 1 ppm lead ICP-MS stock solution from Ricca Chemical. Internal calibration for each sample used a 10 ppm rhodium ICP-MS stock solution from Sigma-Aldrich. Calcium chloride, copper chloride, magnesium sulfate, and nickel chloride salts were obtained from Sigma-Aldrich. Adsorption isotherm solutions were mixed for 24 h before analysis. After 24 h, the solutions were centrifuged for 5 min. at 10,000 rcf and the supernatant was retained for testing.

Chapter 6

Interfacial dynamics dictate the performance of surface-mediated binding on supramolecular nanostructures

Abstract: The dynamic behavior of biological materials is precisely controlled in nature to imbue biological functionality, suggesting that harnessing interfacial dynamics could enhance the performance of materials whose applications are dictated by surface-mediated events. Here, we investigate the influence of surface flexibility and hydration on heavy metal remediation by supramolecular nanostructures. We find that incorporating short oligo-ethylene glycol spacers below the surfaces of these systems can drastically increase the diffusion rate of remediating moieties while interacting with surrounding water. In turn, we find the binding affinities of the most flexible surfaces for Pb^{2+} are over an order of magnitude higher than less flexible surfaces, enabling the remediation of thousands of liters of Pb^{2+}-contaminated water with single grams of material. These findings establish nanoscale dynamics as a critical design factor for soft matter systems where interfacial interactions are essential to material function.

Introduction

The dynamics of soft matter systems play a critical role in enabling molecular recognition and binding events.[243, 244] For example, the dynamics of protein relaxation and fluctuation events control their ability to bind ligands.[245, 246] These findings have replaced the static "lock-and-key" models for protein binding events with more complete representations, such as the induced fit[246] and conformational selection models.[247] As a result, the influence of flexibility – a critical design parameter for controlling soft matter dynamics – on the binding affinities of biological systems is now considered a "fundamental determinant of intermolecular interaction strength."[243] Despite progress in the past few decades in uncovering dynamics-function relationships in biological systems,[248] designing for molecular flexibility is largely overlooked on the surfaces on synthetic soft matter systems.

The dynamics of water at and around soft matter interfaces are also intricately coupled to the chemical identity of the interface, and can in turn mediate material performance.[249-251] For example, interfacial water plays an active role in protein function, including mediating protein binding and folding.[252, 253] Investigations into the role of water at and around biomacromolecules has uncovered three "types" of water based on its rate of translational motion: bulk water, hydration water, and structural water. Whereas bulk water far from macromolecular interfaces behaves independently of solute influences, hydration and structural water experience suppressed diffusion from their interactions with a solute.[72, 252] Of note, hydration water can facilitate or inhibit the ability of dissolved species from interacting with a soft matter surface, impacting its performance.[252, 254] Therefore, characterizing and leveraging the dynamics of a material's surface and its surrounding environment offers a critical pathway to enhancing material performance.

Small molecule supramolecular assemblies formed by the spontaneous self-organization of amphiphiles in water represent a material class where interfacial behavior is critical to material function.[16, 24, 53] The tunable surface chemistries and high surface areas hallmark of supramolecular assemblies offer promise for their use in a broad range of applications, including regenerative medicine,[255] photonics,[256] and water treatment.[212]

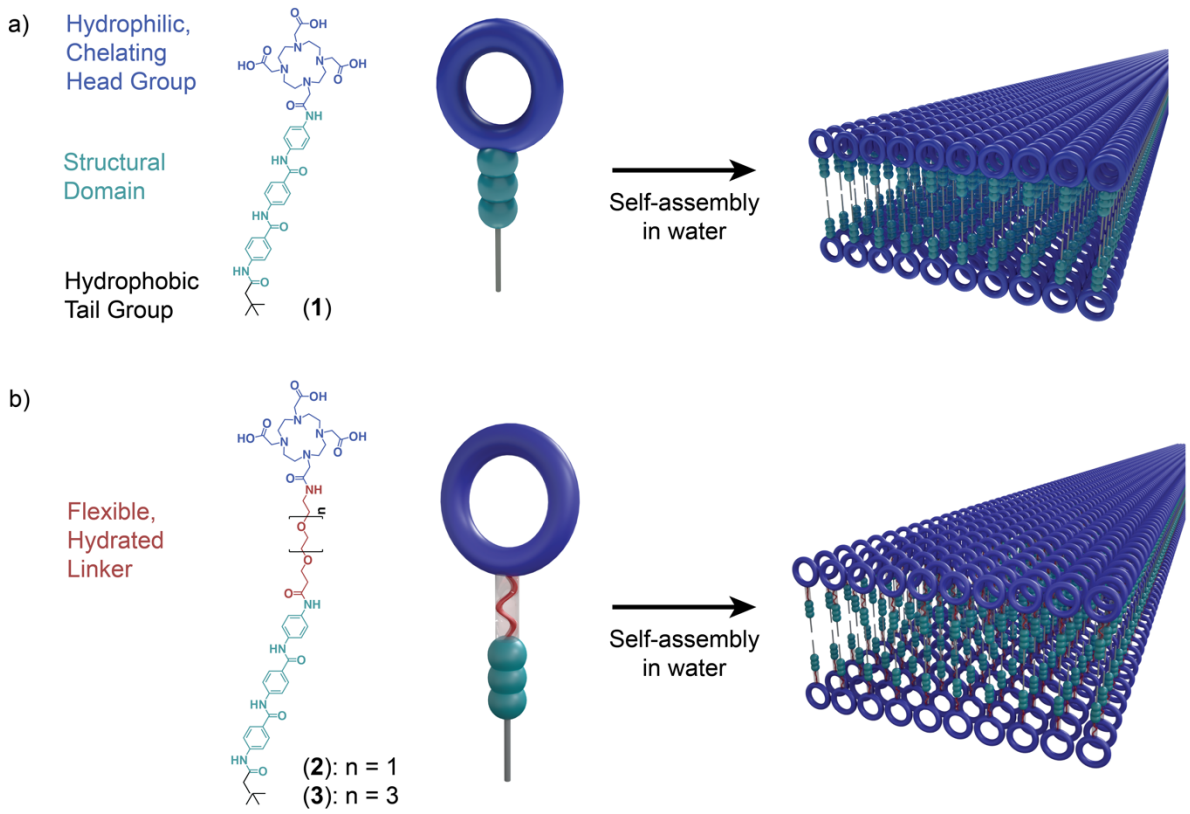

Figure 6.1 | Tunable surface chemistries hallmark of supramolecular assemblies enable control over surface dynamics and hydration. a, Prototypical aramid amphiphiles contain hydrophobic tail and hydrophilic head groups to assist self-assembly, and a structural domain to suppress dynamic exchange and enhance mechanical properties. For this study, a head group which is also capable of complexing heavy metals is chosen to assess the impact of surface dynamics on material performance. **b**, The addition of oligoethylene glycol linkers between the amphiphiles' hydrophobic and hydrophilic domains is hypothesized to enhance the local flexibility and hydration of the chelating head groups, in turn enhancing material performance.

Several reports have demonstrated the significant influence of internal material and hydration dynamics on the properties of supramolecular assemblies,[41, 72, 257, 258] but such dynamics at and above the assembly surface remain largely unexplored. Understanding the influence of interfacial behavior in this regime could enable new molecular design principles to enhance material performance.

Here, we characterize the interfacial dynamics of aramid amphiphiles (AA) nanostructure surfaces and the impact of these dynamics on the nanomaterials' heavy metal remediation performance (Figure 1). AAs incorporate a triaramid structural domain

to impart a cohesive hydrogen bonding and pi stacking network within the resulting self-assembled nanostructures,[51] As a consequence, AA nanostructures demonstrate suppressed molecular migration between assemblies and mechanical properties rivaling silk. Selecting the AA design allows us to more readily isolate impacts from changing surface dynamics by minimizing dynamic instabilities pervasive in conventional supramolecular assemblies.[22, 41, 51]

Results and Discussion

In this study, we incorporate oligo-ethylene glycol (OEG) units of varying length between the AA structural domain and hydrophilic head group to systematically vary surface dynamics (Figure 6.1). OEG groups are well-established for their backbone flexibility and favorable interactions with water,[259, 260] so we hypothesize the incorporation of these groups into the molecular design will enhance surface dynamics and hydration, and consequent water decontamination performance. Compounds (**1**) - (**3**) are AAs with anionic, heavy metal chelating head groups and either no (compound (**1**)), an oligo-ethylene glycol dimer (OEG_2, compound (**2**)), or an oligo-ethylene glycol tetramer (OEG_4, compound (**3**)) linker between the AA structural domain and the head group (Figure 6.1). All compounds were analyzed by NMR and mass spectrometry, and synthesis and chemical characterization details are provided in the Methods section.

We observe compounds (**1**) - (**3**) spontaneously form nanoribbons upon suspension in water via cryogenic transmission electron microscopy (cryo-TEM, Figure 6.2a-c). We employed synchrotron small angle X-ray scattering (SAXS) in combination with cryo-TEM to extract the dimensions of the nanoribbons (Figure 6.2d). The SAXS profiles of compound (**1**) - (**3**) nanostructures were best fit to rectangular prism models which accommodate different scattering length densities for head and tail group domains.[261] From these methods, we extract average cross-sectional dimensions of 3.9 x 8.9 nm,

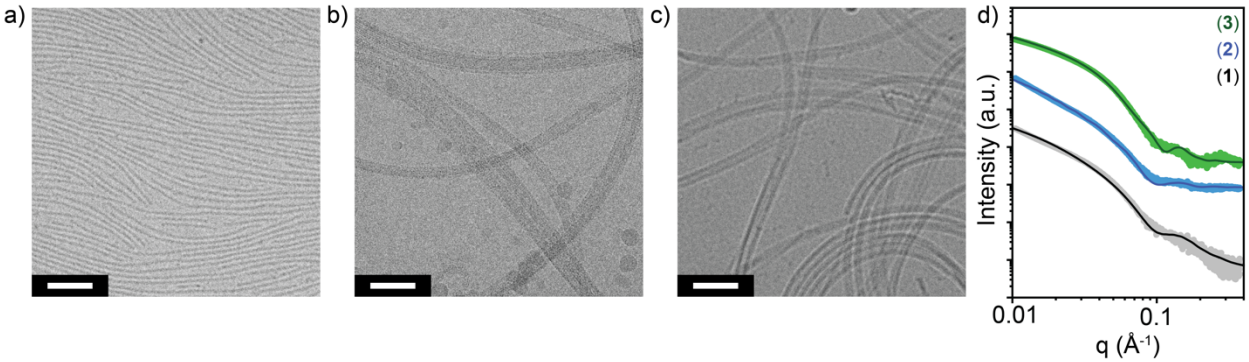

Figure 6.2 | Compounds (1) – (3) spontaneously self-assemble into microns-long nanoribbons in water. The self-assembled nanostructures of compounds **a**, (**1**); **b**, (**2**); and (**c**), 3 are observed with cryogenic transmission electron microscopy. In all cases, the amphiphiles spontaneously assemble into a nanoribbon morphology. Some aggregation of compound (**2**) nanoribbons is observed. Scale bars, 50 nm. **d**, Fitting of synchrotron small angle X-ray scattering profiles of compound (**1**) – (**3**) nanostructures to a core-shell parallelepiped model corroborates approx. 4-6 x 9-12 nm nanoribbon cross-sectional dimensions.

5.0 x 12.0 nm, and 5.8 nm x 10.0 nm for compound (**1**), (**2**), and (**3**) nanoribbons, respectively. In all cases, the nanoribbons extend microns in length.

Electron paramagnetic resonance (EPR)-based techniques take advantage of site-directed spin labeling to quantify localized dynamics with sub-nanometer resolution.[262] By inserting radical nitroxide spin labels into a supramolecular structure, material dynamics at the spin label site can be captured over megahertz to gigahertz range of rotational diffusion rates (D_R, $10^6 – 10^9$ rad^2 s^{-1}).[48] Typical spin labels minimally perturb the structure of molecular systems,[72, 263] and the high sensitivity of EPR techniques enable the use of small amounts of spin labels to produce data.[262] Thus, EPR offers a route to representatively quantify the impacts of material flexibility and hydration dynamics on the dynamics of supramolecular nanostructure surfaces.

Compounds (**4**) - (**6**) were synthesized to probe localized dynamics at the sites of the chelating head groups through co-assembly in nanoribbons of compounds (**1**) – (**3**), respectively (Figure 6.3a). Compounds (**4**) – (**6**) are analogous AAs to compounds (**1**) - (**3**) where the amphiphile head groups have been replaced with electron paramagnetic resonance (EPR)-sensitive TEMPO spin labels. With the inclusion and lengthening of an OEG linker into the head group's design, we find the rotational diffusion rates of the

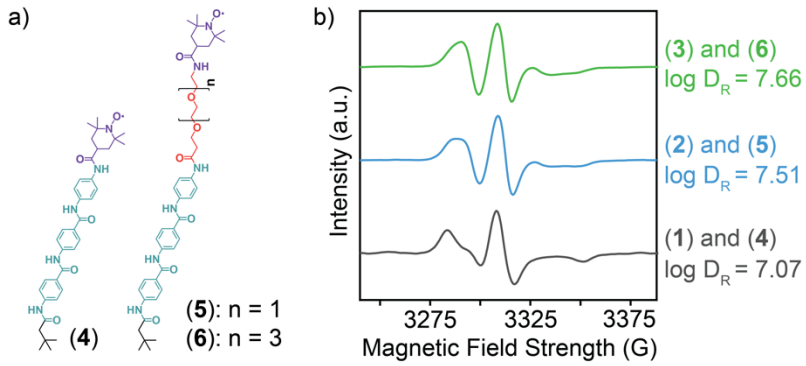

Figure 6.3 | Interfacial material and water dynamics are mediated through incorporation of flexible, hydrated surface linkers. **a,** Compounds (**4**) – (**6**) are spin-labeled (purple) aramid amphiphiles which are co-assembled into compounds (**1**) – (**3**) (Figure 6.1a), respectively, to probe dynamics near surface-tethered chelators. **b,** Electron paramagnetic resonance (EPR) spectroscopy of indicated co-assemblies reveals an over three-fold enhancement in the rotational diffusion constant of probes on nanoribbon surfaces with the incorporation of the longest oligoethylene glycol linker relative to nanoribbon surfaces with no linker.

surface functionalities systematically increase (Figure 6.3b). Notably, D_R nearly triples with the incorporation of OEG_4 onto the surface over nanoribbons without a flexible linker. This enhancement may attributed to both the flexibility of the oligoethylene glycol linkers and their capacity to preserve bulk hydration dynamics beyond the first hydration shell surrounding OEG moieties.[264]

We expect modifying the interfacial behavior of supramolecular nanostructures will have a significant impact on applications which harness surface interactions. Previously, we investigated the ability to employ aramid amphiphile nanoribbons the removal of heavy metal ions from contaminated water.[212] These nanoribbons rely on surface-mediated interactions to complex dissolved heavy metal species with a chelating head group tethered to every amphiphile. In this study, we incorporate a tetraxetan head group onto compounds (**1**) – (**3**) due to its well-established affinity for binding to heavy metal ions,[265] and probe the impact of modulating surface dynamics and hydration on the capture of Pb^{2+} by compound (**1**) – (**3**) nanoribbons in water.

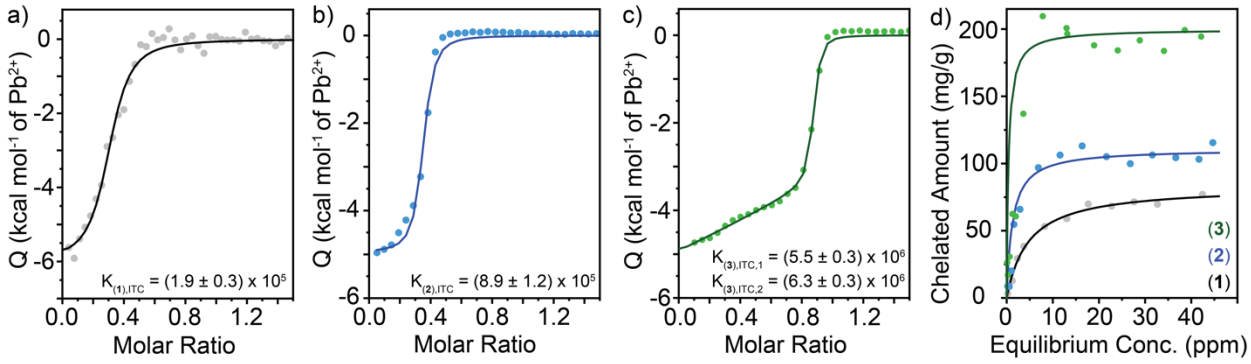

Figure 6.4 | Increasing surface flexibility and hydration enhances lead remediation performance. Isothermal titration calorimetry (ITC) measures the heat released from the complexation of Pb^{2+} ions with tetraxetan head groups coating the supramolecular assemblies' surfaces. ITC profiles of compound **a**, (**1**); **b**, (**2**); and **c**, (**3**) nanoribbons with Pb^{2+} demonstrate systematic increases in the equilibrium binding constant with increases in surface flexibility and hydration. **d**, Fitting adsorption isotherms of compound (**1**) – (**3**) nanoribbons with Pb^{2+} to a Langmuir model reveals a significant enhancement in Pb^{2+} remediation with enhanced surface dynamics. Notably, compound (**3**) nanoribbons saturate at approx. 200 mg Pb^{2+} per gram of amphiphile.

Isothermal titration calorimetry (ITC), which measures the thermodynamics of binding interactions in solution, offers insight into the affinity of the nanoribbons for Pb^{2+} by characterizing the stoichiometry and equilibrium binding constant (K_{ITC}) for complexes of the two species. We extract that the complex between tetraxetan head groups and Pb^{2+} ions for compound (**1**) and (**2**) nanoribbons saturates near 50 mol% Pb^{2+} (Figure 6.4a-b), indicating a 2:1 head group:Pb^{2+} complex stoichiometry consistent with a sandwich-like complex reported elsewhere.[233] In contrast, head groups tethered to compound (**3**) nanoribbons saturate near 100 mol% Pb^{2+} (Figure 6.4c), indicating recovery of the 1:1 tetraxetan:Pb^{2+} complex observed in solution. We also observe notable enhancement in K_{ITC} with increasing lengths of the OEG linker, and an order of magnitude increase in K_{ITC} between compound (**1**) with no OEG linker and compound (**3**) with the longest tested OEG_4 linker (Figure 6.4a-c). Of note, we observe two subsequent binding reactions for compound (3) nanoribbons, which may indicate a switch between 2:1 sandwich-type and 1:1 head group:Pb^{2+} binding to accommodate more Pb^{2+} on the nanoribbon surfaces as the Pb^{2+} concentration increases.

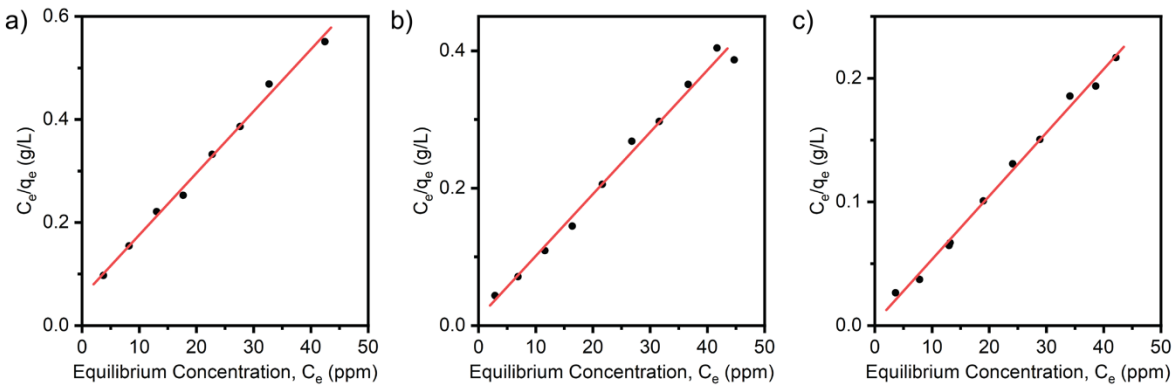

Figure 6.5 l Linear regression of lead adsorption isotherms for compound (**1**), (**2**), and (**3**) nanoribbons, obtained by fitting equilibrium data to a Langmuir adsorption model, accompanying Figure 6.4d.

Finally, we characterize the maximum amount of Pb^{2+} which can be removed from solution by each nanoribbon assembly with lead adsorption isotherms (Figure 6.4d). The maximum saturation capacities (Q_o), reported as mg of Pb^{2+} removed from solution per g of amphiphile used, are determined by quantifying the plateau of the isotherms through fitting the adsorption behavior to a Langmuir model (Figure 6.5). We identify a modest improvement in Pb^{2+} removal by incorporating a OEG_2 linker into compound (**2**) relative to compound (**1**), and a significant enhancement in Pb^{2+} removal by compound (**3**) nanoribbons with an OEG_4 linker. These Q_o values suggest that 700, 450, and 250 μg of compound (**1**), (**2**) and (**3**) nanoribbons, respectively, would be needed to remediate 1 L of 50 ppb Pb^{2+}-contaminated water. For context, the mass of a US penny is 2.5 g;[266] a penny's mass of compound (**3**) nanoribbons could treat up to 10,000 L of 50 ppb Pb^{2+}-contaminated water. These results confirm that mediating surface dynamics to improve head group flexibility and surrounding water mobility greatly enhances the performance of Pb^{2+}-remediating supramolecular assemblies where surface events dominate material performance.

Nature's pristine control over the dynamics of soft matter systems and their aqueous environments provide a powerful contention for leveraging flexibility and hydration in material design. In this report, we identified molecular design characteristics capable of significantly enhancing interfacial material and water dynamics in a supramolecular system designed for heavy metal remediation. We combined this control over dynamics

with chemical design and the extraordinarily high surface areas hallmark of supramolecular assemblies to create nanostructures capable of remediating thousands of liters of heavy metal contaminated water per gram of material. These results suggest material and environmental behavior dictate the performance of systems where interfacial interactions are critical to material function, and offer design principles towards realizing enhancing this performance.

Methods

Synthesis and Chemical Characterization

Full synthesis and characterization details to obtain compounds (**1**) – (**6**) are provided below. In short, compounds (**1**) – (**6**) were synthesized using alternating carbodiimide-mediated amidation and standard deprotection reactions. ^{1}H nuclear magnetic resonance (NMR) spectroscopy of samples in deuterated dimethylsulfoxide (DMSO-d_6) was conducted on a Bruker Avance III DPX 400. Molecular weights of synthesized compounds were investigated by matrix assisted laser desorption/ionization-time-of-flight mass spectrometry (MALDI-ToF MS) on a Bruker Omniflex instrument with a Reflectron accessory. The supernatant of a saturated α-cyano-4-hydroxycinnamic acid in 500:500:1 water:acetonitrile:TFA by volume solution was used as the MALDI-ToF matrix. MALDI-ToF samples were prepared by mixing amphiphile solutions with this matrix and SpheriCal Peptide Low (Polymer Factory) as an internal calibrant.

Materials

Methyl 4-aminobenzoate (Sigma Aldrich, 98%), 3,3-dimethylbutyric acid (Sigma Aldrich, 98%), *N*-Boc-*p*-phenylenediamine (BPP, Sigma Aldrich, 97%), *N*-Boc-3-[2-(2-aminoethoxy)ethoxy]propionic acid (Ambeed Inc., 95%), Boc-15-amino-4,7,10,13-tetraoxapentadecanoic acid (Chem Impex. 95%), 2-(4,7,10-tris(2-tert-butoxy-2-oxoethyl)-1,4,7,10-tetraazacyclododecan-1-yl)acetic acid (DOTA-tris(*t*-Bu ester), AstaTech, 95%), 4-Carboxy-2,2,6,6-tetramethylpiperidine 1-oxyl (4-Carboxy-TEMPO, Sigma Aldrich, 97%), 1-ethyl-3-(3-dimethylaminopropyl)carbodiimide hydrochloride (EDC, TCI

Chemicals, 98%), *N,N'*-Diisopropylcarbodiimide (DIC, Chem Impex. 99%), 4-dimethylaminopyridine (DMAP, TCI Chemicals, 99%), ethyl cyano(hydroxyimino)acetate (TCI Chemicals, 98%), lithium hydroxide monohydrate ($LiOH \cdot H_2O$, Alfa Aesar, 98%), sodium bicarbonate ($NaHCO_3$, Alfa Aesar, 99%), hydrochloric acid (HCl, Alfa Aesar, 36%), sodium sulfate (Na_2SO_4, Fisher Scientific, 99%), magnesium sulfate ($MgSO_4$, J.T. Baker, anhydrous, 99%), sodium chloride (HCl, Fisher Scientific, 99%), trifluoroacetic acid (TFA, Alfa Aesar, 99%), methanol (Fisher Scientific), acetonitrile (Fisher Scientific), methylene chloride (Fisher Scientific), *N,N*-dimethylformamide (dimethylformamide, Fisher Scientific), and ethyl acetate (Fisher Scientific) were used as received without further purification.

Synthesis of chelating amphiphiles

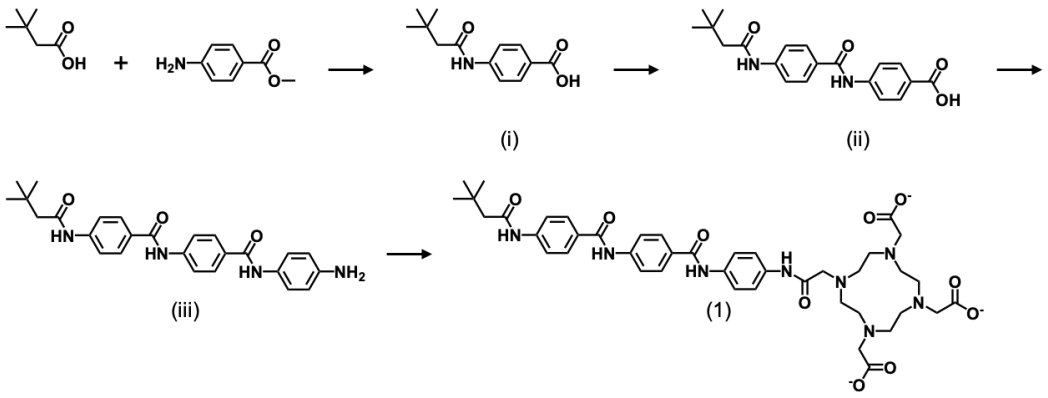

Scheme 6.1 I Synthesis scheme to obtain compound (**1**).

4-(3,3-dimethylbutanamido)benzoic acid (**i**): A solution of 3,3-dimethylbutyric acid (50 mmol), methyl 4-aminobenzoate (33 mmol), EDC (100 mmol), and DMAP (100 mmol) in dimethylformamide (150 mL) was stirred at 60 °C for 24 h. After the reaction, excess deionized water was added to the solution to obtain a precipitate, which was collected by filtration. The crude precipitate was further mixed with methanol and then precipitated in a 5 wt% sodium bicarbonate (aq) solution. The precipitate was then obtained by filtration, washed with 5 wt% sodium bicarbonate (aq) solution, and dried under vacuum. Lithium hydroxide monohydrate (290 mmol) was dissolved in deionized water (60 mL), and added

to a stirred solution of the precipitate compound in tetrahydrofuran (240 mL) and methanol (120 mL). The mixture was refluxed for 24 h. The volatile fraction was then evaporated under reduced pressure and neutralized with an aqueous 1% hydrochloric acid solution. The precipitate was filtered off, washed with water, and dried under vacuum to afford the product (yield: 89.4%).

4-(4-(3,3-dimethylbutanamido)benzamido)benzoic acid (**ii**): A solution of methyl 4-aminobenzoate (45 mmol), compound **i** (30 mmol), EDC (90 mmol), and DMAP (90 mmol) in dimethylformamide (200 mL) was stirred at 60 °C for 24 h. After the reaction, excess deionized water was added to the solution to obtain a precipitate, which was collected by filtration. The crude precipitate was further washed with methanol and acetonitrile, and then dried under vacuum. Lithium hydroxide monohydrate (300 mmol) was dissolved in deionized water (80 mL) and added to a stirred solution of the precipitate compound in tetrahydrofuran (320 mL) and methanol (160 mL). The mixture was refluxed for 24 h. The volatile fraction was then evaporated under reduced pressure and neutralized with an aqueous 1% hydrochloric acid solution. The precipitate was filtered off, washed with water and methanol, and dried under vacuum to afford the product (yield: 62.0%).

N-(4-(amino)phenyl)-4-(4-(3,3-dimethylbutanamido)benzamido)benzamide (**iii**): A solution of BPP (36 mmol), compound **ii** (18 mmol), EDC (54 mmol), and DMAP (54 mmol) in dimethylformamide (200 mL) was stirred at 60 °C for 24 h. After the reaction, excess deionized water was added to the solution to obtain a precipitate, which was collected by filtration. The crude precipitate was further washed with methanol, and then dried under vacuum. TFA (20 mL) and the precipitate compound were mixed in chloroform (180 mL) for 24 h at room temperature. Then, the volatile components were removed *in vacuo* and the remaining mixture was washed with saturated sodium bicarbonate (aq) solution to afford the final product, which was obtained by filtration and dried under vacuum (yield: 91.4%).

2,2',2''-(10-(2-((4-(4-(4-(3,3-dimethylbutanamido)benzamido)benzamido)phenyl) amino)-2-oxoethyl)-1,4,7,10-tetraazacyclododecane-1,4,7-triyl)triacetate (**1**): A solution of DOTA-tris(*t*-Bu ester) (1.65 mmol), compound **ii** (1.38 mmol), EDC (4.13 mmol), and DMAP (4.13 mmol) in dimethylformamide (25 mL) was stirred at 60 °C for 24 h. After the

reaction, the solvent was removed *in vacuo* and the mixture was suspended in a solution of 20 g sodium chloride dissolved in 100 mL deionized water to obtain a precipitate. The precipitate was obtained by filtration and dried under vacuum. The precipitate was then mixed with TFA (3 mL) and stirred for 24 h at room temperature. Afterwards, the volatile components were removed *in vacuo* and the remaining residue was mixed with ethyl acetate to afford the final product as a precipitate. The product was obtained by filtration and dried under vacuum (yield: 43.2%).

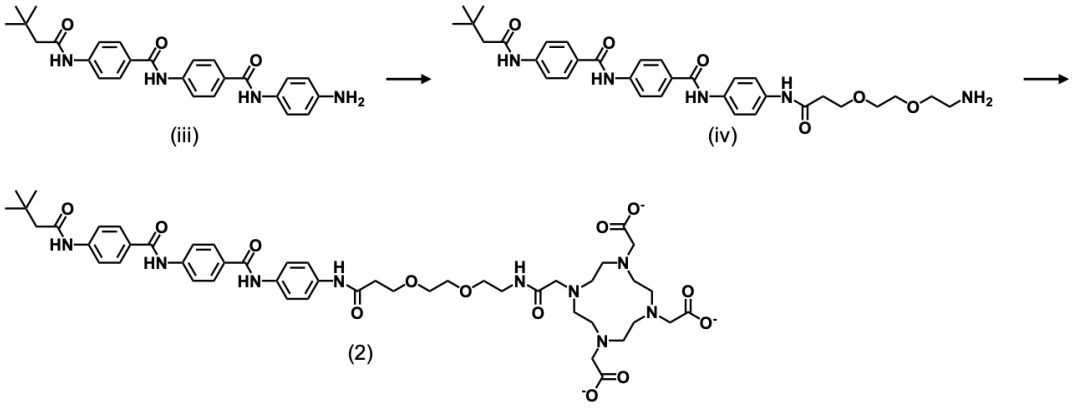

Scheme 6.2 ISynthesis scheme to obtain compound (**2**)

N-(4-(3-(2-(2-aminoethoxy)ethoxy)propanamido)phenyl)-4-(4-(3,3dimethylbutanamido)benzamido)benzamide (**iv**): A solution of compound **iii** (0.90 mmol), *N*-Boc-3-[2-(2-aminoethoxy)ethoxy]propionic acid (1.80 mmol), DIC (3.60 mmol), and ethyl cyano(hydroxyimino)acetate (3.60 mmol) in a mixture of dimethylformamide (50 mL) and methylene chloride (50 mL) was stirred at room temperature for 24 h. After the reaction, the solvent was removed *in vacuo*, and the remaining residue was washed with deionized water and acetonitrile. The isolated compound was then reacted with TFA (10 mL) in methylene chloride (100 mL) at room temperature for 9 h. The volatile fraction was evaporated under reduced pressure. A cosolvent of 9 : 1 diethyl ether : methylene chloride was added to recrystallize the product, which was subsequently separated from the solvent by centrifugation at 4000 rpm for 3 minutes. Afterwards, the precipitate was collected. The remaining product in the centrifuge tube was resuspended in solvent and

centrifuged to collect three more times. The solid precipitate was collected and dried under vacuum (yield: 97.6%).

2,2',2''-(10-(2-((2-(2-(3-((4-(4-(4-(3,3-dimethylbutanamido)benzamido)benzamido) phenyl)amino)-3-oxopropoxy)ethoxy)ethyl)amino)-2-oxoethyl)-1,4,7,10-tetraazacyclodo decane-1,4,7-triyl)triacetate (**2**): A solution of compound **iv** (0.18 mmol), DOTA-tris(*t*-Bu ester) (0.36 mmol), DIC (0.54 mmol), and ethyl cyano(hydroxyimino)acetate (0.54 mmol) in a mixture of dimethylformamide (10 mL) and methylene chloride (10 mL) was stirred at room temperature for 72 h. After the reaction, the solvent was removed *in vacuo* and the remaining residue was dissolved in methylene chloride. The solution was washed by a cosolvent of 5:5 deionized water:methanol via solvent extraction and the organic fraction in methylene chloride was dried using magnesium sulfate and filtered. The organic layer was retained and the volatile fraction was evaporated under reduced pressure. A cosolvent of 9 : 1 diethyl ether : methylene chloride was added to recrystallize the product, which was subsequently separated from the solvent by centrifugation at 4000 rpm for 3 minutes. Afterwards, the precipitate was collected. The remaining compound in the centrifuge tube was resuspended in solvent and centrifuged to collect three more times. All retained compound was then dried in vacuum. The isolated compound was then reacted with TFA (4 mL) in methylene chloride (10 mL) at room temperature for 24 h. The volatile fraction was evaporated under reduced pressure, and the remaining residue was suspended in ethyl acetate. This mixture was centrifuged at 4000 rpm for 3 minutes and the precipitate was collected. The remaining product in the centrifuge tube was resuspended in ethyl acetate and centrifuged to collect three more times. All retained product was then dried under vacuum (yield: 24.9%).

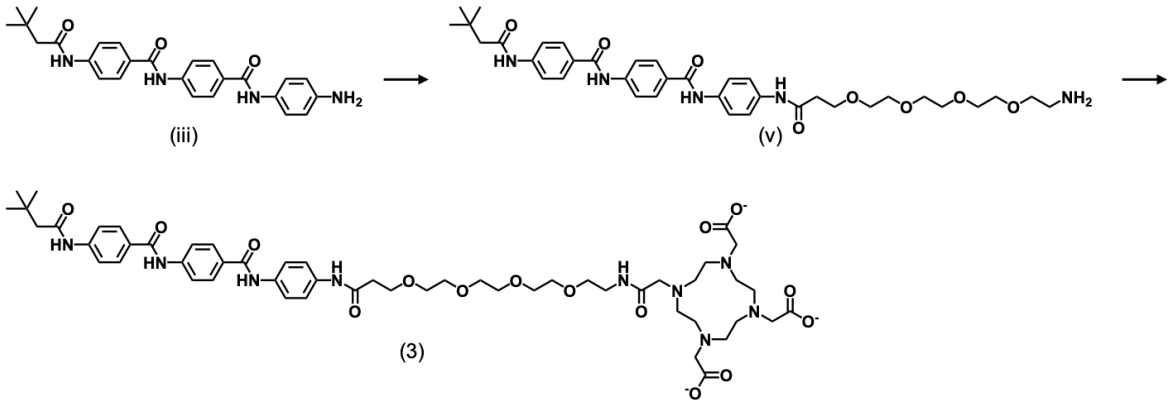

Scheme 6.3 I Synthesis scheme to obtain compound (**3**).

N-(4-(1-amino-3,6,9,12-tetraoxapentadecan-15-amido)phenyl)-4-(4-(3,3-dimethy lbutanamido)benzamido)benzamide (**v**): A solution of compound **iii** (0.69 mmol), Boc-15-amino-4,7,10,13-tetraoxapentadecanoic acid (1.37 mmol), DIC (1.37 mmol), and ethyl cyano(hydroxyimino)acetate (1.37 mmol) in a mixture of dimethylformamide (35 mL) and methylene chloride (35 mL) was stirred at room temperature for 24 h. After the reaction, the solvent was removed *in vacuo*, and the remaining residue was washed with deionized water. The isolated crude product was then reacted with TFA (10 mL) in methylene chloride (100 mL) at room temperature for 5 h. The volatile fraction was evaporated under reduced pressure. A cosolvent of 9 : 1 diethyl ether : methylene chloride was added to recrystallize the product, which was subsequently separated from the solvent by centrifugation at 4000 rpm for 3 minutes. Afterwards, the precipitate was collected. The remaining product in the centrifuge tube was resuspended in solvent and centrifuged to collect three more times. The solid precipitate was collected and dried in vacuum (yield: 77.3%).

2,2',2''-(10-(18-((4-(4-(4-(3,3-dimethylbutanamido)benzamido)benzamido)phenyl) amino)-2,18-dioxo-6,9,12,15-tetraoxa-3-azaoctadecyl)-1,4,7,10-tetraazacyclododecane-1,4,7-triyl)triacetate (**3**): A solution of compound **v** (0.28 mmol), DOTA-tris(*t*-Bu ester) (0.56 mmol), DIC (0.84 mmol), and ethyl cyano(hydroxyimino)acetate (0.84 mmol) in a mixture of dimethylformamide (16 mL) and methylene chloride (16 mL) was stirred at room temperature for 72 h. After the reaction, the solvent was removed *in vacuo* and the remaining residue was dissolved in methylene chloride. The solution was washed by a

cosolvent of 5 : 5 deionized water : methanol via solvent extraction and the organic fraction in methylene chloride was dried using magnesium sulfate and filtered. The organic layer was retained and the volatile fraction was evaporated under reduced pressure. A cosolvent of 9 : 1 diethyl ether : methylene chloride was added to recrystallize the product, which was separated from the solvent by centrifugation at 4000 rpm for 3 minutes. Afterwards, the precipitate was collected. The remaining compound in the centrifuge tube was resuspended in solvent and centrifuged to collect three more times. All retained compound was then dried in vacuum. The isolated compound was then reacted with TFA (8 mL) in methylene chloride (20 mL) at room temperature for 24 h. The volatile fraction was evaporated under reduced pressure. The remaining residue was suspended in ethyl acetate and collected by centrifugation at 4000 rpm for 3 minutes and the precipitate was collected. The remaining product in the centrifuge tube was resuspended in solvent and centrifuged to collect three more times. All retained product was then dried under vacuum. (yield: 44.5%).

Synthesis of spin-labeled compounds

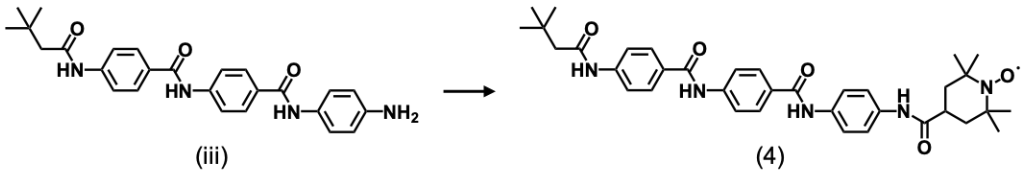

Scheme 6.4 I Synthesis scheme to obtain compound (**4**).

N-(4-(4-(4-(3,3-dimethylbutanamido)benzamido)benzamido)phenyl)-1-hydroxy-2,2,6,6-tetramethylpiperidine-4-carboxamide (**4**): A solution of compound (**iii**) (0.34 mmol), 4 Carboxy-TEMPO (1.02 mmol), EDC (1.02 mmol), DMAP (1.02 mmol), and DIPEA (3.04 mmol) in 7 mL dimethylformamide and 7 mL methylene chloride was mixed for 24 h at room temperature. The solution was then rotovapped to remove volatile components and suspended in deionized water to obtain a precipitate, which was obtained by filtration and dried under vacuum. The dried filtrate was suspended in cold acetonitrile and filtered to obtain the final product (yield: 46.2%).

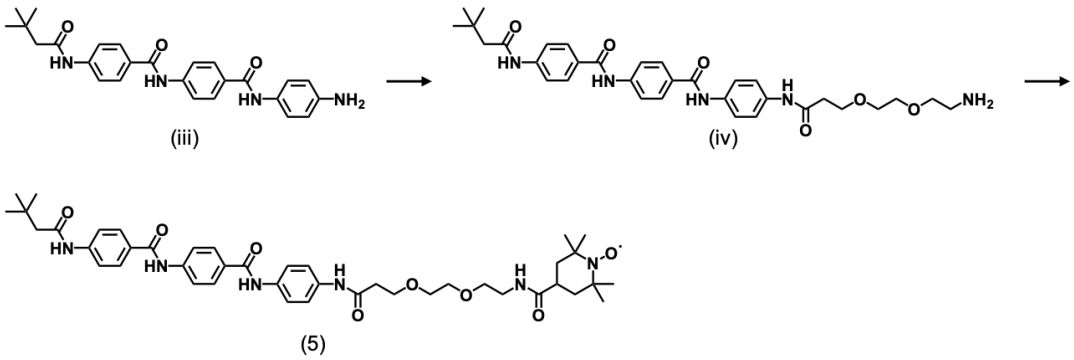

Scheme 6.5 I Synthesis scheme to obtain compound (**5**).

N-(2-(2-(3-((4-(4-(4-(3,3-dimethylbutanamido)benzamido)benzamido)phenyl)amino)-3-oxopropoxy)ethoxy)ethyl)-1-hydroxy-2,2,6,6-tetramethylpiperidine-4-carboxamide (**5**): A solution of compound **iv** (0.20 mmol), 4-Carboxy-TEMPO (0.40 mmol), EDC (0.60 mmol), and DMAP (0.60 mmol), and DIPEA (0.60 mmol) in dimethylformamide (4 mL) and methylene chloride (4 mL) was stirred at room temperature for 72 h. After the reaction, the solvent was removed *in vacuo*, and the remaining residue was washed with deionized water. The crude product was suspended in acetonitrile and collected by centrifugation at 4000 rpm for 3 minutes, and the precipitate was collected. The remaining product in the centrifuge tube was resuspended in solvent and centrifuged to collect three more times. All retained product was then dried under vacuum (yield: 36.5%).

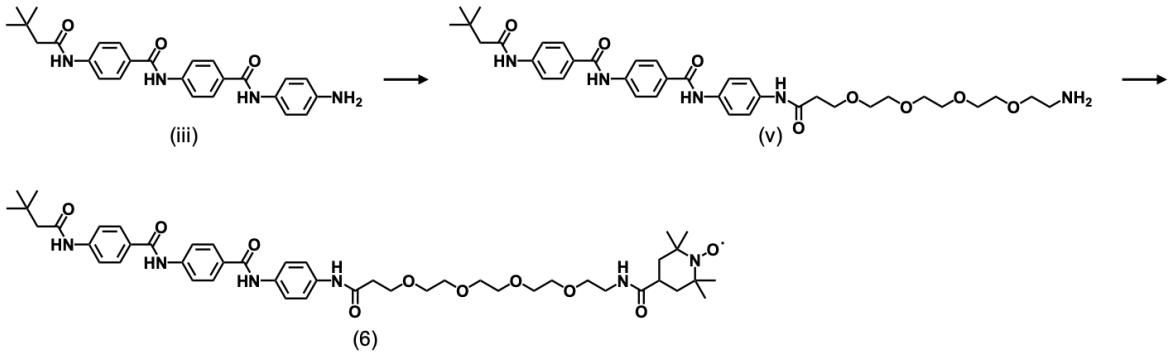

Scheme 6.6 I Synthesis scheme to obtain the compound (**6**).

N-(15-((4-(4-(4-(3,3-dimethylbutanamido)benzamido)benzamido)phenyl)amino)-15-oxo-3,6,9,12-tetraoxapentadecyl)-1-hydroxy-2,2,6,6-tetramethylpiperidine-4-carboxamide (**6**): A solution of compound (**v**) (0.25 mmol), 4-Carboxy-TEMPO (0.50 mmol), EDC (0.60 mmol), and DMAP (0.75 mmol), DIPEA (0.75 mmol) in dimethylformamide (4 mL) and methylene chloride (4 mL) was stirred at room temperature for 72 h. After the reaction, the solvent was removed *in vacuo*, and the remaining residue was washed with deionized water. The crude product was suspended in acetonitrile and collected by centrifugation at 4000 rpm for 3 minutes and the precipitate was collected. The remaining product in the centrifuge tube was resuspended in solvent and centrifuged to collect three more times. All retained product was then dried under vacuum (yield: 45.3%).

Structural Characterization

Self-assembled nanostructures were imaged by cryogenic transmission electron microscopy (cryo-TEM) on a Talos Arctica G2 microscope set to a 200 kV accelerating voltage. Vitrified grids were prepared by pipetting 3 μL of 0.5 mg mL^{-1} nanoribbon suspensions onto glow-discharged holey carbon grids (Quantifoil, 300 mesh, copper) in a FEI Vitrobot Mark IV at 100% humidity. Grids were then blotted for 4 s, plunged into liquid ethane, and preserved in liquid nitrogen.

Bulk structural characterization of nanostructure morphology was performed via small angle X-ray scattering (SAXS) at Beamline 12-ID-B of the Advanced Photon Source at Argonne National Laboratory. SAXS was performed on 5 mg mL^{-1} suspensions of molecular assemblies in quartz capillary tubes (Hampton Research, 2 mm diameter) at 13.3 keV X-ray radiation energy and with a DECTRIS PILATUS 2M detector. 1D SAXS profiles for each sample and their background subtraction of a capillary filled with deionized water was performed with beamline software.

Transmission electron microscopy (TEM) to verify co-assembly nanostructures was performed on a FEI Tecnai G2 Spirit TWIN microscope set to a 120 kV accelerating voltage. Grids were prepared by pipetting 5 μL of 1 mg mL^{-1} nanoribbon suspensions onto continuous carbon grids (Electron Microscopy Sciences, 200 mesh, copper) for 20 s,

wicking to remove the solution, staining with 5 μL of 1% phosphotungistic acid (aq, Electron Microscopy Sciences), and wicking to remove the stain.

Electron Paramagnetic Resonance (EPR) Spectroscopy

EPR spectra were collected at 298 K on a Bruker EMXplus spectrometer with the center field set at 3,315 G and a 150 G sweep width. EPR samples were loaded into Teflon capillaries (1 mm inner diameter, 1.6 mm outer diameter, MSC Industrial Supply Co.) which were capped with Critoseal before analysis. Co-assemblies were prepared by mixing 5 mg mL^{-1} solutions of compounds (**1**) – (**3**) dissolved in *N*,*N*-dimethylformamide (DMF) with their respective spin labeled counterpart (**4**) – (**6**) dissolved in DMF with 5% NH_4OH (aq). These mixtures were held for 12 h at 80 ºC to evaporate volatile components, lyophilized for 24 h to remove trace volatiles, suspended in deionized water to achieve an amphiphile concentration of 5 mg mL^{-1}, and bath sonicated for 1 h to produce nanoribbon co-assemblies. Exchange broadening is observed at spin label concentrations exceeding 10 mol% in the co-assemblies, so we selected 5 mol% spin label concentrations across all samples. Spectra were analyzed using the Chi-Squared Cluster Analysis spectral simulation toolkit,[267] and the medoid is reported as the best representation of the rotational diffusion constant (D_R) from this fitting.

Characterization of Heavy Metal Remediation

Aqueous solutions of Pb^{2+} refer to lead (II) nitrate (Sigma-Aldrich) dissolved in deionized water.

Isothermal titration calorimetry (ITC) was performed on a MicroCal VP-ITC ultrasensitive titration calorimeter with 0.3 mM amphiphile and 3.0 mM Pb^{2+} aqueous solutions. Background heat of dilution from injecting Pb^{2+} into nanoribbon-free water is subtracted from all data. ITC experiments were performed in the absence of buffer due to the insolubility of lead species in most buffers. However, negligible signal results from the injection of water into nanoribbon solutions. Binding isotherms were captured at 25ºC and analyzed using instrument software.

Measurements of Pb^{2+} concentrations to construct adsorption isotherms were taken on an Agilent 7900 inductively coupled plasma-mass spectrometer (ICP-MS). Samples were digested in a 2% hydrochloric acid/2% nitric acid aqueous solution for analysis. The instrument was calibrated using a 10 ppm Pb standard (Ricca Chemical) and all samples were internally calibrated to a 10 ppm Rh standard (Sigma-Aldrich). To prepare samples for adsorption isotherm testing, aqueous mixtures with constant concentrations of compound (**1**) – (**3**) nanoribbons and variable concentrations of Pb^{2+} were prepared, mixed, and equilibrated for 24 h. These solutions were then centrifuged for 5 min at 10,000 rcf and the supernatants were retained for analysis.

Chapter 7

Future Outlook

In this dissertation, I explored how incorporating robust intermolecular interactions between molecules in a supramolecular assembly can give rise to unusual properties that can enable the translation of such nanomaterials to a broad range of new application spaces. The learnings from these studies offer promise to address a range of new challenges spanning basic science to pressing applications.

Characterizing water dynamics above material surfaces

The behavior of water above material surfaces is a topic of intense scrutiny which impacts nearly all scientific fields, spanning catalysis, mineralogy, tribology, biology, atmospheric chemistry, and beyond.[268] Though it is widely accepted that the dynamics of water generally differ greatly near material surfaces than in the bulk,[252, 269, 270] it has historically been difficult to experimentally systematically analyze the behavior of water while holding material parameters constant (i.e. to isolate the behavior of water separately from material dynamics). Outstanding questions in the field include: precisely what is the dynamic behavior of water immediately above a charged material surface, and how does this behavior change with high resolution further from a material surface? How do these dynamics compare with nonpolar or polar uncharged surfaces? How does the introduction of salts impact water behavior? How could manipulating water dynamics be used to enhance material performance?

Both a material system with stable internal dynamics and customizable surface chemistries and an appropriate experimental technique are needed to accurately address these questions. Advances in electron paramagnetic resonance (EPR) spectroscopy and Overhauser dynamic nuclear polarization (ODNP) spectroscopy may offer an appropriate characterization approach to this end. EPR and ODNP are able to quantify the material

and hydration dynamics, respectively, of a soft matter system with sub-nanometer resolution around an introduced radical spin label.[48, 72, 271] However, an appropriate material platform for methodically varying surface parameters has thus far been missing.

The aramid amphiphile design may fill this gap. The suppressed exchange dynamics identified in Chapter 2 enable the separation of material dynamics from water dynamics. Aramid amphiphile co-assemblies of amphiphiles with varying head group chemistries and spin labeled molecules would enable an understanding of the impact of surface charge with surface water dynamics. Next, extending the spin label to fixed distances off the nanomaterial surface (e.g. with "molecular rulers" [272]) can be used to measure changes in water dynamics from surface to bulk water with high resolution. Finally, the impact of introducing changes to the aqueous environment (e.g. adding salts of differing valencies and charges, manipulating pH, and altering temperature) on water dynamics can be systematically characterized.

Interrogate recyclability and composites as a replacement for commodity plastics

When Karl Zeigler and Giulio Natta were awarded the 1963 Nobel Prize in Chemistry for developing the first robust synthetic route to obtain polymers from fossil fuels, Prof. Arne Fredga remarked in the Nobel presentation speech, "the scientific and technical consequences of your discovery are immense and cannot even now be fully estimated".[273] Today, we are beginning to understand the depth of this statement. With a projected 25 billion metric tons of plastic produced by 2050, a radical shift must be undertaken to develop alternative materials with significantly enhanced recyclability towards realizing circularity of the materials' life cycle.[274-276]

Polymers comprising traditional single-use plastics have nanoscale entanglement that imparts useful properties like low density and resistance to shattering, but limits recyclability by making chains difficult to separate. The heat required to flow plastics breaks covalent bonds in their backbone, resulting in limited downcycling of recaptured plastics to lower value commodities.[277] Supramolecular assemblies may offer a route to overcome these limitations because of their underlying reliance on noncovalent

intermolecular interactions. In other words, supramolecular materials could be triggerably disassembled and reassembled without heat.

The stability and scalability of aramid amphiphile nanostructures offers promise as a candidate foundation for alternative materials to commodity plastics. For example, I found the stiffness of macroscopic aramid amphiphile materials is comparable to conventional single-use plastics like polyethylene.[51] To enhance other mechanical properties (e.g. strength and elongation at break), composites with aramid amphiphiles should be investigated. Aramid amphiphile threads thus far have been formed solely from divalent, low molecular weight salts. Improved mechanical properties may be observed coordinating nanoribbons with higher-order high-surface-energy materials, such as charged carbon nanotubes or metal nano- or micro-particles. Composites can be tested for recyclability with green solvents or salts to disrupt intermolecular interactions, and the biodegradability of aramid amphiphile nanostructures may also be investigated.

Targeting challenging water contaminants *via* systems chemistry

The weakly polar or amphiphilic nature of some water contaminants renders them difficult to remove using treatment strategies which rely on primarily ionic or dipolar interactions. For example, arsenic is typically present in water as arsenic acid (H_3AsO_4) or arsenous acid (H_3AsO_3), the latter of which is uncharged at neutral pH.[278] These species are pervasive in groundwater in and around Bangladesh, where an estimated 20 million people rely on tube well water laced with toxic levels of arsenic.[279] Failure to respond to this crisis with appropriate material systems has led to widespread suffering, leading to its designation as “humanity’s biggest mass poisoning.”[280]

Chapters 5 and 6 demonstrated how the high-surface-areas and chemical tunability of supramolecular assemblies could be used to remediate divalent heavy metal contaminants from water. However, the formation of supramolecular assemblies requires amphiphilic head groups which are intrinsically polar. In other words, the formation of these assemblies was only possible due to the hydrophilic nature of chelating moieties selected for the amphiphiles’ head groups. Nonpolar or weakly polar chemistries which

are able to remove uncharged water contaminants like arsenic would likely not be intrinsically successful as amphiphilic head groups.

To circumvent this design requirement, our group has explored the potential to use a sacrificial head group which can induce assembly and then be cleaved off (Figure 7.1).[195] We observed that the structural domain in aramid amphiphile assemblies imparts significantly different stability to the hydrophobic core of the nanostructure than the hydrophilic surface. As a consequence, the surface can be selectively thermally cleaved after assembly to leave behind hydrophobic nanoribbons.

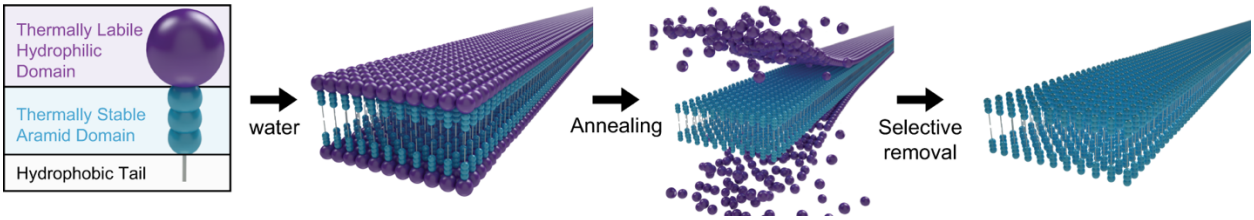

Figure 7.1 I Differential stability between amphiphilic head and tail groups can be harnessed in a systems chemistry approach to use a sacrificial head group to form supramolecular assemblies and subsequently express an underlying surface. Illustrated in this figure, our group demonstrated that the aramid structural domain is significantly more thermally stable than the hydrophilic head groups. Consequently, the hydrophilic surfaces of aramid amphiphile nanoribbons can be cleaved after assembly to produce hydrophobic nanoribbons. Image reproduced from "Domain-selective thermal decomposition within supramolecular nanoribbons," originally published in Nature Communications by Cho, Christoff-Tempesta, et al.[195]

This systems chemistry approach may also offer a route to producing nanostructures coated in nonpolar or weakly polar chemical groups to treat the aforementioned challenging water contaminants. For example, a thiol-based chelator covalently linked to the structural domain of an aramid amphiphile could be temporarily linked to a hydrophilic group. These amphiphiles could then be self-assembled in water, and then chemical reducing agents could be added to the surface to cleave off the hydrophilic groups. The remaining nanoribbon surfaces would then be coated in thiols capable of complexing inorganic arsenic acids.[281]

Solid-state materials for water- and gas-phase contaminant remediation

Producing macroscopic fabrics to treat aqueous and gaseous contaminants is highly desirable for a range of targets. For water contaminants, fabric remediation technologies are effective because the process for obtaining clean drinking water (e.g. straining water through a fabric) is remarkably simple, and the fabrics are small, portable, and easy to deploy.[282, 283] For gaseous contaminants, fabrics are easily transportable to regions of interest and may be readily incorporated into masks or ventilation streams.[284]

Combining principles from Chapter 2 to make solid-state aramid amphiphile macroscopic materials and Chapters 5-6 to capture environmental contaminants on nanomaterial surfaces offers a pathway to target these applications. Several avenues of research are required to achieve these goals. First, nanomaterial surface chemistries must be optimized for both contaminant remediation and structural gelation. This may be achieved through head group chemistries which are capable of both characteristics or through co-assembly of different components responsible imbuing each property. Next, processing techniques can be investigated to produce macroscopic fabrics from aligned nanoribbon gels, including solution blow spinning and electrospinning. Finally, the fabrics may be investigated for remediation capacity, rechargeability, and degradation.

References

1. P. Walde, Surfactant assemblies and their various possible roles for the origin (s) of life, *Origins of Life and Evolution of Biospheres*, 2006, **36**, 109-150.
2. E. Mattia and S. Otto, Supramolecular systems chemistry, *Nature Nanotechnology*, 2015, **10**, 111-119.
3. M. Edidin, Lipids on the frontier: a century of cell-membrane bilayers, *Nature Reviews Molecular Cell Biology*, 2003, **4**, 414-418.
4. A. Chen and V. T. Moy, Cross-linking of cell surface receptors enhances cooperativity of molecular adhesion, *Biophysical Journal*, 2000, **78**, 2814-2820.
5. B. Alberts, A. Johnson, J. Lewis, M. Raff, K. Roberts and P. Walter, in *Molecular Biology of the Cell. 4th edition*, Garland Science, 2002.
6. G. M. Cooper, R. E. Hausman and R. E. Hausman, *The cell: a molecular approach*, ASM press Washington, DC, USA:, 2007.
7. A. Chabanel, M. Flamm, K. Sung, M. Lee, D. Schachter and S. Chien, Influence of cholesterol content on red cell membrane viscoelasticity and fluidity, *Biophysical Journal*, 1983, **44**, 171-176.
8. G. Yu, K. Jie and F. Huang, Supramolecular amphiphiles based on host–guest molecular recognition motifs, *Chemical Reviews*, 2015, **115**, 7240-7303.
9. L. L. Lock, M. LaComb, K. Schwarz, A. G. Cheetham, Y.-a. Lin, P. Zhang and H. Cui, Self-assembly of natural and synthetic drug amphiphiles into discrete supramolecular nanostructures, *Faraday Discussions*, 2013, **166**, 285-301.
10. M. Lee, S.-J. Lee and L.-H. Jiang, Stimuli-responsive supramolecular nanocapsules from amphiphilic calixarene assembly, *Journal of the American Chemical Society*, 2004, **126**, 12724-12725.
11. Y. Zhang, Y. Kuang, Y. Gao and B. Xu, Versatile small-molecule motifs for self-assembly in water and the formation of biofunctional supramolecular hydrogels, *Langmuir*, 2011, **27**, 529-537.
12. E. Yashima, N. Ousaka, D. Taura, K. Shimomura, T. Ikai and K. Maeda, Supramolecular helical systems: helical assemblies of small molecules, foldamers, and polymers with chiral amplification and their functions, *Chemical Reviews*, 2016, **116**, 13752-13990.
13. Z. Yang and B. Xu, Supramolecular hydrogels based on biofunctional nanofibers of self-assembled small molecules, *Journal of Materials Chemistry*, 2007, **17**, 2385-2393.
14. K. Kim, Mechanically interlocked molecules incorporating cucurbituril and their supramolecular assemblies, *Chemical Society Reviews*, 2002, **31**, 96-107.
15. J. W. Lee, S. Samal, N. Selvapalam, H.-J. Kim and K. Kim, Cucurbituril homologues and derivatives: new opportunities in supramolecular chemistry, *Accounts of Chemical Research*, 2003, **36**, 621-630.
16. M. P. Hendricks, K. Sato, L. C. Palmer and S. I. Stupp, Supramolecular assembly of peptide amphiphiles, *Accounts of Chemical Research*, 2017, **50**, 2440-2448.

17. Z. Song, X. Chen, X. You, K. Huang, A. Dhinakar, Z. Gu and J. Wu, Self-assembly of peptide amphiphiles for drug delivery: the role of peptide primary and secondary structures, *Biomaterials Science*, 2017, **5**, 2369-2380.
18. M. J. Webber, J. Kessler and S. Stupp, Emerging peptide nanomedicine to regenerate tissues and organs, *Journal of Internal Medicine*, 2010, **267**, 71-88.
19. H. Cui, M. J. Webber and S. I. Stupp, Self-assembly of peptide amphiphiles: From molecules to nanostructures to biomaterials, *Peptide Science: Original Research on Biomolecules*, 2010, **94**, 1-18.
20. W. Schief, L. Touryan, S. Hall and V. Vogel, Nanoscale topographic instabilities of a phospholipid monolayer, *The Journal of Physical Chemistry B*, 2000, **104**, 7388-7393.
21. R. M. Da Silva, D. Van Der Zwaag, L. Albertazzi, S. S. Lee, E. Meijer and S. I. Stupp, Super-resolution microscopy reveals structural diversity in molecular exchange among peptide amphiphile nanofibres, *Nature Sommunications*, 2016, **7**, 11561.
22. W. C. Wimley and T. E. Thompson, Transbilayer and interbilayer phospholipid exchange in dimyristoylphosphatidylcholine/dimyristoylphosphatidylethanolamine large unilamellar vesicles, *Biochemistry*, 1991, **30**, 1702-1709.
23. J. N. Israelachvili, *Intermolecular and surface forces*, Academic press, 2011.
24. S. Zhang, Fabrication of novel biomaterials through molecular self-assembly, *Nature Biotechnology*, 2003, **21**, 1171.
25. T. Aida, E. Meijer and S. I. Stupp, Functional supramolecular polymers, *Science*, 2012, **335**, 813-817.
26. M. J. Webber, E. A. Appel, E. Meijer and R. Langer, Supramolecular biomaterials, *Nature Materials*, 2016, **15**, 13-26.
27. S. E. Paramonov, H.-W. Jun and J. D. Hartgerink, Self-assembly of peptide–amphiphile nanofibers: the roles of hydrogen bonding and amphiphilic packing, *Journal of the American Chemical Society*, 2006, **128**, 7291-7298.
28. S. S. Babu, V. K. Praveen and A. Ajayaghosh, Functional π-gelators and their applications, *Chemical Reviews*, 2014, **114**, 1973-2129.
29. C. Wang, Q. Chen, H. Xu, Z. Wang and X. Zhang, Photoresponsive Supramolecular Amphiphiles for Controlled Self-Assembly of Nanofibers and Vesicles, *Advanced Materials*, 2010, **22**, 2553-2555.
30. D. S. Kim, J. Chang, S. Leem, J. S. Park, P. Thordarson and J. L. Sessler, Redox- and pH-responsive orthogonal supramolecular self-assembly: An ensemble displaying molecular switching characteristics, *Journal of the American Chemical Society*, 2015, **137**, 16038-16042.
31. M. Zelzer and R. V. Ulijn, Next-generation peptide nanomaterials: molecular networks, interfaces and supramolecular functionality, *Chemical Society Reviews*, 2010, **39**, 3351-3357.
32. J. B. Matson, C. J. Newcomb, R. Bitton and S. I. Stupp, Nanostructure-templated control of drug release from peptide amphiphile nanofiber gels, *Soft Matter*, 2012, **8**, 3586-3595.

33. B. O. Okesola and A. Mata, Multicomponent self-assembly as a tool to harness new properties from peptides and proteins in material design, *Chemical Society Reviews*, 2018, **47**, 3721-3736.
34. S. Fleming and R. V. Ulijn, Design of nanostructures based on aromatic peptide amphiphiles, *Chemical Society Reviews*, 2014, **43**, 8150-8177.
35. E. Beniash, J. D. Hartgerink, H. Storrie, J. C. Stendahl and S. I. Stupp, Self-assembling peptide amphiphile nanofiber matrices for cell entrapment, *Acta Biomaterialia*, 2005, **1**, 387-397.
36. A. G. Cheetham, R. W. Chakroun, W. Ma and H. Cui, Self-assembling prodrugs, *Chemical Society Reviews*, 2017, **46**, 6638-6663.
37. Y. Yamamoto, G. Zhang, W. Jin, T. Fukushima, N. Ishii, A. Saeki, S. Seki, S. Tagawa, T. Minari and K. Tsukagoshi, Ambipolar-transporting coaxial nanotubes with a tailored molecular graphene–fullerene heterojunction, *Proceedings of the National Academy of Sciences*, 2009, **106**, 21051-21056.
38. M. Yemini, M. Reches, E. Gazit and J. Rishpon, Peptide nanotube-modified electrodes for enzyme– biosensor applications, *Analytical Chemistry*, 2005, **77**, 5155-5159.
39. A. S. Weingarten, R. V. Kazantsev, L. C. Palmer, D. J. Fairfield, A. R. Koltonow and S. I. Stupp, Supramolecular packing controls H2 photocatalysis in chromophore amphiphile hydrogels, *Journal of the American Chemical Society*, 2015, **137**, 15241-15246.
40. P. Beker, I. Koren, N. Amdursky, E. Gazit and G. Rosenman, Bioinspired peptide nanotubes as supercapacitor electrodes, *Journal of Materials Science*, 2010, **45**, 6374-6378.
41. Y. Cho, T. Christoff-Tempesta, S. J. Kaser and J. H. Ortony, Dynamics in supramolecular nanomaterials, *Soft Matter*, 2021, **17**, 5850-5863.
42. S. J. Singer and G. L. Nicolson, The fluid mosaic model of the structure of cell membranes, *Science*, 1972, **175**, 720-731.
43. F. M. Goñi, The basic structure and dynamics of cell membranes: An update of the Singer–Nicolson model, *Biochimica et Biophysica Acta (BBA)-Biomembranes*, 2014, **1838**, 1467-1476.
44. M. Edidin, Rotational and translational diffusion in membranes, *Annual Review of Biophysics and Bioengineering*, 1974, **3**, 179-201.
45. K. Naqvi, J. Gonzalez-Rodriguez, R. Cherry and D. Chapman, Spectroscopic technique for studying protein rotation in membranes, *Nature New Biology*, 1973, **245**, 249-251.
46. R. A. Cooper, Influence of increased membrane cholesterol on membrane fluidity and cell function in human red blood cells, *Journal of Supramolecular Structure*, 1978, **8**, 413-430.
47. A. V. Davis, R. M. Yeh and K. N. Raymond, Supramolecular assembly dynamics, *Proceedings of the National Academy of Sciences*, 2002, **99**, 4793-4796.
48. J. H. Ortony, C. J. Newcomb, J. B. Matson, L. C. Palmer, P. E. Doan, B. M. Hoffman and S. I. Stupp, Internal dynamics of a supramolecular nanofibre, *Nature Materials*, 2014, **13**, 812.

49. L. Avram, A. D. Wishard, B. C. Gibb and A. Bar-Shir, Quantifying guest exchange in supramolecular systems, *Angewandte Chemie International Edition*, 2017, **56**, 15314-15318.
50. Y. R. Zheng and P. J. Stang, Direct and Quantitative Characterization of Dynamic Ligand Exchange between Coordination-Driven Self-Assembled Supramolecular Polygons, *Journal of the American Chemical Society*, 2009, **131**, 3487-+.
51. T. Christoff-Tempesta, Y. Cho, D.-Y. Kim, M. Geri, G. Lamour, A. J. Lew, X. Zuo, W. R. Lindemann and J. H. Ortony, Self-assembly of aramid amphiphiles into ultra-stable nanoribbons and aligned nanoribbon threads, *Nature Nanotechnology*, 2021, **16**, 447-454.
52. C. Fong, T. Le and C. J. Drummond, Lyotropic liquid crystal engineering–ordered nanostructured small molecule amphiphile self-assembly materials by design, *Chemical Society Reviews*, 2012, **41**, 1297-1322.
53. T. Christoff-Tempesta, A. J. Lew and J. H. Ortony, Beyond covalent crosslinks: applications of supramolecular gels, *Gels*, 2018, **4**, 40.
54. J. N. Israelachvili, D. J. Mitchell and B. W. Ninham, Theory of self-assembly of hydrocarbon amphiphiles into micelles and bilayers, *Journal of the Chemical Society, Faraday Transactions 2: Molecular and Chemical Physics*, 1976, **72**, 1525-1568.
55. L. Wasungu and D. Hoekstra, Cationic lipids, lipoplexes and intracellular delivery of genes, *Journal of Controlled Release*, 2006, **116**, 255-264.
56. H. Goldfine, Bacterial membranes and lipid packing theory, *Journal of Lipid Research*, 1984, **25**, 1501-1507.
57. J. M. Kim, Y. Sakamoto, Y. K. Hwang, Y.-U. Kwon, O. Terasaki, S.-E. Park and G. D. Stucky, Structural design of mesoporous silica by micelle-packing control using blends of amphiphilic block copolymers, *The Journal of Physical Chemistry B*, 2002, **106**, 2552-2558.
58. N. Baccile, A.-S. Cuvier, S. Prévost, C. V. Stevens, E. Delbeke, J. Berton, W. Soetaert, I. N. Van Bogaert and S. Roelants, Self-assembly mechanism of pH-responsive glycolipids: micelles, fibers, vesicles, and bilayers, *Langmuir*, 2016, **32**, 10881-10894.
59. Y. Wang, Y. Zhang, X. Liu, J. Wang, L. Wei and Y. Feng, Effect of a hydrophilic head group on krafft temperature, surface activities and rheological behaviors of erucyl amidobetaines, *Journal of Surfactants and Detergents*, 2014, **17**, 295-301.
60. J. Israelachvili, S. Marčelja and R. G. Horn, Physical principles of membrane organization, *Quarterly Reviews of Biophysics*, 1980, **13**, 121-200.
61. N. Vlachy, M. Drechsler, J.-M. Verbavatz, D. Touraud and W. Kunz, Role of the surfactant headgroup on the counterion specificity in the micelle-to-vesicle transition through salt addition, *Journal of Colloid and Interface Science*, 2008, **319**, 542-548.
62. M. Hanna-Attisha, J. LaChance, R. C. Sadler and A. Champney Schnepp, Elevated blood lead levels in children associated with the Flint drinking water crisis: a spatial analysis of risk and public health response, *American Journal of Public Health*, 2016, **106**, 283-290.

63. T. M. Olson, M. Wax, J. Yonts, K. Heidecorn, S.-J. Haig, D. Yeoman, Z. Hayes, L. Raskin and B. R. Ellis, Forensic estimates of lead release from lead service lines during the water crisis in Flint, Michigan, *Environmental Science & Technology Letters*, 2017, **4**, 356-361.
64. World Health Organization, Guidelines for Drinking-water Quality. 2011.
65. K. J. Pieper, M. Tang and M. A. Edwards, Flint Water Crisis Caused By Interrupted Corrosion Control: Investigating “Ground Zero” Home, *Environmental Science & Technology*, 2017, **51**, 2007-2014.
66. M. B. Pell and J. Schneyer, *The thousands of U.S. locales where lead poisoning is worse than in Flint*, Reuters, 2016.
67. Institute for Health Metrics and Evaluation, University of Washington, The Global Burden of Disease. 2019.
68. G. M. Whitesides, J. P. Mathias and C. T. Seto, Molecular self-assembly and nanochemistry: a chemical strategy for the synthesis of nanostructures, *Science*, 1991, **254**, 1312-1319.
69. S. Zhang, M. A. Greenfield, A. Mata, L. C. Palmer, R. Bitton, J. R. Mantei, C. Aparicio, M. O. De La Cruz and S. I. Stupp, A self-assembly pathway to aligned monodomain gels, *Nature Materials*, 2010, **9**, 594-601.
70. S. Koutsopoulos, L. D. Unsworth, Y. Nagai and S. Zhang, Controlled release of functional proteins through designer self-assembling peptide nanofiber hydrogel scaffold, *Proceedings of the National Academy of Sciences*, 2009, **106**, 4623-4628.
71. F. Tantakitti, J. Boekhoven, X. Wang, R. V. Kazantsev, T. Yu, J. Li, E. Zhuang, R. Zandi, J. H. Ortony and C. J. Newcomb, Energy landscapes and functions of supramolecular systems, *Nature Materials*, 2016, **15**, 469.
72. J. H. Ortony, B. Qiao, C. J. Newcomb, T. J. Keller, L. C. Palmer, E. Deiss-Yehiely, M. Olvera de la Cruz, S. Han and S. I. Stupp, Water Dynamics from the Surface to the Interior of a Supramolecular Nanostructure, *Journal of the American Chemical Society*, 2017, **139**, 8915-8921.
73. D. Yuan, J. Shi, X. Du, N. Zhou and B. Xu, Supramolecular glycosylation accelerates proteolytic degradation of peptide nanofibrils, *Journal of the American Chemical Society*, 2015, **137**, 10092-10095.
74. S. Toledano, R. J. Williams, V. Jayawarna and R. V. Ulijn, Enzyme-triggered self-assembly of peptide hydrogels via reversed hydrolysis, *Journal of the American Chemical Society*, 2006, **128**, 1070-1071.
75. R. Freeman, M. Han, Z. Álvarez, J. A. Lewis, J. R. Wester, N. Stephanopoulos, M. T. McClendon, C. Lynsky, J. M. Godbe and H. Sangji, Reversible self-assembly of superstructured networks, *Science*, 2018, **362**, 808-813.
76. R. J. Williams, A. M. Smith, R. Collins, N. Hodson, A. K. Das and R. V. Ulijn, Enzyme-assisted self-assembly under thermodynamic control, *Nature Nanotechnology*, 2009, **4**, 19.
77. P. Hashim, J. Bergueiro, E. Meijer and T. Aida, Supramolecular Polymerization: A Conceptual Expansion for Innovative Materials, *Progress in Polymer Science*, 2020, **105**, 101250.

78. Y. Xu, D. Kraemer, B. Song, Z. Jiang, J. Zhou, J. Loomis, J. Wang, M. Li, H. Ghasemi and X. Huang, Nanostructured polymer films with metal-like thermal conductivity, *Nature Communications*, 2019, **10**, 1-8.
79. H. L. Tuller, Ionic conduction in nanocrystalline materials, *Solid State Ionics*, 2000, **131**, 143-157.
80. D. C. Sherrington and K. A. Taskinen, Self-assembly in synthetic macromolecular systems via multiple hydrogen bonding interactions, *Chemical Society Reviews*, 2001, **30**, 83-93.
81. M. Dobb, D. Johnson and B. Saville, Supramolecular structure of a high-modulus polyaromatic fiber (Kevlar 49), *Journal of Polymer Science: Polymer Physics Edition*, 1977, **15**, 2201-2211.
82. H. Seyler, C. Storz, R. Abbel and A. F. Kilbinger, A facile synthesis of aramide–peptide amphiphiles, *Soft Matter*, 2009, **5**, 2543-2545.
83. R. C. Claussen, B. M. Rabatic and S. I. Stupp, Aqueous self-assembly of unsymmetric peptide bolaamphiphiles into nanofibers with hydrophilic cores and surfaces, *Journal of the American Chemical Society*, 2003, **125**, 12680-12681.
84. M. Yang, K. Cao, L. Sui, Y. Qi, J. Zhu, A. Waas, E. M. Arruda, J. Kieffer, M. Thouless and N. A. Kotov, Dispersions of aramid nanofibers: a new nanoscale building block, *ACS Nano*, 2011, **5**, 6945-6954.
85. T. W. Schleuss, R. Abbel, M. Gross, D. Schollmeyer, H. Frey, M. Maskos, R. Berger and A. F. M. Kilbinger, Hockey-Puck Micelles from Oligo(p-benzamide)-b-PEG Rod–Coil Block Copolymers, *Angewandte Chemie International Edition*, 2006, **45**, 2969-2975.
86. A. Bohle, G. Brunklaus, M. R. Hansen, T. W. Schleuss, A. F. M. Kilbinger, J. Seltmann and H. W. Spiess, Hydrogen-Bonded Aggregates of Oligoaramide–Poly(ethylene glycol) Block Copolymers, *Macromolecules*, 2010, **43**, 4978-4985.
87. R. Abbel, T. W. Schleuss, H. Frey and A. F. M. Kilbinger, Rod-Length Dependent Aggregation in a Series of Oligo(p-benzamide)-Block-Poly(ethylene glycol) Rod-Coil Copolymers, *Macromolecular Chemistry and Physics*, 2005, **206**, 2067-2074.
88. A. Johansson, P. Kollman, S. Rothenberg and J. McKelvey, Hydrogen bonding ability of the amide group, *Journal of the American Chemical Society*, 1974, **96**, 3794-3800.
89. D. A. Dixon, K. D. Dobbs and J. J. Valentini, Amide-water and amide-amide hydrogen bond strengths, *Journal of Physical Chemistry*, 1994, **98**, 13435-13439.
90. S. R. Kline, Reduction and analysis of SANS and USANS data using IGOR Pro, *Journal of Applied Crystallography*, 2006, **39**, 895-900.
91. F. Nallet, R. Laversanne and D. Roux, Modelling X-ray or neutron scattering spectra of lyotropic lamellar phases: interplay between form and structure factors, *Journal de Physique II*, 1993, **3**, 487-502.
92. H. D. Mertens and D. I. Svergun, Structural characterization of proteins and complexes using small-angle X-ray solution scattering, *Journal of Structural Biology*, 2010, **172**, 128-141.

93. H. Yokoi, T. Kinoshita and S. Zhang, Dynamic reassembly of peptide RADA16 nanofiber scaffold, *Proceedings of the National Academy of Sciences*, 2005, **102**, 8414-8419.
94. J. D. Hartgerink, E. Beniash and S. I. Stupp, Self-assembly and mineralization of peptide-amphiphile nanofibers, *Science*, 2001, **294**, 1684-1688.
95. G. Cravotto and P. Cintas, Molecular self-assembly and patterning induced by sound waves. The case of gelation, *Chemical Society Reviews*, 2009, **38**, 2684-2697.
96. T. E. Gorelik, J. van de Streek, A. F. Kilbinger, G. Brunklaus and U. Kolb, Ab-initio crystal structure analysis and refinement approaches of oligo p-benzamides based on electron diffraction data, *Acta Crystallographica Section B: Structural Science*, 2012, **68**, 171-181.
97. T. Gorelik, G. Matveeva, U. Kolb, T. Schleuß, A. F. Kilbinger, J. van de Streek, A. Bohle and G. Brunklaus, H-bonding schemes of di-and tri-p-benzamides assessed by a combination of electron diffraction, X-ray powder diffraction and solid-state NMR, *CrystEngComm*, 2010, **12**, 1824-1832.
98. J. Wang, K. Liu, R. Xing and X. Yan, Peptide self-assembly: thermodynamics and kinetics, *Chemical Society Reviews*, 2016, **45**, 5589-5604.
99. A. Barth, Infrared spectroscopy of proteins, *Biochimica et Biophysica Acta - Bioenergetics*, 2007, **1767**, 1073-1101.
100. G. Zandomeneghi, M. R. Krebs, M. G. McCammon and M. Fändrich, FTIR reveals structural differences between native β-sheet proteins and amyloid fibrils, *Protein Science*, 2004, **13**, 3314-3321.
101. E. D. Matayoshi, G. T. Wang, G. A. Krafft and J. Erickson, Novel fluorogenic substrates for assaying retroviral proteases by resonance energy transfer, *Science*, 1990, **247**, 954-958.
102. B. Wu, A. Heidelberg and J. J. Boland, Mechanical properties of ultrahigh-strength gold nanowires, *Nature Materials*, 2005, **4**, 525-529.
103. J. F. Smith, T. P. Knowles, C. M. Dobson, C. E. MacPhee and M. E. Welland, Characterization of the nanoscale properties of individual amyloid fibrils, *Proceedings of the National Academis of Sciences*, 2006, **103**, 15806-15811.
104. T. P. Knowles, A. W. Fitzpatrick, S. Meehan, H. R. Mott, M. Vendruscolo, C. M. Dobson and M. E. Welland, Role of intermolecular forces in defining material properties of protein nanofibrils, *Science*, 2007, **318**, 1900-1903.
105. G. Lamour, J. B. Kirkegaard, H. Li, T. P. Knowles and J. Gsponer, Easyworm: an open-source software tool to determine the mechanical properties of worm-like chains, *Source Code for Biology and Medicine*, 2014, **9**, 16.
106. Y. Y. Huang, T. P. Knowles and E. M. Terentjev, Strength of nanotubes, filaments, and nanowires from sonication-induced scission, *Advanced Materials*, 2009, **21**, 3945-3948.
107. R. Nassar, E. Wong, J. Gsponer and G. Lamour, Inverse Correlation between Amyloid Stiffness and Size, *Journal of the American Chemical Society*, 2019, **141**, 58-61.

108. Z. Peng, A. S. Parker, M. D. R. Peralta, K. M. Ravikumar, D. L. Cox and M. D. Toney, High Tensile Strength of Engineered β-Solenoid Fibrils via Sonication and Pulling, *Biophysical Journal*, 2017, **113**, 1945-1955.
109. H. M. Santos, C. Lodeiro and J.-L. Capelo-Martínez, in *Ultrasound in Chemistry: Analytical Applications*, Wiley Online Library, 2009, pp. 1-16.
110. G. Lamour, R. Nassar, P. H. Chan, G. Bozkurt, J. Li, J. M. Bui, C. K. Yip, T. Mayor, H. Li and H. Wu, Mapping the broad structural and mechanical properties of amyloid fibrils, *Biophysical Journal*, 2017, **112**, 584-594.
111. X. Zhao, F. Pan, H. Xu, M. Yaseen, H. Shan, C. A. Hauser, S. Zhang and J. R. Lu, Molecular self-assembly and applications of designer peptide amphiphiles, *Chemical Society Reviews*, 2010, **39**, 3480-3498.
112. K. L. Niece, J. D. Hartgerink, J. J. Donners and S. I. Stupp, Self-assembly combining two bioactive peptide-amphiphile molecules into nanofibers by electrostatic attraction, *Journal of the American Chemical Society*, 2003, **125**, 7146-7147.
113. N. L. Angeloni, C. W. Bond, Y. Tang, D. A. Harrington, S. Zhang, S. I. Stupp, K. E. McKenna and C. A. Podlasek, Regeneration of the cavernous nerve by Sonic hedgehog using aligned peptide amphiphile nanofibers, *Biomaterials*, 2011, **32**, 1091-1101.
114. L. Fink, A. Steiner, O. Szekely, P. Szekely and U. Raviv, Structure and interactions between charged lipid membranes in the presence of multivalent ions, *Langmuir*, 2019, **35**, 9694-9703.
115. T. P. Knowles and M. J. Buehler, Nanomechanics of functional and pathological amyloid materials, *Nature Nanotechnology*, 2011, **6**, 469-479.
116. R. Bradbury and M. Nagao, Effect of charge on the mechanical properties of surfactant bilayers, *Soft Matter*, 2016, **12**, 9383-9390.
117. Y. Takahashi, Y. Ozaki, M. Takase and W. Krigbaum, Crystal structure of poly (p-benzamide), *Journal of Polymer Science Part B: Polymer Physics*, 1993, **31**, 1135-1143.
118. P. Russell, Photonic crystal fibers, *Science*, 2003, **299**, 358-362.
119. T. Christoff-Tempesta, D.-Y. Kim, G. Lamour, X. Zuo, K.-H. Ryu and J. H. Ortony, Morphological Transitions of a Photoswitchable Aramid Amphiphile Nanostructure, *Nano Letters*, 2021, **21**, 2912-2918.
120. Q. Meng, Y. Kou, X. Ma, Y. Liang, L. Guo, C. Ni and K. Liu, Tunable Self-Assembled Peptide Amphiphile Nanostructures, *Langmuir*, 2012, **28**, 5017-5022.
121. L. Lis, d. McAlister, N. Fuller, R. Rand and V. Parsegian, Interactions between neutral phospholipid bilayer membranes, *Biophysical Journal*, 1982, **37**, 657.
122. K. V. Rao and S. J. George, Supramolecular Alternate Co-Assembly through a Non-Covalent Amphiphilic Design: Conducting Nanotubes with a Mixed D–A Structure, *Chemistry–A European Journal*, 2012, **18**, 14286-14291.
123. Z. Xu, S. Jia, W. Wang, Z. Yuan, B. J. Ravoo and D.-S. Guo, Heteromultivalent peptide recognition by co-assembly of cyclodextrin and calixarene amphiphiles enables inhibition of amyloid fibrillation, *Nature Chemistry*, 2019, **11**, 86-93.

124. G. A. Silva, C. Czeisler, K. L. Niece, E. Beniash, D. A. Harrington, J. A. Kessler and S. I. Stupp, Selective differentiation of neural progenitor cells by high-epitope density nanofibers, *Science*, 2004, **303**, 1352-1355.
125. M.-P. Nieh, V. A. Raghunathan, S. R. Kline, T. A. Harroun, C.-Y. Huang, J. Pencer and J. Katsaras, Spontaneously formed unilamellar vesicles with path-dependent size distribution, *Langmuir*, 2005, **21**, 6656-6661.
126. P. A. Korevaar, C. J. Newcomb, E. W. Meijer and S. I. Stupp, Pathway Selection in Peptide Amphiphile Assembly, *Journal of the American Chemical Society*, 2014, **136**, 8540-8543.
127. R. Dong, Y. Zhou, X. Huang, X. Zhu, Y. Lu and J. Shen, Functional supramolecular polymers for biomedical applications, *Advanced Materials*, 2015, **27**, 498-526.
128. L. Sun, C. Zheng and T. J. Webster, Self-assembled peptide nanomaterials for biomedical applications: promises and pitfalls, *International Journal of Nanomedicine*, 2017, **12**, 73.
129. S. Sur, F. Tantakitti, J. B. Matson and S. I. Stupp, Epitope topography controls bioactivity in supramolecular nanofibers, *Biomaterials Science*, 2015, **3**, 520-532.
130. P. Urban, S. D. Pritzl, M. F. Ober, C. F. Dirscherl, C. Pernpeintner, D. B. Konrad, J. A. Frank, D. Trauner, B. Nickel and T. Lohmueller, A lipid photoswitch controls fluidity in supported bilayer membranes, *Langmuir*, 2020, **36**, 2629-2634.
131. Z. Wu, R. Xue, M. Xie, X. Wang, Z. Liu, M. Drechsler, J. Huang and Y. Yan, Self-Assembly-Triggered Cis-to-Trans Conversion of Azobenzene Compounds, *The Journal of Physical Chemistry Letters*, 2018, **9**, 163-169.
132. R. H. Zha, G. Vantomme, J. A. Berrocal, R. Gosens, B. de Waal, S. Meskers and E. Meijer, Photoswitchable nanomaterials based on hierarchically organized siloxane oligomers, *Advanced Functional Materials*, 2018, **28**, 1703952.
133. C. Maity, W. E. Hendriksen, J. H. van Esch and R. Eelkema, Spatial structuring of a supramolecular hydrogel by using a visible-light triggered catalyst, *Angewandte Chemie International Edition*, 2015, **54**, 998-1001.
134. M. Kathan and S. Hecht, Photoswitchable molecules as key ingredients to drive systems away from the global thermodynamic minimum, *Chemical Society Reviews*, 2017, **46**, 5536-5550.
135. D. Gegiou, K. Muszkat and E. Fischer, Temperature dependence of photoisomerization. V. Effect of substituents on the photoisomerization of stilbenes and azobenzenes, *Journal of the American Chemical Society*, 1968, **90**, 3907-3918.
136. R. H. Dyck and D. S. McClure, Ultraviolet spectra of stilbene, p-monohalogen stilbenes, and azobenzene and the trans to cis photoisomerization process, *The Journal of Chemical Physics*, 1962, **36**, 2326-2345.
137. H. Zhu, L. Shangguan, D. Xia, J. H. Mondal and B. Shi, Control on the photo-responsive assembly of a stilbene-containing amphiphile by using pillar [5] arene-based host–guest interactions, *Nanoscale*, 2017, **9**, 8913-8917.
138. D. Bléger, J. Schwarz, A. M. Brouwer and S. Hecht, o-Fluoroazobenzenes as readily synthesized photoswitches offering nearly quantitative two-way

isomerization with visible light, *Journal of the American Chemical Society*, 2012, **134**, 20597-20600.
139. X. Yao, T. Li, J. Wang, X. Ma and H. Tian, Recent progress in photoswitchable supramolecular self-assembling systems, *Advanced Optical Materials*, 2016, **4**, 1322-1349.
140. S. Choi, S. H. Park, A. Y. Ziganshina, Y. H. Ko, J. W. Lee and K. Kim, A stable cis-stilbene derivative encapsulated in cucurbit [7] uril, *Chemical Communications*, 2003, DOI: 10.1039/b306832c, 2176-2177.
141. E. Uchida, K. Sakaki, Y. Nakamura, R. Azumi, Y. Hirai, H. Akiyama, M. Yoshida and Y. Norikane, Control of the orientation and photoinduced phase transitions of macrocyclic azobenzene, *Chemistry–A European Journal*, 2013, **19**, 17391-17397.
142. I. Levchuk, Y. Hou, M. Gruber, M. Brandl, P. Herre, X. Tang, F. Hoegl, M. Batentschuk, A. Osvet and R. Hock, Deciphering the role of impurities in methylammonium iodide and their impact on the performance of perovskite solar cells, *Advanced Materials Interfaces*, 2016, **3**, 1600593.
143. R. Nayuk and K. Huber, Formfactors of Hollow and Massive Rectangular Parallelepipeds at Variable Degree of Anisometry, *Zeitschrift für Physikalische Chemie*, 2012, **226**, 837-854.
144. L. Feigin and D. I. Svergun, *Structure analysis by small-angle X-ray and neutron scattering*, Springer, 1987.
145. B. Adhikari, Y. Yamada, M. Yamauchi, K. Wakita, X. Lin, K. Aratsu, T. Ohba, T. Karatsu, M. J. Hollamby, N. Shimizu, H. Takagi, R. Haruki, S.-i. Adachi and S. Yagai, Light-induced unfolding and refolding of supramolecular polymer nanofibres, *Nature Communications*, 2017, **8**, 15254.
146. D. D. Prabhu, K. Aratsu, Y. Kitamoto, H. Ouchi, T. Ohba, M. J. Hollamby, N. Shimizu, H. Takagi, R. Haruki, S.-i. Adachi and S. Yagai, Self-folding of supramolecular polymers into bioinspired topology, *Science Advances*, 2018, **4**, eaat8466.
147. H. Wang and M. Lee, Switching between Stacked Toroids and Helical Supramolecular Polymers in Aqueous Nanotubules, *Macromolecular Rapid Communications*, 2020, **41**, 2000138.
148. J. W. Fredy, A. Méndez-Ardoy, S. Kwangmettatam, D. Bochicchio, B. Matt, M. C. A. Stuart, J. Huskens, N. Katsonis, G. M. Pavan and T. Kudernac, Molecular photoswitches mediating the strain-driven disassembly of supramolecular tubules, *Proceedings of the National Academy of Sciences*, 2017, **114**, 11850-11855.
149. L. Ziserman, H.-Y. Lee, S. R. Raghavan, A. Mor and D. Danino, Unraveling the mechanism of nanotube formation by chiral self-assembly of amphiphiles, *Journal of the American Chemical Society*, 2011, **133**, 2511-2517.
150. D. Wu, L. Zhi, G. J. Bodwell, G. Cui, N. Tsao and K. Müllen, Self-assembly of positively charged discotic PAHs: from nanofibers to nanotubes, *Angewandte Chemie International Edition*, 2007, **46**, 5417-5420.

151. D.-Y. Kim, W.-J. Yoon, Y.-J. Choi, S.-I. Lim, J. Koo and K.-U. Jeong, Photoresponsive chiral molecular crystal for light-directing nanostructures, *Journal of Materials Chemistry C*, 2018, **6**, 12314-12320.
152. Y.-J. Choi, D. Jung, S.-I. Lim, W.-J. Yoon, D.-Y. Kim and K.-U. Jeong, Diacetylene-Functionalized Dendrons: Self-Assembled and Photopolymerized Three-Dimensional Networks for Advanced Self-Healing and Wringing Soft Materials, *ACS Applied Materials & Interfaces*, 2020, **12**, 33239-33245.
153. S. Shadpour, A. Nemati, N. J. Boyd, L. Li, M. E. Prévôt, S. L. Wakerlin, J. P. Vanegas, M. Salamończyk, E. Hegmann and C. Zhu, Heliconical-layered nanocylinders (HLNCs)–hierarchical self-assembly in a unique B4 phase liquid crystal morphology, *Materials Horizons*, 2019, **6**, 959-968.
154. M. Cano, A. Sánchez-Ferrer, J. L. Serrano, N. Gimeno and M. B. Ros, Supramolecular architectures from bent-core dendritic molecules, *Angewandte Chemie*, 2014, **126**, 13667-13671.
155. L. Zhu, X. Li, Q. Zhang, X. Ma, M. Li, H. Zhang, Z. Luo, H. Ågren and Y. Zhao, Unimolecular photoconversion of multicolor luminescence on hierarchical self-assemblies, *Journal of the American Chemical Society*, 2013, **135**, 5175-5182.
156. J. W. Chung, S.-J. Yoon, B.-K. An and S. Y. Park, High-contrast on/off fluorescence switching via reversible E–Z isomerization of diphenylstilbene containing the α-cyanostilbenic moiety, *The Journal of Physical Chemistry C*, 2013, **117**, 11285-11291.
157. T. Christoff-Tempesta, E. Deiss-Yehiely, P. C. Dromel, L. D. Uliassi, C. A. C. Chazot, A. J. Hart, M. Spector, P. T. Hammond and J. H. Ortony, Antifouling surface coatings from self-assembled zwitterionic aramid amphiphile nanoribbons *Advanced Materials Interfaces*, 2022.
158. K. Page, M. Wilson and I. P. Parkin, Antimicrobial surfaces and their potential in reducing the role of the inanimate environment in the incidence of hospital-acquired infections, *Journal of Materials Chemistry*, 2009, **19**, 3819-3831.
159. D. Talon, The role of the hospital environment in the epidemiology of multi-resistant bacteria, *Journal of Hospital Infection*, 1999, **43**, 13-17.
160. V. B. Damodaran and N. S. Murthy, Bio-inspired strategies for designing antifouling biomaterials, *Biomaterials Research*, 2016, **20**, 18.
161. H. Zhang and M. Chiao, Anti-fouling coatings of poly (dimethylsiloxane) devices for biological and biomedical applications, *Journal of Medical and Biological Engineering*, 2015, **35**, 143-155.
162. G. D. Bixler and B. Bhushan, Biofouling: lessons from nature, *Philosophical Transactions of the Royal Society A: Mathematical, Physical and Engineering Sciences*, 2012, **370**, 2381-2417.
163. Z. K. Zander and M. L. Becker, Antimicrobial and Antifouling Strategies for Polymeric Medical Devices, *ACS Macro Letters*, 2018, **7**, 16-25.
164. D. Lindsay and A. von Holy, Bacterial biofilms within the clinical setting: what healthcare professionals should know, *Journal of Hospital Infection*, 2006, **64**, 313-325.

165. H. Wake, H. Takahashi, T. Takimoto, H. Takayanagi, K. Ozawa, H. Kadoi, M. Okochi and T. Matsunaga, Development of an electrochemical antifouling system for seawater cooling pipelines of power plants using titanium, *Biotechnology and Bioengineering*, 2006, **95**, 468-473.
166. A. Want, M. C. Bell, R. E. Harris, M. Q. Hull, C. R. Long and J. S. Porter, Sea-trial verification of a novel system for monitoring biofouling and testing anti-fouling coatings in highly energetic environments targeted by the marine renewable energy industry, *Biofouling*, 2021, **37**, 433-451.
167. I. Banerjee, R. C. Pangule and R. S. Kane, Antifouling Coatings: Recent Developments in the Design of Surfaces That Prevent Fouling by Proteins, Bacteria, and Marine Organisms, *Advanced Materials*, 2011, **23**, 690-718.
168. C. M. Magin, S. P. Cooper and A. B. Brennan, Non-toxic antifouling strategies, *Materials Today*, 2010, **13**, 36-44.
169. S. Wieck, O. Olsson and K. Kümmerer, Possible underestimations of risks for the environment due to unregulated emissions of biocides from households to wastewater, *Environment International*, 2016, **94**, 695-705.
170. J. A. Callow and M. E. Callow, Trends in the development of environmentally friendly fouling-resistant marine coatings, *Nature Communications*, 2011, **2**, 244.
171. S. B. Levy and B. Marshall, Antibacterial resistance worldwide: causes, challenges and responses, *Nature Medicine*, 2004, **10**, S122-S129.
172. U.S. Centers for Disease Control and Prevention, U.S. Department of Health and Human Services, Current HAI Progress Report: 2019 National and State Healthcare-Associated Infections Progress Report, 2019.
173. R. M. Klevens, J. R. Edwards, C. L. Richards Jr, T. C. Horan, R. P. Gaynes, D. A. Pollock and D. M. Cardo, Estimating health care-associated infections and deaths in US hospitals, 2002, *Public Health Reports*, 2007, **122**, 160-166.
174. M. P. Monopoli, C. Åberg, A. Salvati and K. A. Dawson, Biomolecular coronas provide the biological identity of nanosized materials, *Nature Nanotechnology*, 2012, **7**, 779-786.
175. I. Lynch and K. A. Dawson, Protein-nanoparticle interactions, *Nano Today*, 2008, **3**, 40-47.
176. S. Chen, L. Li, C. Zhao and J. Zheng, Surface hydration: Principles and applications toward low-fouling/nonfouling biomaterials, *Polymer*, 2010, **51**, 5283-5293.
177. J.-m. Zheng, W.-C. Chin, E. Khijniak, E. Khijniak and G. H. Pollack, Surfaces and interfacial water: Evidence that hydrophilic surfaces have long-range impact, *Advances in Colloid and Interface Science*, 2006, **127**, 19-27.
178. P. J. Molino, D. Yang, M. Penna, K. Miyazawa, B. R. Knowles, S. MacLaughlin, T. Fukuma, I. Yarovsky and M. J. Higgins, Hydration Layer Structure of Biofouling-Resistant Nanoparticles, *ACS Nano*, 2018, **12**, 11610-11624.
179. J. L. Dalsin and P. B. Messersmith, Bioinspired antifouling polymers, *Materials Today*, 2005, **8**, 38-46.

180. N. A. Alcantar, E. S. Aydil and J. N. Israelachvili, Polyethylene glycol–coated biocompatible surfaces, *Journal of Biomedical Materials Research*, 2000, **51**, 343-351.
181. Y. Arima, M. Toda and H. Iwata, Complement activation on surfaces modified with ethylene glycol units, *Biomaterials*, 2008, **29**, 551-560.
182. R. Webster, E. Didier, P. Harris, N. Siegel, J. Stadler, L. Tilbury and D. Smith, PEGylated Proteins: Evaluation of Their Safety in the Absence of Definitive Metabolism Studies, *Drug Metabolism and Disposition*, 2007, **35**, 9-16.
183. P. Zhang, F. Sun, S. Liu and S. Jiang, Anti-PEG antibodies in the clinic: Current issues and beyond PEGylation, *Journal of Controlled Release*, 2016, **244**, 184-193.
184. R. P. Garay, R. El-Gewely, J. K. Armstrong, G. Garratty and P. Richette, Antibodies against polyethylene glycol in healthy subjects and in patients treated with PEG-conjugated agents, *Expert Opinion on Drug Delivery*, 2012, **9**, 1319-1323.
185. Y. Liu, D. Zhang, B. Ren, X. Gong, L. Xu, Z.-Q. Feng, Y. Chang, Y. He and J. Zheng, Molecular simulations and understanding of antifouling zwitterionic polymer brushes, *Journal of Materials Chemistry B*, 2020, **8**, 3814-3828.
186. S. Jiang and Z. Cao, Ultralow-Fouling, Functionalizable, and Hydrolyzable Zwitterionic Materials and Their Derivatives for Biological Applications, *Advanced Materials*, 2010, **22**, 920-932.
187. S. Chen, J. Zheng, L. Li and S. Jiang, Strong Resistance of Phosphorylcholine Self-Assembled Monolayers to Protein Adsorption: Insights into Nonfouling Properties of Zwitterionic Materials, *Journal of the American Chemical Society*, 2005, **127**, 14473-14478.
188. J. Baggerman, M. M. J. Smulders and H. Zuilhof, Romantic Surfaces: A Systematic Overview of Stable, Biospecific, and Antifouling Zwitterionic Surfaces, *Langmuir*, 2019, **35**, 1072-1084.
189. A. M. Alswieleh, N. Cheng, I. Canton, B. Ustbas, X. Xue, V. Ladmiral, S. Xia, R. E. Ducker, O. El Zubir and M. L. Cartron, Zwitterionic Poly (amino acid methacrylate) Brushes, *Journal of the American Chemical Society*, 2014, **136**, 9404-9413.
190. B. Li, P. Jain, J. Ma, J. K. Smith, Z. Yuan, H.-C. Hung, Y. He, X. Lin, K. Wu, J. Pfaendtner and S. Jiang, Trimethylamine-*N*-oxide-derived zwitterionic polymers: a new class of ultralow fouling bioinspired materials, *Science Advances*, 2019, **5**, eaaw9562.
191. A. R. Statz, R. J. Meagher, A. E. Barron and P. B. Messersmith, New Peptidomimetic Polymers for Antifouling Surfaces, *Journal of the American Chemical Society*, 2005, **127**, 7972-7973.
192. S. Zhang, Fabrication of novel biomaterials through molecular self-assembly, *Nature Biotechnology*, 2003, **21**, 1171-1178.
193. S. I. Stupp, Self-Assembly and Biomaterials, *Nano Letters*, 2010, **10**, 4783-4786.
194. H. Cui, M. J. Webber and S. I. Stupp, Self-assembly of peptide amphiphiles: From molecules to nanostructures to biomaterials, *Peptide Science*, 2010, **94**, 1-18.

195. Y. Cho, T. Christoff-Tempesta, D.-Y. Kim, G. Lamour and J. H. Ortony, Domain-selective thermal decomposition within supramolecular nanoribbons, *Nature Communications*, 2021, **12**, 1-7.
196. J. Drelich and E. Chibowski, Superhydrophilic and superwetting surfaces: definition and mechanisms of control, *Langmuir*, 2010, **26**, 18621-18623.
197. B. B. Haab, B. H. Geierstanger, G. Michailidis, F. Vitzthum, S. Forrester, R. Okon, P. Saviranta, A. Brinker, M. Sorette, L. Perlee, S. Suresh, G. Drwal, J. N. Adkins and G. S. Omenn, Immunoassay and antibody microarray analysis of the HUPO Plasma Proteome Project reference specimens: Systematic variation between sample types and calibration of mass spectrometry data, *Proteomics*, 2005, **5**, 3278-3291.
198. R. T. Ellison, 3rd and T. J. Giehl, Killing of gram-negative bacteria by lactoferrin and lysozyme, *The Journal of Clinical Investigation*, 1991, **88**, 1080-1091.
199. M. Leeman, J. Choi, S. Hansson, M. U. Storm and L. Nilsson, Proteins and antibodies in serum, plasma, and whole blood-size characterization using asymmetrical flow field-flow fractionation (AF4), *Analytical and Bioanalytical Chemistry*, 2018, **410**, 4867-4873.
200. H.-C. Flemming, J. Wingender, U. Szewzyk, P. Steinberg, S. A. Rice and S. Kjelleberg, Biofilms: an emergent form of bacterial life, *Nature Reviews Microbiology*, 2016, **14**, 563-575.
201. H.-C. Flemming and J. Wingender, The biofilm matrix, *Nature Reviews Microbiology*, 2010, **8**, 623-633.
202. L. Hall-Stoodley, J. W. Costerton and P. Stoodley, Bacterial biofilms: from the Natural environment to infectious diseases, *Nature Reviews Microbiology*, 2004, **2**, 95-108.
203. Centers for Disease Control and Prevention, U.S. Department of Health and Human Services, Antibiotic Resistance Threats in the United States, 2019.
204. D. Nathwani, G. Raman, K. Sulham, M. Gavaghan and V. Menon, Clinical and economic consequences of hospital-acquired resistant and multidrug-resistant Pseudomonas aeruginosa infections: a systematic review and meta-analysis, *Antimicrobial Resistance and Infection Control*, 2014, **3**, 32-32.
205. M. L. Manning, J. Pfeiffer and E. L. Larson, Combating antibiotic resistance: The role of nursing in antibiotic stewardship, *American Journal of Infection Control*, 2016, **44**, 1454-1457.
206. A. Heydorn, A. T. Nielsen, M. Hentzer, C. Sternberg, M. Givskov, B. K. Ersbøll and S. Molin, Quantification of biofilm structures by the novel computer program comstat, *Microbiology*, 2000, **146**, 2395-2407.
207. M. Vorregaard, in *Informatics and Mathematical Modelling*, Technical University of Denmark: Kongens Lyngby, Denmark, 2008.
208. A. Jana and K. Pahan, Fibrillar amyloid-β-activated human astroglia kill primary human neurons via neutral sphingomyelinase: implications for Alzheimer's disease, *Journal of Neuroscience*, 2010, **30**, 12676-12689.

209. X. Liu, M. Jana, S. Dasgupta, S. Koka, J. He, C. Wood and K. Pahan, Human immunodeficiency virus type 1 (HIV-1) tat induces nitric-oxide synthase in human astroglia, *Journal of Biological Chemistry*, 2002, **277**, 39312-39319.
210. S. Henriksen, G. D. Tylden, A. Dumoulin, B. N. Sharma, H. H. Hirsch and C. H. Rinaldo, The human fetal glial cell line SVG p12 contains infectious BK polyomavirus, *Journal of Virology*, 2014, **88**, 7556-7568.
211. Y. Chen, K. Biddell, A. Sun, P. A. Relue and J. D. Johnson, 1999.
212. T. Christoff-Tempesta and J. H. Ortony, Aramid amphiphile nanoribbons for the remediation of lead from contaminated water, *Environmental Science: Nano*, 2021, **8**, 1536-1542.
213. S. Zhang, Emerging biological materials through molecular self-assembly, *Biotechnology Advances*, 2002, **20**, 321-339.
214. A. Dasgupta and D. Das, Designer peptide amphiphiles: self-assembly to applications, *Langmuir*, 2019, **35**, 10704-10724.
215. M. Rad-Malekshahi, L. Lempsink, M. Amidi, W. E. Hennink and E. Mastrobattista, Biomedical applications of self-assembling peptides, *Bioconjugate Chemistry*, 2016, **27**, 3-18.
216. N. Stephanopoulos, J. H. Ortony and S. I. Stupp, Self-assembly for the synthesis of functional biomaterials, *Acta Materialia*, 2013, **61**, 912-930.
217. A. D. Ozkan, A. B. Tekinay, M. O. Guler and E. D. Tekin, Effects of temperature, pH and counterions on the stability of peptide amphiphile nanofiber structures, *RSC Advances*, 2016, **6**, 104201-104214.
218. J. D. Hartgerink, E. Beniash and S. I. Stupp, Peptide-amphiphile nanofibers: a versatile scaffold for the preparation of self-assembling materials, *Proceedings of the National Academy of Sciences*, 2002, **99**, 5133-5138.
219. L. C. Palmer and S. I. Stupp, Molecular self-assembly into one-dimensional nanostructures, *Accounts of Chemical Research*, 2008, **41**, 1674-1684.
220. M. J. Brown and S. Margolis, Lead in drinking water and human blood lead levels in the United States, *Centers for Disease Control and Prevention: Morbidity and Mortality Weekly Report*, 2012, **61**, 1-10.
221. M. Hauptman, R. Bruccoleri and A. D. Woolf, An update on childhood lead poisoning, *Clinical Pediatric Emergency Medicine*, 2017, **18**, 181-192.
222. P. Levallois, P. Barn, M. Valcke, D. Gauvin and T. Kosatsky, Public health consequences of lead in drinking water, *Current Environmental Health Reports*, 2018, **5**, 255-262.
223. E. Obeng-Gyasi, Sources of lead exposure in various countries, *Reviews on Environmental Health*, 2019, **34**, 25-34.
224. T. Dignam, R. B. Kaufmann, L. LeStourgeon and M. J. Brown, Control of lead sources in the United States, 1970-2017: public health progress and current challenges to eliminating lead exposure, *Journal of Public Health Management and Practice*, 2019, **25**, S13.
225. F. Fernandez-Luqueno, F. López-Valdez, P. Gamero-Melo, S. Luna-Suárez, E. N. Aguilera-González, A. I. Martínez, M. García-Guillermo, G. Hernández-Martínez, R. Herrera-Mendoza and M. A. Álvarez-Garza, Heavy metal pollution in drinking

water-a global risk for human health: A review, *African Journal of Environmental Science and Technology*, 2013, **7**, 567-584.
226. J. E. Johnston and A. Hricko, Industrial lead poisoning in Los Angeles: anatomy of a public health failure, *Environmental Justice*, 2017, **10**, 162-167.
227. R. J. Sampson and A. S. Winter, The racial ecology of lead poisoning: Toxic inequality in Chicago neighborhoods, 1995-2013, *Du Bois Review: Social Science Research on Race*, 2016, **13**, 261-283.
228. B. Mondal, D. Bairagi, N. Nandi, B. Hansda, K. S. Das, C. J. C. Edwards-Gayle, V. Castelletto, I. W. Hamley and A. Banerjee, Peptide-Based Gel in Environmental Remediation: Removal of Toxic Organic Dyes and Hazardous Pb^{2+} and Cd^{2+} Ions from Wastewater and Oil Spill Recovery, *Langmuir*, 2020, **36**, 12942-12953.
229. P. J. Knerr, M. C. Branco, R. Nagarkar, D. J. Pochan and J. P. Schneider, Heavy metal ion hydrogelation of a self-assembling peptideviacysteinyl chelation, *Journal of Materials Chemistry*, 2012, **22**, 1352-1357.
230. J. W. Nugent, H.-S. Lee, J. H. Reibenspies and R. D. Hancock, Spectroscopic, structural, and thermodynamic aspects of the stereochemically active lone pair on lead (II): Structure of the lead (II) dota complex, *Polyhedron*, 2015, **91**, 120-127.
231. V. L. Silva, R. Carvalho, M. P. Freitas, C. F. Tormena and W. C. Melo, Spectrometric and theoretical investigation of the structures of Cu and Pb/DTPA complexes, *Structural Chemistry*, 2007, **18**, 605-609.
232. A. Pasha, G. Tircsó, E. T. Benyó, E. Brücher and A. D. Sherry, Synthesis and characterization of DOTA-(amide) 4 derivatives: equilibrium and kinetic behavior of their lanthanide (III) complexes, *European Journal of Inorganic Chemistry*, 2007, **2007**, 4340.
233. E. N. Ushakov, S. P. Gromov, O. A. Fedorova, Y. V. Pershina, M. V. Alfimov, F. Barigelletti, L. Flamigni and V. Balzani, Sandwich-type complexes of alkaline-earth metal cations with a bisstyryl dye containing two crown ether units, *The Journal of Physical Chemistry A*, 1999, **103**, 11188-11193.
234. E. Deiss-Yehiely, J. H. Ortony, B. Qiao, S. I. Stupp and M. Olvera de la Cruz, Ion condensation onto self-assembled nanofibers, *Journal of Polymer Science Part B: Polymer Physics*, 2017, **55**, 901-906.
235. M. R. Schock, I. Wagner and R. Oliphant, The corrosion and solubility of lead in drinking water, *Internal Corrosion of Water Distribution Systems*, 1996, **4**, 131-230.
236. G. Anderegg, F. Arnaud-Neu, R. Delgado, J. Felcman and K. Popov, Critical evaluation of stability constants of metal complexes of complexones for biomedical and environmental applications (IUPAC Technical Report), *Pure and Applied Chemistry*, 2005, **77**, 1445-1495.
237. M. A. P. Cechinel and A. A. U. de Souza, Study of lead (II) adsorption onto activated carbon originating from cow bone, *Journal of Cleaner Production*, 2014, **65**, 342-349.
238. H.-T. Fan, J.-B. Wu, X.-L. Fan, D.-S. Zhang, Z.-J. Su, F. Yan and T. Sun, Removal of cadmium (II) and lead (II) from aqueous solution using sulfur-functionalized silica prepared by hydrothermal-assisted grafting method, *Chemical Engineering Journal*, 2012, **198**, 355-363.

239. Y.-H. Li, S. Wang, J. Wei, X. Zhang, C. Xu, Z. Luan, D. Wu and B. Wei, Lead adsorption on carbon nanotubes, *Chemical Physics Letters*, 2002, **357**, 263-266.
240. L. Mouni, D. Merabet, A. Bouzaza and L. Belkhiri, Adsorption of Pb (II) from aqueous solutions using activated carbon developed from Apricot stone, *Desalination*, 2011, **276**, 148-153.
241. M. Kragović, A. Daković, M. Marković, J. Krstić, G. D. Gatta and N. Rotiroti, Characterization of lead sorption by the natural and Fe (III)-modified zeolite, *Applied Surface Science*, 2013, **283**, 764-774.
242. W. Chen, Z. Lu, B. Xiao, P. Gu, W. Yao, J. Xing, A. M. Asiri, K. A. Alamry, X. Wang and S. Wang, Enhanced removal of lead ions from aqueous solution by iron oxide nanomaterials with cobalt and nickel doping, *Journal of Cleaner Production*, 2019, **211**, 1250-1258.
243. C. Forrey, J. F. Douglas and M. K. Gilson, The fundamental role of flexibility on the strength of molecular binding, *Soft Matter*, 2012, **8**, 6385-6392.
244. A. Stank, D. B. Kokh, J. C. Fuller and R. C. Wade, Protein binding pocket dynamics, *Accounts of Chemical Research*, 2016, **49**, 809-815.
245. P. J. Steinbach, A. Ansari, J. Berendzen, D. Braunstein, K. Chu, B. R. Cowen, D. Ehrenstein, H. Frauenfelder and J. B. Johnson, Ligand binding to heme proteins: connection between dynamics and function, *Biochemistry*, 1991, **30**, 3988-4001.
246. M. C. Thielges, J. r. Zimmermann, W. Yu, M. Oda and F. E. Romesberg, Exploring the energy landscape of antibody–antigen complexes: protein dynamics, flexibility, and molecular recognition, *Biochemistry*, 2008, **47**, 7237-7247.
247. P. Csermely, R. Palotai and R. Nussinov, Induced fit, conformational selection and independent dynamic segments: an extended view of binding events, *Nature Precedings*, 2010, 1-1.
248. J. Janin and M. J. Sternberg, Protein flexibility, not disorder, is intrinsic to molecular recognition, *F1000 Biology Reports*, 2013, **5**.
249. J. H. Ortony, D. S. Hwang, J. M. Franck, J. H. Waite and S. Han, Asymmetric collapse in biomimetic complex coacervates revealed by local polymer and water dynamics, *Biomacromolecules*, 2013, **14**, 1395-1402.
250. M.-P. Gaigeot, M. Sprik and M. Sulpizi, Oxide/water interfaces: how the surface chemistry modifies interfacial water properties, *Journal of Physics: Condensed Matter*, 2012, **24**, 124106.
251. P. K. Verma, R. Saha, R. K. Mitra and S. K. Pal, Slow water dynamics at the surface of macromolecular assemblies of different morphologies, *Soft Matter*, 2010, **6**, 5971-5979.
252. B. Bagchi, Water dynamics in the hydration layer around proteins and micelles, *Chemical Reviews*, 2005, **105**, 3197-3219.
253. Y. Levy and J. N. Onuchic, Water mediation in protein folding and molecular recognition, *Annual Review of Biophysics and Biomolecular Structure*, 2006, **35**, 389-415.
254. M. Maurer and C. Oostenbrink, Water in protein hydration and ligand recognition, *Journal of Molecular Recognition*, 2019, **32**, e2810.

255. J. Boekhoven and S. I. Stupp, Supramolecular materials for regenerative medicine, *Advanced Materials*, 2014, **26**, 1642-1659.
256. C. M. Drain, I. Goldberg, I. Sylvain and A. Falber, in *Functional Molecular Nanostructures*, Springer, 2005, pp. 55-88.
257. K. Bhattacharyya, Solvation dynamics and proton transfer in supramolecular assemblies, *Accounts of Chemical Research*, 2003, **36**, 95-101.
258. D. Bochicchio, M. Salvalaglio and G. M. Pavan, Into the dynamics of a supramolecular polymer at submolecular resolution, *Nature Communications*, 2017, **8**, 147.
259. J. Zheng, L. Li, S. Chen and S. Jiang, Molecular simulation study of water interactions with oligo (ethylene glycol)-terminated alkanethiol self-assembled monolayers, *Langmuir*, 2004, **20**, 8931-8938.
260. O. Borodin, D. Bedrov and G. D. Smith, Concentration dependence of water dynamics in poly (ethylene oxide)/water solutions from molecular dynamics simulations, *The Journal of Physical Chemistry B*, 2002, **106**, 5194-5199.
261. P. Mittelbach, Zur rontgenkleinwinkelstreuung verdunnter kolloider systeme, *Acta Physica Austriaca*, 1961, **14**, 185-211.
262. W. L. Hubbell, D. S. Cafiso and C. Altenbach, Identifying conformational changes with site-directed spin labeling, *Nature Structural Biology*, 2000, **7**, 735-739.
263. B. Liang, J. H. Bushweller and L. K. Tamm, Site-directed parallel spin-labeling and paramagnetic relaxation enhancement in structure determination of membrane proteins by solution NMR spectroscopy, *Journal of the American Chemical Society*, 2006, **128**, 4389-4397.
264. K. R. Daley and K. J. Kubarych, An “iceberg” coating preserves bulk hydration dynamics in aqueous PEG solutions, *The Journal of Physical Chemistry B*, 2017, **121**, 10574-10582.
265. M. F. Cabral, J. Costa, R. Delgado, J. F. Da Silva and M. F. Vilhena, Protonation and metal complexation studies on some oxa-diaza macrocyclic ligands, *Polyhedron*, 1990, **9**, 2847-2857.
266. U. S. Mint, Coin Specifications, accessed March 2022.
267. W. R. Lindemann, T. Christoff-Tempesta and J. H. Ortony, A global minimization toolkit for batch-fitting and χ2 cluster analysis of CW-EPR spectra, *Biophysical Journal*, 2020, **119**, 1937-1945.
268. M. A. Henderson, The interaction of water with solid surfaces: fundamental aspects revisited, *Surface Science Reports*, 2002, **46**, 1-308.
269. K. Murzyn, W. Zhao, M. Karttunen, M. Kurdziel and T. Róg, Dynamics of water at membrane surfaces: Effect of headgroup structure, *Biointerphases*, 2006, **1**, 98-105.
270. F. Pizzitutti, M. Marchi, F. Sterpone and P. J. Rossky, How protein surfaces induce anomalous dynamics of hydration water, *The Journal of Physical Chemistry B*, 2007, **111**, 7584-7590.
271. J. M. Franck and S. Han, Overhauser dynamic nuclear polarization for the study of hydration dynamics, explained, *Methods in Enzymology*, 2019, **615**, 131-175.

272. W. Wriggers, S. Chakravarty and P. A. Jennings, Control of protein functional dynamics by peptide linkers, *Peptide Science: Original Research on Biomolecules*, 2005, **80**, 736-746.
273. G. Natta, Nobel lectures in chemistry, 1963-1970, *Elsevier, Amsterdam*, 1972, **27**, 3.
274. R. Geyer, J. R. Jambeck and K. L. Law, Production, use, and fate of all plastics ever made, *Science Advances*, 2017, **3**, e1700782.
275. M. Hong and E. Y.-X. Chen, Future directions for sustainable polymers, *Trends in Chemistry*, 2019, **1**, 148-151.
276. X. B. Lu, Y. Liu and H. Zhou, Learning nature: recyclable monomers and polymers, *Chemistry–A European Journal*, 2018, **24**, 11255-11266.
277. F. P. La Mantia, Polymer mechanical recycling: Downcycling or upcycling?, *Progress in Rubber Plastics and Recycling Technology*, 2004, **20**, 11-24.
278. B. P. Rosen, Biochemistry of arsenic detoxification, *FEBS Letters*, 2002, **529**, 86-92.
279. S. V. Flanagan, R. B. Johnston and Y. Zheng, Arsenic in tube well water in Bangladesh: health and economic impacts and implications for arsenic mitigation, *Bulletin of the World Health Organization*, 2012, **90**, 839-846.
280. Y. Bhattacharjee, A sluggish response to humanity's biggest mass poisoning. *Science*, 2007.
281. M. J. Kosnett, The role of chelation in the treatment of arsenic and mercury poisoning, *Journal of Medical Toxicology*, 2013, **9**, 347-354.
282. *Guinea Worm Eradication Program*, The Carter Center, 2018.
283. C. Nieto-Delgado, D. Partida-Gutierrez and J. R. Rangel-Mendez, Preparation of activated carbon cloths from renewable natural fabrics and their performance during the adsorption of model organic and inorganic pollutants in water, *Journal of Cleaner Production*, 2019, **213**, 650-658.
284. L. Song, T. Zhao, D. Yang, X. Wang, X. Hao, Y. Liu, S. Zhang and Z.-Z. Yu, Photothermal graphene/UiO-66-NH_2 fabrics for ultrafast catalytic degradation of chemical warfare agent simulants, *Journal of Hazardous Materials*, 2020, **393**, 122332.